UNIVERSITY OF CALIFORNIA, SAN DIEGO

A New Method for Air-Blast–Structure Interaction Based on an Immersed Approach

A dissertation submitted in partial satisfaction of the
requirements for the degree
Doctor of Philosophy

in

Structural Engineering with a Specialization in Computational Science

by

Georgios Moutsanidis

Committee in charge:

Professor Yuri Bazilevs, Chair
Professor Jiun-Shyan Chen
Professor Veronica Eliasson
Professor Gilbert Hegemier
Professor Michael Holst

2018

The dissertation of Georgios Moutsanidis is approved, and it is acceptable in quality and form for publication on microfilm and electronically:

_____

_____

_____

_____

_____

Chair

University of California, San Diego

2018

DEDICATION

To my parents.

EPIGRAPH

I tried so hard and got so far but in the end...

it doesn't even matter.

—Linkin Park

TABLE OF CONTENTS

LIST OF FIGURES

LIST OF TABLES

ACKNOWLEDGEMENTS

First and foremost, I would like to thank my parents for all their help and guidance throughout my studies and my life in general. If it hadn't been for their support, understanding, and encouragement, I wouldn't have been able to fulfill my graduate studies.

I would also like to thank all my friends in Greece, US, northern Europe, and all over the world, for all their support, encouragement and for spending unforgettable moments with me.

I would like to thank my committee members, Prof. Jiun-Shyan Chen, Prof. Veronica Eliasson, Prof. Gilbert Hegemier, and Prof. Michael Holst for sharing their experience and knowledge with me throughout my research.

I would also like to thank Dr. Christopher Long and Dr. Duan Zhang from Los Alamos National Laboratory for sharing their expertise with me and giving me the chance to work with them on cutting edge computational mechanics problems.

I am thankful to all my colleagues at UCSD; Dr. Kazem Kamran, Prof. Artem Korobenko, Dr. Marco Pigazzini, and Dr. Jinhui Yan. I want to thank in particular Dr. Jesus Bueno for his valuable help and guidance during my first steps in my PhD studies, and Dr. David Kamensky for his help and guidance throughout my research at UCSD.

Finally, I would like to express my deep appreciation and gratefulness to my advisor, Prof. Yuri Bazilevs, for his invaluable help during my research and for the opportunity he gave me to follow him as a postdoctoral researcher. Without his help and encouragement this work would have not been posible.

Chapter 2, in part, is a reprint of the material as it appears in: "A new formulation for air-blast fluid–structure interaction using an immersed approach. Part I: basic methodology and FEM-based simulations" (with Y. Bazilevs, K. Kamran, D. Benson, and E. Onate), *Computational Mechanics*, 60, 2017. The dissertation author was one of the primary investigators and authors of the paper.

Chapter 3, in part, is a reprint of the material as it appears in: "A new formulation for air-blast fluid–structure interaction using an immersed approach: part II–coupling of IGA and meshfree discretizations" (with Y. Bazilevs, J. Bueno, K. Kamran, D. Kamensky, M. Hilman, H. Gomez, and J.S. Chen), *Computational Mechanics*, 60, 2017. The dissertation author was the primary investigator and author of the paper.

Chapter 5, in part, is a reprint of the material as it appears in: "Hyperbolic phase field modeling of brittle fracture: Part I—Theory and simulations" (with D. Kamensky and Y. Bazilevs), *Journal of the Mechanics and Physics of Solids*, 2018. The dissertation author was one of the primary investigators and authors of the paper.

Chapter 6, in part, is a reprint of the material as it appears in: "Hyperbolic phase field modeling of brittle fracture: Part II—immersed IGA-RKPM coupling for air-blast–structure interaction" (with D. Kamensky, J.S. Chen and Y. Bazilevs), *Journal of the Mechanics and Physics of Solids*, 2018. The dissertation author was the primary investigator and author of the paper.

VITA

2012	M. Eng. in Civil Engineering, Aristotle University, Thessaloniki, Greece
2012-2014	Graduate Research Assistant, The University of Texas at Austin
2014	M. Sc. in Civil Engineering, The University of Texas at Austin
2014-2018	Graduate Research Assistant, University of California, San Diego
2018	Ph. D. in Structural Engineering with a Specialization in Computational Science, University of California, San Diego

PUBLICATIONS

"Modeling strong discontinuities in the Material Point Method using a single velocity field" (with C. Long, D. Kamensky, D. Zhang, and Y. Bazilevs), *Computer Methods in Applied Mechanics and Engineering*, (under review). The dissertation author was the primary investigator and author of the paper.

"Hyperbolic phase field modeling of brittle fracture: Part II—immersed IGA-RKPM coupling for air-blast–structure interaction" (with D. Kamensky, J.S. Chen and Y. Bazilevs), *Journal of the Mechanics and Physics of Solids*, 2018. The dissertation author was the primary investigator and author of the paper.

"Hyperbolic phase field modeling of brittle fracture: Part I—Theory and simulations" (with D. Kamensky and Y. Bazilevs), *Journal of the Mechanics and Physics of Solids*, 2018. The dissertation author was one of the primary investigators and authors of the paper.

"A new formulation for air-blast fluid–structure interaction using an immersed approach: part II–coupling of IGA and meshfree discretizations" (with Y. Bazilevs, J. Bueno, K. Kamran, D. Kamensky, M. Hilman, H. Gomez, and J.S. Chen), *Computational Mechanics*, 60, 2017. The dissertation author was the primary investigator and author of the paper.

"A new formulation for air-blast fluid–structure interaction using an immersed approach. Part I: basic methodology and FEM-based simulations" (with Y. Bazilevs, K. Kamran, D. Benson, and E. Onate), *Computational Mechanics*, 60, 2017. The dissertation author was one of the primary investigators and authors of the paper.

"Compressible flows on moving domains: stabilized methods, weakly enforced essential boundary conditions, sliding interfaces, and application to gas-turbine modeling" (with F. Xu, D. Kamensky, M.C. Hsu, M. Murugan, A. Ghoshal, and Y. Bazilevs), *Computers and Fluids*, 158, 2017. The dissertation author was one of the primary investigators and authors of the paper.

ABSTRACT OF THE DISSERTATION

A New Method for Air-Blast–Structure Interaction Based on an Immersed Approach

by

Georgios Moutsanidis

Doctor of Philosophy in Structural Engineering with a Specialization in Computational Science

University of California, San Diego, 2018

Professor Yuri Bazilevs, Chair

The numerical simulation of air-blast–structure interaction (ABSI) is a highly challenging and complicated problem. It requires an accurate and robust fluid solver for the Navier-Stokes equations of compressible flow, an advanced computational method that can capture possible structural disintegration, large inelastic deformations and multi-body interaction, as well as a sophisticated fluid–structure interaction (FSI) technique that ensures the correct coupling of the two subsystems.

In this work, a new immersed approach for ABSI is presented. The new method leads to an a-priori monolithic FSI formulation with intrinsic contact detection between solid objects, and without formal restrictions on their motions. The proposed formulation is verified against benchmark problems and experimental results, and is applied to the simulation of a concrete wall subjected to blast loading. A new hyperbolic phase field model for brittle fracture, which eliminates the well-known shortcomings of local damage models, is then developed and coupled with the ABSI formulation. Several numerical examples that demonstrate the capabilities of the method are provided.

Chapter 1

Introduction

Blast loading on structures can be a result of accidents or terrorist attacks and it can cause excessive structural disintegration or human losses. From Ronan Point apartment's collapse [1] to the Alfred P. Murrah Federal Building (aka Oklahoma city bombing, Fig. 1.1) [2] it is evident that mitigating the effects of blasts on infrastructures is imperative. Computational simulation of such events is a promising and reliable tool in order to predict the behavior and protect from the hazardous implications. In this work we aim to develop accurate, robust, and practical computational methodology, which is capable of modeling the dynamics of air blast coupled with the structure response, where the latter involves not only large, inelastic deformations, but also disintegration into fragments, which typically occurs during explosions.

Figure 1.1: The Alfred P. Murrah Federal Building after bombing

Air-blast–structure interaction (ABSI) is a very complicated process. The air flow is in the regime of high Reynolds and Mach numbers, requiring the fluid mechanics numerical simulation to be accurate and robust. The solid objects undergo large inelastic deformations, come in and out of contact with one another, and often fragment into smaller pieces, which requires advanced modeling and discretization techniques for the solid itself, as well as the

management of the fluid mechanics domain and mesh. Moreover, at each time instant the solid and fluid need to have kinematics and tractions in equilibrium to ensure correct coupling between the two subsystems, requiring appropriate coupling at the space-discrete level, and an efficient solution strategy for the coupled system. Finally, the coupled system undergoes rapid transients, which need to be accurately and efficiently captured.

To address the above challenges, we propose a novel ABSI formulation based on the immersed methodology. Moving-mesh methods, such as the Arbitrary-Lagrangian Eulerian (ALE) method [3, 4, 5] are not pursued in the present work because of the challenges they face in modeling fragmentation and structural disintegration. In the proposed method, the Navier-Stokes equations of compressible flow are coupled with a large-deformation inelastic solid. Balance equations for both media are written in the weak form on the current configuration, and the compatibility of kinematics and tractions is established at a fully continuous level. Two discretizations, background and foreground, are employed in the discrete formulation. Foreground discretization, which moves with the solid material particles, is employed to track the solid current position, store the history-dependent variables needed in the solid formulation, and carry out numerical quadrature for the solid terms in the coupled FSI formulation. Pressure-primitive variables [6, 7], which are compatible with the solid degrees-of-freedom (DOFs), are employed to discretize the compressible-flow equations. SUPG [8, 9, 10, 11, 12] and residual-based discontinuity capturing [13, 14, 15, 16, 17, 18] are used to stabilize the compressible-flow formulation.

In this setting, since the background mesh does not track the fluid–solid interface, no formal restrictions on the solid motion are imposed in the coupled formulation. In addition, due to the fact that the fluid and solid share the same background-mesh DOFs, the resulting FSI formulation is a-priori monolithic, even in the case of explicit time integration, which is what we do here to efficiently handle the fast dynamics of air-blast FSI. This a-priori monolithic coupling is a major advantage over existing methods using explicit time stepping in combination with the so-called "loosely-coupled" FSI, in which, unlike in the present formulation, there is no guarantee that the fluid and solid tractions are in equilibrium during the time step.

The proposed methodology shares similarities with the existing immersed-type techniques, such as embedded domain [19, 20, 21, 22, 23, 24, 25, 26], immersed boundary [27, 28], immersed finite element [29, 30], material point method [31, 32], finite cell [33], and immersogeometric [34, 35, 36] methods.

The dissertation is outlined as follows. In chapter 2 we state the basic methodology of our new immersed approach for ABSI. Chapter 3 focuses on a particular instantiation of the proposed framework which couples Isogeometric Analysis (IGA) [37, 38] based on Non-Uniform Rational B-Splines (NURBS) [39, 40, 41] as the background discretization, and the Reproducing Kernel Particle Method (RKPM) [42, 43, 44, 45] as the foreground discretization. This combination is particularly attractive for the problem class of interest due to the higher-order accuracy and higher degree of continuity inherent in both techniques, and the relative simplicity of RKPM in handling the solid large-deformation and fragmentation scenarios. Higher-order accuracy and smoothness of the discretizations was

shown to be beneficial for both fluid and solid/structural mechanics applications, both in terms of accuracy [46, 47] and robustness [48] of the resulting discrete solutions. In addition, in the present framework, higher-order smoothness of the background discretization yields a continuous representation of the strain rate, and thus precludes jumps in the stress and other history variables as the Lagrangian particles cross the background-element boundaries. We note that the strain-rate discontinuity across element boundaries is recognized as a shortcoming of FEM-based material-point-type methods [49], which may be naturally overcome using IGA for the background discretization. The presented numerical examples are compared to different computational techniques and experimental results. In chapter 4 we present the basics of a concrete material implementation as well as a technique for high explosive modeling. The material is modeled after LS-DYNA concrete material model 159 [50] which is a three invariant based model, with rate effects and a local damage evolution law. A numerical example is presented and appears to capture all the major qualitative features of concrete behavior well. Chapter 5 focuses on the treatment of the local damage model's drawbacks presented in chapter 4. A new phase field model of dynamic brittle fracture, in which material damage evolves according to a hyperbolic partial differential equation, is presented. This model can be stably discretized using explicit time integration, without imposing crippling time step restrictions with refinement in space. The model is derived from microforce balance by including effects of microscopic inertia. Chapter 6 applies the formulation developed in chapter 5 to the coupled isogeometric–meshfree ABSI formulation presented in chapters 2,3, where RKPM function spaces are used to solve the phase field equation. The presented benchmark examples are verified against published literature, while the ABSI examples seem to capture all the major qualitative features. Chapter 7 summarizes the presented work, emphasizes on the important original contributions, and outlines future research directions and recommendations.

Chapter 2

Immersed Air-Blast–Structure Interaction: basic theory

In this chapter we present the core air-blast–structure interaction methodology.

2.1 Governing equations of fluid and solid mechanics, and their coupling

In this section we present the governing equations of compressible flow and inelastic solid, and their coupling. All the developments in this section take place at the continuum level, and a weak form of the coupled FSI problem is derived that is suitable for discretization using an immersed technique.

2.1.1 Compressible-flow formulation

The air blast phenomena are modeled using the Navier–Stokes equations of compressible flows, which may be expressed as

$$\mathbf{U}_{,t} + \mathbf{F}_{i,i} - \mathbf{S}^f = \mathbf{0}, \tag{2.1}$$

where

$$\mathbf{U} = \begin{pmatrix} \rho^f \\ \rho^f \mathbf{u} \\ \rho^f e_{tot} \end{pmatrix} \tag{2.2}$$

are the so-called conservation variables [6], ρ^f is the fluid density, $\mathbf{u}$ is the material-particle velocity, $e_{tot} = e + \frac{\|\mathbf{u}\|}{2}$ is the total energy density, and e is the internal energy density given by $e = c_v T$, where c_v is specific heat at constant volume

and T is the temperature. In Eq. (2.1), $\mathbf{S}^f$ is the source term and $\mathbf{F}_i$ is the total flux that consists of advective, pressure, and diffusive contributions, namely,

$$\mathbf{F}_i = \mathbf{F}_i^a + \mathbf{F}_i^p - \mathbf{F}_i^d. \tag{2.3}$$

Here,

$$\mathbf{F}_i^a = u_i \mathbf{U}, \tag{2.4}$$

$$\mathbf{F}_i^p = \begin{pmatrix} 0 \\ p\mathbf{1}_i \\ \mathbf{u} \cdot p\mathbf{1}_i \end{pmatrix}, \tag{2.5}$$

and

$$\mathbf{F}_i^d = \begin{pmatrix} 0 \\ \boldsymbol{\tau}_i \\ \mathbf{u} \cdot \boldsymbol{\tau}_i - q_i, \end{pmatrix}, \tag{2.6}$$

where p is the pressure, $\mathbf{1}_i$ is the i^{th} Cartesian basis vector in $\mathbb{R}^d$, d is the space dimension, $\boldsymbol{\tau}_i$ derives from the viscous stresses and is given by

$$\boldsymbol{\tau}_i = 2\mu \nabla^s \mathbf{u}\mathbf{1}_i + \lambda(\nabla \cdot \mathbf{u})\mathbf{1}_i, \tag{2.7}$$

where μ is the fluid viscosity, $\lambda = -2/3\mu$, and ∇^s is the symmetric spatial gradient, and q_i is the heat flux given by

$$q_i = -\kappa T_{,i}, \tag{2.8}$$

where κ is the fluid thermal conductivity. We assume that the fluid is an ideal gas with the equation of state given by

$$p = \rho^f R T, \tag{2.9}$$

where R is the specific gas constant. In the above formulas, i is the space dimension index, $(\cdot)_{,i}$ denotes a partial derivative with respect to spatial coordinates $\mathbf{x}$, and $(\cdot)_{,t}$ denotes a partial time derivative holding the spatial coordinates fixed. Einstein's summation convention is used throughout the manuscript.

2.1.2 Quasi-linear form of the compressible-flow equations

The Navier–Stokes equations of compressible flows may be written in a quasi-linear form using primitive variables based on pressure [6] as follows

$$\mathbf{A}_0^f \mathbf{Y}_{,t} + \mathbf{A}_i^a \mathbf{Y}_{,i} + \mathbf{F}_{i,i}^p - \mathbf{F}_{i,i}^d - \mathbf{S}^f = \mathbf{0}, \tag{2.10}$$

where $\mathbf{Y}$ denotes the set of pressure-primitive variables given by

$$\mathbf{Y} = \begin{pmatrix} p \\ \mathbf{u} \\ T \end{pmatrix}, \tag{2.11}$$

$\mathbf{A}_0^f$ is the Jacobian of the mapping $\mathbf{U}(\mathbf{Y})$ given by

$$\mathbf{A}_0^f = \frac{\partial \mathbf{U}}{\partial \mathbf{Y}}, \tag{2.12}$$

and $\mathbf{A}_i^a$ is the Jacobian of the mapping $\mathbf{F}_i^a(\mathbf{Y})$ given by

$$\mathbf{A}_i^a = \frac{\partial \mathbf{F}_i^a}{\partial \mathbf{Y}}. \tag{2.13}$$

We also define the Jacobian matrix that takes the pressure terms into account, namely,

$$\mathbf{A}_i^f = \mathbf{A}_i^a + \frac{\partial \mathbf{F}_i^p}{\partial \mathbf{Y}}. \tag{2.14}$$

The above Jacobian matrices may be analytically derived (see [6] for details). Here we provide an explicit expression for $\mathbf{A}_0^f$,

$$\mathbf{A}_0^f = \begin{pmatrix} \rho^f \beta_T & \mathbf{0}^T & -\rho^f \alpha_p \\ \rho^f \beta_T \mathbf{u} & \rho^f \mathbf{I} & -\rho^f \alpha_p \mathbf{u} \\ \rho^f \beta_T e_{tot} & \rho^f \mathbf{u}^T & \rho^f (-\alpha_p e_{tot} + c_v) \end{pmatrix}, \tag{2.15}$$

where $\mathbf{I}$ is a $d \times d$ identity matrix, $\beta_T = 1/p$ and $\alpha_p = 1/T$. Explicit expressions for $\mathbf{A}_i^a$'s and $\mathbf{A}_i^f$'s may be found in [6].

Remark The choice of primitive variables based on pressure to discretize the Navier–Stokes equations of compressible flows in this work is based on two factors: a. This variable set, or a subset thereof, is typically employed for the discretization of the equations of solid and structural mechanics, and thus presents a convenient variable choice for the discretization of the coupled FSI problem; b. The Jacobian matrices have a well defined incompressible limit, which presents a pathway to a unified formulation for both compressible and incompressible flows [51].

2.1.3 Updated Lagrangian formulation of an inelastic solid

We consider an inelastic solid, and state the point-wise balance of mass and momentum written in the updated Lagrangian form [52] as

$$\rho_0^s - \rho^s J = 0, \tag{2.16}$$

$$\rho^s \dot{\mathbf{u}} - \nabla \cdot \boldsymbol{\sigma} - \mathbf{s} = \mathbf{0}. \tag{2.17}$$

In Eqs. (2.16)-(2.17), $\mathbf{u}$, as before, is a material particle velocity, ρ^s and ρ_0^s are the solid densities in the current and reference configurations, respectively, $\boldsymbol{\sigma}$ is the Cauchy stress, $\mathbf{s}$ is the source term, $\dot{(\cdot)}$ is used to denote the material time derivative, that is, time derivative holding material coordinates $\mathbf{X}$ fixed, and $J = \det \frac{\partial \mathbf{x}}{\partial \mathbf{X}}$.

Standard J_2 flow theory with isotropic hardening [53, 54], which is suitable for metals, is considered in this work. The solid constitutive equations, written in the rate form at a material point, are summarized in what follows:

- **Additive decomposition of the rate-of-deformation tensor**:

$$\mathbf{D} = \nabla^s \mathbf{u} = \frac{1}{2}(\nabla \mathbf{u} + \nabla \mathbf{u}^T) = \mathbf{D}^e + \mathbf{D}^p, \tag{2.18}$$

  where $\mathbf{D}^e$ and $\mathbf{D}^p$ are its elastic and plastic components, respectively.

- **Stress-rate constitutive relation**:

$$\boldsymbol{\sigma}^{\nabla J} = \mathbb{C} : \mathbf{D}^e = \mathbb{C} : (\mathbf{D} - \mathbf{D}^p), \tag{2.19}$$

  where $\mathbb{C}$ is the constitutive material tensor, and $\boldsymbol{\sigma}^{\nabla J}$ is the objective Jaumann rate of the Cauchy stress [52] given by

$$\boldsymbol{\sigma}^{\nabla J} = \dot{\boldsymbol{\sigma}} - \boldsymbol{\sigma}\boldsymbol{\omega}^T - \boldsymbol{\omega}\boldsymbol{\sigma}, \tag{2.20}$$

  where $\dot{\boldsymbol{\sigma}}$ is the material time derivative of the Cauchy stress, and

$$\boldsymbol{\omega} = \frac{1}{2}(\nabla \mathbf{u} - \nabla \mathbf{u}^T) \tag{2.21}$$

  is the spin tensor.

- **Yield surface**:

$$f(\boldsymbol{\sigma}, \bar{\epsilon}^p) = \bar{\sigma}(\boldsymbol{\sigma}) - \sigma_Y(\bar{\epsilon}_p) = 0, \tag{2.22}$$

where $\bar{\sigma}$ is the equivalent or von Mises stress given by

$$\bar{\sigma}(\boldsymbol{\sigma}) = \sqrt{\frac{3}{2}\boldsymbol{\sigma}' : \boldsymbol{\sigma}'}, \tag{2.23}$$

$$\boldsymbol{\sigma}' = \boldsymbol{\sigma} - \frac{1}{3}(\mathrm{tr}\,\boldsymbol{\sigma})\,\mathbf{I}, \tag{2.24}$$

and σ_Y is the yield stress assumed dependent on the equivalent plastic strain $\bar{\epsilon}_p$.

- **Flow rule**:

$$\mathbf{D}^p = \dot{\bar{\epsilon}}_p \frac{\partial f}{\partial \boldsymbol{\sigma}}, \tag{2.25}$$

which corresponds to associative plasticity [53, 54] and states that the plastic flow occurs in the direction orthogonal to the yield surface. For the von Mises yield criterion the partial derivative in the associative flow rule equation may be computed explicitly and becomes

$$\frac{\partial f}{\partial \boldsymbol{\sigma}} = \sqrt{\frac{3}{2}} \frac{\boldsymbol{\sigma}'}{\|\boldsymbol{\sigma}'\|}. \tag{2.26}$$

- **Consistency condition**:

$$\dot{f} = \frac{\partial f}{\partial \boldsymbol{\sigma}} : \dot{\boldsymbol{\sigma}} - \frac{\partial f}{\partial \bar{\epsilon}_p} \dot{\bar{\epsilon}}_p = 0, \tag{2.27}$$

which, in combination with the associative flow rule, leads to the following expression for the equivalent plastic-strain rate:

$$\dot{\bar{\epsilon}}_p = \frac{\frac{\partial f}{\partial \boldsymbol{\sigma}} : \mathbb{C} : \mathbf{D}}{H + \frac{\partial f}{\partial \boldsymbol{\sigma}} : \mathbb{C} : \frac{\partial f}{\partial \boldsymbol{\sigma}}}. \tag{2.28}$$

Remark Note that the key quantity appearing in the above constitutive model is $\nabla \mathbf{u}$, the spatial velocity gradient. It is the time history of this quantity that "drives" the evolution of the solid Cauchy stress.

Remark In the present work we consider the solid as isothermal. However, introducing thermal coupling by making the Cauchy stress temperature-dependent and adding the energy-balance equation to the system given by Eqs. (2.16)-(2.17)

does not present a conceptual difficulty and will be pursued in the future work.

2.1.4 Quasi-linear form of the inelastic solid equations

Solid linear-momentum balance given by Eq. (2.17) may be written in a quasi-linear form consistent with that of the Navier–Stokes equations of compressible flows as

$$\mathbf{A}_0^s \dot{\mathbf{Y}} - \mathbf{F}_{i,i}^{\sigma} - \mathbf{S}^s = \mathbf{0}, \tag{2.29}$$

where $\mathbf{Y}$ is the set of primitive variables from Eq. (2.11),

$$\mathbf{A}_0^s = \begin{pmatrix} 0 & \mathbf{0}^T & 0 \\ \mathbf{0} & \rho^s \mathbf{I} & \mathbf{0} \\ 0 & \mathbf{0}^T & 0 \end{pmatrix}, \tag{2.30}$$

$$\mathbf{F}_i^{\sigma} = \begin{pmatrix} 0 \\ \boldsymbol{\sigma} \mathbf{1}_i \\ 0 \end{pmatrix}, \tag{2.31}$$

and

$$\mathbf{S}^s = \begin{pmatrix} 0 \\ \mathbf{s} \\ 0 \end{pmatrix}. \tag{2.32}$$

It is convenient to express the material time derivative in Eq. (2.29) using its spatial counterpart and a convection term as

$$\dot{\mathbf{Y}} = \mathbf{Y}_{,t} + u_i \mathbf{Y}_{,i}, \tag{2.33}$$

in which case the quasi-linear form of Eq. (2.17) may be written as

$$\mathbf{A}_0^s \mathbf{Y}_{,t} + \mathbf{A}_i^s \mathbf{Y}_{,i} - \mathbf{F}_{i,i}^{\sigma} - \mathbf{S}^s = \mathbf{0}, \tag{2.34}$$

where

$$\mathbf{A}_i^s = \begin{pmatrix} 0 & \mathbf{0}^T & 0 \\ \mathbf{0} & \rho^s u_i \mathbf{I} & \mathbf{0} \\ 0 & \mathbf{0}^T & 0 \end{pmatrix}. \tag{2.35}$$

Note that, in this formulation, because the time derivatives in the fluid and solid mechanics governing equations take on the same meaning, one can naturally define a time integration scheme that consistently accounts for the fluid and solid parts of the the coupled FSI problem.

2.1.5 Weak form of the coupled FSI problem

Let Ω denote the combined fluid and solid domain, and let Ω^f and Ω^s denote the individual, time-dependent fluid and solid subdomains in the spatial configuration, such that $\Omega^f \bigcup \Omega^s = \Omega$ and $\Omega^f \bigcap \Omega^s = \emptyset$. Let Γ^{fs} denote their interface, which also evolves in time. We define the following semilinear forms and linear functionals corresponding to the weak forms of the fluid and solid subproblems:

$$M^f_\omega(\mathbf{W},\mathbf{Y}) = \int_\omega \mathbf{W}\cdot\mathbf{A}^f_0\mathbf{Y}_{,t}\; d\omega, \tag{2.36}$$

$$B^f_\omega(\mathbf{W},\mathbf{Y}) = \int_\omega \mathbf{W}\cdot\mathbf{A}^a_i\mathbf{Y}_{,i}\; d\omega - \int_\omega \mathbf{W}_{,i}\cdot(\mathbf{F}^p_i - \mathbf{F}^d_i)\; d\omega, \tag{2.37}$$

$$F^f_\omega(\mathbf{W}) = \int_\omega \mathbf{W}\cdot\mathbf{S}^f\; d\omega + \int_{\Gamma^f_H} \mathbf{W}\cdot\mathbf{H}^f\; d\Gamma, \tag{2.38}$$

$$M^s_\omega(\mathbf{W},\mathbf{Y}) = \int_\omega \mathbf{W}\cdot\mathbf{A}^s_0\mathbf{Y}_{,t}\; d\omega, \tag{2.39}$$

$$B^s_\omega(\mathbf{W},\mathbf{Y}) = \int_\omega \mathbf{W}\cdot\mathbf{A}^s_i\mathbf{Y}_{,i}\; d\omega + \int_\omega \mathbf{W}_{,i}\cdot\mathbf{F}^\sigma_i\; d\omega, \tag{2.40}$$

$$F^s_\omega(\mathbf{W}) = \int_\omega \mathbf{W}\cdot\mathbf{S}^s\; d\omega + \int_{\Gamma^s_H} \mathbf{W}\cdot\mathbf{H}^s\; d\Gamma, \tag{2.41}$$

where $\mathbf{Y}$ and $\mathbf{W}$, the vector-valued trial and test functions, respectively, are the members of $\mathcal{S}$ and $\mathcal{V}$, the corresponding trial and test function spaces, respectively, *defined on all of* Ω, Γ^f_H and Γ^s_H are the subsets of the fluid- and solid-domain boundaries where natural boundary conditions are imposed, and $\mathbf{H}^f$ and $\mathbf{H}^s$ contain the prescribed values of the natural boundary conditions. Note that in Eqs. (6.2)-(6.7) the subscript ω on the semilinear forms and linear functionals denotes the domain of integration.

With the above definitions, the coupled FSI problem maybe stated as: Find $\mathbf{Y} \in \mathcal{S}$, such that $\forall \mathbf{W} \in \mathcal{V}$,

$$
\begin{aligned}
& M^f_{\Omega^f}(\mathbf{W},\mathbf{Y}) + B^f_{\Omega^f}(\mathbf{W},\mathbf{Y}) - F^f_{\Omega^f}(\mathbf{W}) \\
& + \\
& M^s_{\Omega^s}(\mathbf{W},\mathbf{Y}) + B^s_{\Omega^s}(\mathbf{W},\mathbf{Y}) - F^s_{\Omega^s}(\mathbf{W}) \\
& = \\
& 0,
\end{aligned} \tag{2.42}
$$

where we assume that functions in $\mathcal{S}$ and $\mathcal{V}$ have sufficient regularity for the coupled FSI problem given by Eq. (6.1) to be well-posed, and are continuous across Γ^{fs}.

Examination of the Euler–Lagrange conditions for the above coupled problem reveal that the fluid and solid governing equations hold on the interior of their respective domains, namely,

$$
\mathbf{R}^f(\mathbf{Y}) = \mathbf{A}^f_0 \mathbf{Y}_{,t} + \mathbf{A}^a_i \mathbf{Y}_{,i} + \mathbf{F}^p_{i,i} - \mathbf{F}^d_{i,i} = \mathbf{0} \ \text{ in } \Omega^f, \tag{2.43}
$$

and

$$
\mathbf{R}^s(\mathbf{Y}) = \mathbf{A}^s_0 \mathbf{Y}_{,t} + \mathbf{A}^s_i \mathbf{Y}_{,i} - \mathbf{F}^\sigma_{i,i} - \mathbf{S}^s = \mathbf{0} \ \text{ in } \Omega^s, \tag{2.44}
$$

and the natural boundary conditions hold on their respective boundaries, namely,

$$
-\mathbf{F}^p_i n^f_i + \mathbf{F}^d_i n^f_i - \mathbf{H}^f = \mathbf{0} \ \text{ on } \Gamma^f_H, \tag{2.45}
$$

and

$$
\mathbf{F}^\sigma_i n^s_i - \mathbf{H}^s = \mathbf{0} \ \text{ on } \Gamma^s_H, \tag{2.46}
$$

where n^f_i and n^s_i are the cartesian components of the outward unit normal vector to the fluid and solid domains, respectively, in the current configuration. In addition, at the fluid–solid interface, the following compatibility condition holds,

$$
-\mathbf{F}^p_i n^f_i + \mathbf{F}^d_i n^f_i + \mathbf{F}^\sigma_i n^s_i = \mathbf{0} \ \text{ on } \Gamma^{fs}, \tag{2.47}
$$

which is a consequence of the test-function continuity at the fluid–solid interface. Equation (2.47) implies that the fluid

and solid tractions are in equilibrium at the fluid–solid interface, namely,

$$-pn_i^f + \tau_{ij} n_j^f + \sigma_{ij} n_j^s = 0 \ \text{ on } \Gamma^{fs}. \tag{2.48}$$

In addition, the energy-equation component of Eq. (2.47) yields the following condition at the fluid–solid interface

$$-pu_i n_i^f + u_i \tau_{ij} n_j^f - q_i n_i^f = 0 \ \text{ on } \Gamma^{fs}, \tag{2.49}$$

which is a consequence of not considering thermal coupling in the solid mechanics formulation. In case thermal coupling is added to the solid mechanics formulation, Eq. (2.47) would naturally lead to the equilibrium of heat fluxes at the fluid–solid interface.

Remark Using the additive property of integrals, the coupled FSI formulation given by Eq. (6.1) may be re-written as: Find $\mathbf{Y} \in \mathcal{S}$, such that $\forall \mathbf{W} \in \mathcal{V}$,

$$\begin{gathered}
M_\Omega^f(\mathbf{W},\mathbf{Y}) + B_\Omega^f(\mathbf{W},\mathbf{Y}) - F_\Omega^f(\mathbf{W}) \\
+ \\
M_{\Omega^s}^s(\mathbf{W},\mathbf{Y}) + B_{\Omega^s}^s(\mathbf{W},\mathbf{Y}) - F_{\Omega^s}^s(\mathbf{W}) \\
- \\
M_{\Omega^s}^f(\mathbf{W},\mathbf{Y}) + B_{\Omega^s}^f(\mathbf{W},\mathbf{Y}) - F_{\Omega^s}^f(\mathbf{W}) \\
= \\
0,
\end{gathered} \tag{2.50}$$

where the integration over the fluid mechanics domain is replaced by integration over the combined domain *minus* that over the solid domain. This form of the coupled problem, which at the continuous level is equivalent to the original formulation given by Eq.(6.1), is convenient for the application of an immersed approach to the discretization of the coupled FSI equations (see, e.g., [34]).

2.2 Discrete formulation and algorithmic aspects

Here we present the discretization of the continuous FSI formulation developed in the previous section. We briefly cover a stabilized formulation with discontinuity capturing employed for the compressible-flow equations, state the semi-discrete immersed FSI formulation, and present time discretization of the coupled FSI problem, including the

stress update algorithm.

2.2.1 Stabilization of the compressible-flow equations

To discretize the compressible-flow equations we make use of the SUPG formulation [8, 9, 10, 11, 12] augmented with a discontinuity-capturing operator [13, 14, 15, 16, 17, 18]. The latter is important to ensure stability for high-Mach-number flows, which is the case in the present work. We briefly summarize the SUPG and discontinuity-capturing operators in what follows. The reader is referred to [55] for the details of the compressible-flow formulation employed in the present work.

The SUPG stabilization operator for compressible flows may be expressed by means of the following semilinear form:

$$B^{st}_{\omega}(\mathbf{W},\mathbf{Y}) = \int_{\tilde{\omega}} (\mathbf{A}^f_i)^T \mathbf{W}_{,i} \cdot \boldsymbol{\tau} \mathbf{R}^f(\mathbf{Y})\, d\tilde{\omega}, \tag{2.51}$$

where it is assumed that ω is discretized into elements, $\tilde{\omega}$ is a collection of element interiors, the integral $\int_{\tilde{\omega}}$ is taken element-wise, and $\boldsymbol{\tau}$ is a $(d+2)\times(d+2)$ stabilization matrix. We make use of the following definition of $\boldsymbol{\tau}$,

$$\boldsymbol{\tau} = (\mathbf{A}^f_0)^{-1} \hat{\boldsymbol{\tau}}, \tag{2.52}$$

where $\hat{\boldsymbol{\tau}}$ is a stabilization matrix defined for conservation variables (see, e.g., [6, 7]). Premultiplication of $\hat{\boldsymbol{\tau}}$ by $(\mathbf{A}^f_0)^{-1}$ gives an appropriate transformation of the stabilization matrix between the two variable sets.

The discontinuity-capturing operator is also designed for conservation variables with a transformation to the pressure-primitive variables, leading to the following definition,

$$B^{dc}_{\omega}(\mathbf{W},\mathbf{Y}) = \int_{\tilde{\omega}} \mathbf{W}_{,i} \cdot \hat{\boldsymbol{\nu}}^{dc} \mathbf{A}^f_0 \mathbf{Y}_{,i}\, d\tilde{\omega}, \tag{2.53}$$

where $\hat{\boldsymbol{\nu}}^{dc}$ is a diagonal $(d+2)\times(d+2)$ matrix of shock-capturing parameters defined for conservation variables (see e.g., [15, 16, 17, 18, **?**]) and $\mathbf{A}^f_0$ gives the transformation to the primitive-variable formulation. The design of $\hat{\boldsymbol{\nu}}^{dc}$ makes use of the compressible-flow-equation residuals, which renders the discontinuity-capturing operator consistent.

Remark In compressible-flow computations in the blast regime one often makes use of the classical von Neumann–Richtmyer artificial viscosities (see, e.g., [56, 57].) No such viscosities are employed in the present formulation, and the numerical results presented later in the article indicate that shock-capturing given by Eq. (2.53) is sufficient to stabilize the formulation in the high-Mach-number regime of blast waves.

2.2.2 Coupled FSI formulation at the semi-discrete level

Taking the coupled FSI formulation at the continuous level given by Eq. (2.50) as a starting point, and using the SUPG and discontinuity-capturing operators to stabilize the compressible-flow equations, the semi-discrete immersed FSI formulation may be stated as: Find $\mathbf{Y}^h \in \mathcal{S}^h$, such that $\forall \mathbf{W}^h \in \mathcal{V}^h$,

$$
\begin{aligned}
& M^f_{\Omega}(\mathbf{W}^h, \mathbf{Y}^h) + B^f_{\Omega}(\mathbf{W}^h, \mathbf{Y}^h) - F^f_{\Omega}(\mathbf{W}^h) + B^{st}_{\Omega}(\mathbf{W}^h, \mathbf{Y}^h) + B^{dc}_{\Omega}(\mathbf{W}^h, \mathbf{Y}^h) \\
& \qquad + \\
& M^s_{\Omega^s}(\mathbf{W}^h, \mathbf{Y}^h) + B^s_{\Omega^s}(\mathbf{W}^h, \mathbf{Y}^h) - F^s_{\Omega^s}(\mathbf{W}^h) \\
& \qquad - \\
& M^f_{\Omega^s}(\mathbf{W}^h, \mathbf{Y}^h) + B^f_{\Omega^s}(\mathbf{W}^h, \mathbf{Y}^h) - F^f_{\Omega^s}(\mathbf{W}^h) + B^{st}_{\Omega^s}(\mathbf{W}^h, \mathbf{Y}^h) + B^{dc}_{\Omega^s}(\mathbf{W}^h, \mathbf{Y}^h) \\
& \qquad + \\
& \int_{\tilde{\Gamma}^f} \beta h \, [[\mathbf{w}^h_{,i} n_i]] \cdot [[\mathbf{u}^h_{,j} n_j]] \, d\tilde{\Gamma} \\
& \qquad = \\
& \qquad 0.
\end{aligned}
\tag{2.54}
$$

Here, $\mathbf{Y}^h$ and $\mathbf{W}^h$, the discrete trial and test functions, respectively, and $\mathcal{S}^h$ and $\mathcal{V}^h$, the corresponding discrete function spaces, are defined *on the background domain* Ω. As a result, the unknown degrees of freedom (DOFs) are defined completely on the background mesh. Equal-order discretization is employed for all the unknowns in the variable set $\mathbf{Y}^h$.

In Eq. (6.26) the integrals are computed using numerical quadrature. The terms on the first and fourth lines on the left-hand-side of Eq. (6.26) are computed using quadrature rules defined on the background domain, while the terms on the second and third lines are computed using foreground-domain quadrature rules. To carry out integration on the foreground mesh, the background mesh quantities need to be evaluated at the locations corresponding to the quadrature points of the foreground mesh. These locations are found through a simple inverse mapping.

Remark It is well known that solid near incompressibility may lead to volumetric locking, which is especially pronounced for lower-order elements. To alleviate this phenomenon, we adapt a *B-bar* methodology [58, 59, 60] to the solid mechanics part of the present immersed FSI formulation. In the evaluation of the velocity and test-function gradients, the strain displacement matrix *from the background discretization* is replaced with its *B-bar* counterpart in a standard fashion, wherein the dilatational part of the motion is projected to a lower-order space (see, e.g., [58, 61]). In the present work, the *B-bar* methodology is only employed for C^0-continuous linear FEM background discretizations.

The last term on the left-hand-side of Eq. (6.26) is the so-called "ghost velocity" stabilization developed for immersed FEM in [62]. In this term $\mathbf{w}$ is used to denote the linear-momentum components of the test function $\mathbf{W}$, $[\![\cdot]\!]$ is the "jump" operator, $\tilde{\Gamma}^f$ is the set of all edges in 2D and faces in 3D near the interface, h is the size of the local edge or face, and β is the mesh-independent penalty parameter. Ghost velocity stabilization penalizes the jump in the velocity gradient near the fluid–solid interface and significantly improves the stability of the velocity solution.

Remark The edge or face over which the ghost velocity stabilization is applied is such that both elements sharing that edge or face are either covered by the structure or cut by the interface. This condition excludes edges or faces that are on the exterior of the cut-element set.

Remark For a thermally coupled solid, an analogous stabilization technique may be employed also for the temperature variable.

Remark Note that the ghost velocity stabilization terms are active only in the case when a C^0-continuous background discretization is employed. When smooth splines are used, this term vanishes due to the basis-function derivative continuity across element boundaries. Although stability of spline discretizations may be further improved by penalizing higher-order velocity and temperature derivatives at cut-element edges or faces, this is not done in the present work.

2.2.3 Time discretization

An *explicit* version of the Generalized-α method [63, 64, 65] is employed for the time discretization of Eq. (6.26). In this case the discrete residual $\boldsymbol{\mathcal{R}}$ is thought of as a function of the background nodal or control-point unknown vector $\boldsymbol{\mathcal{Y}}$ and its time derivative $\dot{\boldsymbol{\mathcal{Y}}}$, namely,

$$\boldsymbol{\mathcal{R}}(\dot{\boldsymbol{\mathcal{Y}}},\boldsymbol{\mathcal{Y}}) = \boldsymbol{\mathcal{M}}\dot{\boldsymbol{\mathcal{Y}}} + \boldsymbol{\mathcal{N}}(\boldsymbol{\mathcal{Y}}). \tag{2.55}$$

In Eq. (2.55), to set the stage for an explicit time integration algorithm, the discrete residual is decomposed into the parts containing $\boldsymbol{y}$ and $\dot{\boldsymbol{y}}$. Also in Eq. (2.55),

$$
\begin{aligned}
[\boldsymbol{M}]^{ab}_{AB} = &\int_{\Omega} N_A [\mathbf{A}^f_0]_{ab} N_B \, d\Omega \\
&+ \\
&\int_{\Omega^s} N_A [\mathbf{A}^s_0]_{ab} N_B \, d\Omega \\
&- \\
&\int_{\Omega^s} N_A [\mathbf{A}^f_0]_{ab} N_B \, d\Omega,
\end{aligned}
\tag{2.56}
$$

are the components of the coupled mass matrix, A, B are the nodal or control-point indices, a, b are the local DOF indices, and N's are the basis function coming from the background discretization. The residual vector $\boldsymbol{N}(\boldsymbol{y})$ is comprised of the remaining terms in the coupled FSI formulation given by Eq. (6.26), and its components may be expressed as

$$
\begin{aligned}
[\boldsymbol{N}(\boldsymbol{y})]^a_A = &B^f_{\Omega}(N_A \mathbf{E}_a, \mathbf{Y}^h) - F^f_{\Omega}(N_A \mathbf{E}_a) + B^{st}_{\Omega}(N_A \mathbf{E}_a, \mathbf{Y}^h) + B^{dc}_{\Omega}(N_A \mathbf{E}_a, \mathbf{Y}^h) \\
&+ \\
&B^s_{\Omega^s}(N_A \mathbf{E}_a, \mathbf{Y}^h) - F^s_{\Omega^s}(N_A \mathbf{E}_a) \\
&- \\
&B^f_{\Omega^s}(N_A \mathbf{E}_a, \mathbf{Y}^h) - F^f_{\Omega^s}(N_A \mathbf{E}_a) + B^{st}_{\Omega^s}(N_A \mathbf{E}_a, \mathbf{Y}^h) + B^{dc}_{\Omega^s}(N_A \mathbf{E}_a, \mathbf{Y}^h) \\
&+ \\
&\int_{\tilde{\Gamma}^f} \beta h \, [\![N_{A,i} n_i \mathbf{1}_{b(a)}]\!] \cdot [\![\mathbf{u}^h_{,j} n_j]\!] \, d\tilde{\Gamma},
\end{aligned}
\tag{2.57}
$$

where $\mathbf{E}_a$ is the a^{th} Cartesian basis vector in $\mathbb{R}^{d+2}$, and $\mathbf{1}_b$, as before, is the b^{th} Cartesian basis vector in $\mathbb{R}^d$, with $b(a) = a - 1$ and $\mathbf{1}_0 = \mathbf{1}_{d+1} = \mathbf{0}$.

The Generalized-α technique applied to Eq. (2.55) amounts to collocating the discrete residual at the intermediate locations within a time step as follows: Given $\boldsymbol{y}_n$ and $\dot{\boldsymbol{y}}_n$, find $\boldsymbol{y}_{n+1}$ and $\dot{\boldsymbol{y}}_{n+1}$, such that,

$$
\boldsymbol{\mathcal{R}}(\dot{\boldsymbol{y}}_{n+\alpha_m}, \boldsymbol{y}_{n+\alpha_f}) = \mathbf{0},
\tag{2.58}
$$

where the intermediate solution time levels are defined as

$$
(\cdot)_{n+\alpha} = (\cdot)_n + \alpha((\cdot)_{n+1} - (\cdot)_n),
\tag{2.59}
$$

and the relationship between the solution and its time derivative in the time-discrete setting is given by the Newmark formula

$$\boldsymbol{y}_{n+1} = \boldsymbol{y}_n + \Delta t((1-\gamma)\dot{\boldsymbol{y}}_n + \gamma\dot{\boldsymbol{y}}_{n+1}). \tag{2.60}$$

Here, α_m, α_f, and γ are real-valued parameters chosen based on the second-order accuracy and unconditional stability requirements of the Generalized-α method. See [63, 64, 65] for more details.

Predictor-multicorrector algorithm

To solve the nonlinear system given by Eqs. (2.58)-(2.60) we adopt an *explicit* version of a two-stage predictor-multicorrector algorithm presented in what follows.

Predictor stage. Given the solution at time level t_n, initialize the time-level t_{n+1} solution as

$$\begin{aligned} \dot{\boldsymbol{y}}^0_{n+1} &= \frac{\gamma-1}{\gamma}\dot{\boldsymbol{y}}_n, \\ \boldsymbol{y}^0_{n+1} &= \boldsymbol{y}_n. \end{aligned} \tag{2.61}$$

In addition, the foreground solid domain position at time level t_{n+1} is initialized as follows:

$$\begin{aligned} \mathbf{a}^0_{n+1} &= \frac{\gamma-1}{\gamma}\mathbf{a}_n, \\ \mathbf{u}^0_{n+1} &= \mathbf{u}_n, \\ \mathbf{d}^0_{n+1} &= \mathbf{d}_n + \Delta t\mathbf{u}_n + \frac{\Delta t^2}{2}((1-2\beta)\mathbf{a}_n + 2\beta\mathbf{a}^0_{n+1}), \end{aligned} \tag{2.62}$$

where $\mathbf{a}$, $\mathbf{u}$, and $\mathbf{d}$ denote the solid nodal or control-point values of the acceleration, velocity and displacement, and β is the additional Newmark parameter of the Generalized-α scheme. The displacement variable $\mathbf{d}$ is used to place the foreground solid mesh in the appropriate configuration for the purposes of numerical integration.

Multicorrector stage. Compute the solution at time level t_{n+1} by repeating the following steps:

1. Evaluate the iterates at intermediate time levels on the background mesh,

$$\begin{aligned} \dot{\boldsymbol{y}}^l_{n+\alpha_m} &= \dot{\boldsymbol{y}}_n + \alpha_m(\dot{\boldsymbol{y}}^l_{n+1} - \dot{\boldsymbol{y}}_n), \\ \boldsymbol{y}^l_{n+\alpha_f} &= \boldsymbol{y}_n + \alpha_f(\boldsymbol{y}^l_{n+1} - \boldsymbol{y}_n), \end{aligned} \tag{2.63}$$

and on the foreground mesh,

$$\mathbf{d}^l_{n+\alpha_f} = \mathbf{d}_n + \alpha_f(\mathbf{d}^l_{n+1} - \mathbf{d}_n), \tag{2.64}$$

where l is the multicorrector iteration counter.

2. Use the intermediate solution values to assemble the discrete residual of the coupled FSI problem and solve for the increment of the solution time derivative,

$$\Delta\dot{\boldsymbol{\mathcal{Y}}}^l_{n+1} = -(\alpha_m \boldsymbol{\mathcal{M}})^{-1}\, \boldsymbol{\mathcal{R}}(\dot{\boldsymbol{\mathcal{Y}}}^l_{n+\alpha_m}, \boldsymbol{\mathcal{Y}}^l_{n+\alpha_f}). \tag{2.65}$$

In the above equation, in the interest of efficiency, $\boldsymbol{\mathcal{M}}$ may approximated by its lumped counterpart given by

$$\begin{aligned} \boldsymbol{\mathcal{M}} &\approx \boldsymbol{\mathcal{M}}_L, \\ [\boldsymbol{\mathcal{M}}_L]^{ab}_{AB} &= (\sum_C [\boldsymbol{\mathcal{M}}]^{ab}_{BC})\delta_{AB}, \end{aligned} \tag{2.66}$$

where δ_{AB} is the Kronecker delta.

3. Update the solution on the background mesh,

$$\begin{aligned} \dot{\boldsymbol{\mathcal{Y}}}^{l+1}_{n+1} &= \dot{\boldsymbol{\mathcal{Y}}}^l_{n+1} + \Delta\dot{\boldsymbol{\mathcal{Y}}}^l_{n+1}, \\ \boldsymbol{\mathcal{Y}}^{l+1}_{n+1} &= \boldsymbol{\mathcal{Y}}^l_{n+1} + \gamma\Delta t\Delta\dot{\boldsymbol{\mathcal{Y}}}^l_{n+1}, \end{aligned} \tag{2.67}$$

and on the foreground mesh,

$$\begin{aligned} \mathbf{u}^{l+1}_{n+1} &= \mathcal{I}\boldsymbol{\mathcal{Y}}^{l+1}_{n+1}, \\ \mathbf{a}^{l+1}_{n+1} &= \frac{\mathbf{u}^{l+1}_{n+1} - \mathbf{u}_n}{\gamma\Delta t} - \frac{1-\gamma}{\gamma}\mathbf{a}_n, \\ \mathbf{d}^{l+1}_{n+1} &= \mathbf{d}_n + \Delta t\mathbf{u}_n + \frac{\Delta t^2}{2}((1-2\beta)\mathbf{a}_n + 2\beta\mathbf{a}^{l+1}_{n+1}), \end{aligned} \tag{2.68}$$

and increase the Newton-iteration counter l by one. Note that, just like in the predictor stage, the update of the foreground mesh kinematics entails the velocity projection from the background mesh, denoted by the symbol $\mathcal{I}$ above, followed by the reconstruction of the remaining kinematic quantities via the Newmark formulas.

Remark Computation of the solution-time-derivative increment in Eq. (2.65) using a lumped mass matrix requires computing the inverse of a $(d+2)\times(d+2)$ matrix at each background-mesh node or control point. It is possible to

develop a vector representation of the lumped-mass matrix of the form

$$[\boldsymbol{\mathcal{M}}_L]_A^{ab} = [\overline{\mathbf{A}}_0]^{ab} \int_\Omega N_A \, d\Omega, \tag{2.69}$$

where $\overline{\mathbf{A}}_0$ is the equivalent Jacobian matrix associated with node or control point A. The matrix $\overline{\mathbf{A}}_0$ has an inverse, which may be derived analytically (see [66]) and programmed directly, leading to modest improvements in the computational efficiency of the time-integration algorithm.

Remark In the last step of the multicorrector algorithm, once the solution is obtained on the background mesh, kinematic quantities are transferred to the foreground mesh and the solid is moved to a new position. This procedure is also employed in the particle finite element method (PFEM) [67, 68].

Stress update

Computation of the discrete residual In Eq. (2.65) requires evaluation of the solid Cauchy stress at the quadrature points of the foreground mesh, which act as material points in the current formulation. The Cauchy stress may be advanced within a time step as follows,

$$\boldsymbol{\sigma}_{n+1} = \boldsymbol{\sigma}_n + \Delta t \, \dot{\boldsymbol{\sigma}}_{n+\alpha_f} = \boldsymbol{\sigma}_n + \Delta t \, (\boldsymbol{\sigma}^{\nabla J} + \boldsymbol{\omega}\boldsymbol{\sigma} + \boldsymbol{\sigma}\boldsymbol{\omega}^T)_{n+\alpha_f}, \tag{2.70}$$

where the objective Jaumann stress rate is employed, and, for consistency with the Generalized-α time integration algorithm, the material time derivative of the stress is taken at the time level $t_{n+\alpha_f}$. To carry out the above stress update, at each multicorrector iteration of the Generalized-α algorithm, we repeat following steps:

1. Rotate the Cauchy stress to the time level $t_{n+\alpha_f}$ as

$$\tilde{\boldsymbol{\sigma}}^l_{n+\alpha_f} = \boldsymbol{\sigma}_n + \alpha_f \Delta t \, (\boldsymbol{\omega}^l_{n+\alpha_f}\boldsymbol{\sigma}_n + \boldsymbol{\sigma}_n(\boldsymbol{\omega}^l_{n+\alpha_f})^T), \tag{2.71}$$

   where l is the iteration counter of the multicorrector stage, and the spin tensor at time level $t_{n+\alpha_f}$ is computed from the background discretization as

$$\boldsymbol{\omega}^l_{n+\alpha_f} = \frac{1}{2}(\nabla \mathbf{u}^l_{n+\alpha_f} - (\nabla \mathbf{u}^l_{n+\alpha_f})^T). \tag{2.72}$$

2. Update the Cauchy stress at time level $t_{n+\alpha_f}$ as

$$\boldsymbol{\sigma}^l_{n+\alpha_f} = \tilde{\boldsymbol{\sigma}}^l_{n+\alpha_f} + \Delta\boldsymbol{\sigma}^l_{n+\alpha_f}, \tag{2.73}$$

where $\Delta\boldsymbol{\sigma}_{n+\alpha_f} = \Delta t\, \boldsymbol{\sigma}^{\nabla J}_{n+\alpha_f}$ is the stress increment coming form the radial return mapping scheme [52].

3. Rotate the Cauchy stress to the time level t_{n+1} as

$$\boldsymbol{\sigma}^l_{n+1} = \boldsymbol{\sigma}^l_{n+\alpha_f} + (1-\alpha_f)\Delta t\, (\boldsymbol{\omega}^l_{n+\alpha_f}\boldsymbol{\sigma}^l_{n+\alpha_f} + \boldsymbol{\sigma}^l_{n+\alpha_f}(\boldsymbol{\omega}^l_{n+\alpha_f})^T). \tag{2.74}$$

Remark The above stress update is a modification of the well-known half-step rotation technique [69, 70]. The resulting Cauchy stress in Step 2 is used in the computation of the solid contribution to the discrete residual in Eq. (2.65), while the stress in Step 3 is saved for the purposes of performing the stress update in the next time step.

2.3 Conclusions

A computational framework for air-blast FSI based on an immersed approach is proposed. The framework couples compressible flow in the high-Mach-number regime with inelastic structures. The discrete formulation employs the background and foreground discretization as follows. Background discretization is fixed and provides the discrete trial and test function spaces for the coupled FSI problem. Foreground discretization is moving with the solid material particles and is employed to track its current position, store history-dependent variables, and perform numerical quadrature.

The compressible-flow equations are discretized using pressure-primitive variables for compatibility with the solid DOFs and stabilized using residual-based SUPG and discontinuity-capturing techniques. These appear to be sufficient to produce a robust computational methodology for air blast without resorting to classical shock viscosities, which are not consistent and often tend to produce overly diffusive results.

The proposed immersed approach has the advantage over existing embedded domain methods in that a monolithic FSI formulation is naturally obtained, even if the governing equations are advanced in time using an explicit algorithm. In addition, no restrictions on the solid motion is imposed in the framework, which enables handling of the domain topological changes with relative ease. Although, due to the utilization of an immersed approach, fluid mechanics accuracy near the solid surfaces is not as high as in a moving-mesh technique, preliminary comparisons with an ALE-based approach suggest that in the regime of air blast the overall accuracy of the coupled simulations does not suffer significantly. This is likely due to the fact that because of the fast dynamics of air blast, fluid boundary layers, which require higher mesh resolution near solid walls for good accuracy, do not have a chance to develop fully.

2.4 Acknowledgements

Chapter 2, in part, is a reprint of the material as it appears in: “A new formulation for air-blast fluid–structure interaction using an immersed approach. Part I: basic methodology and FEM-based simulations” (with Y. Bazilevs, K. Kamran, D. Benson, and E. Onate), *Computational Mechanics*, 60, 2017. The dissertation author was one of the primary investigators and authors of the paper.

Chapter 3

Immersed Air-Blast–Structure Interaction: coupling of isogeometric and meshfree discretizations

This chapter focuses on a particular instantiation of the proposed ABSI framework, which couples isogeometric analysis with reproducing-kernel particle method, which is a meshfree technique.

3.1 NURBS-based IGA

In this section we briefly recall the basics of IGA [37, 38] based on NURBS [39, 40, 41]. NURBS are convenient for free-form surface modeling, and can represent exactly all conic sections. In addition, they exhibit excellent mathematical properties, such as derivative-continuity across element boundaries, optimal approximation [71], and the ability to be refined through knot insertion and degree elevation. We note that in the present effort NURBS-based IGA is employed to provide a smooth background-mesh discretization, which has significant benefits compared to C^0-continuous approximations in many applications [38, 47, 72, 71, 73, 74]. In the present work we do not directly take advantage of the geometric flexibility of IGA, although one may envision cases where background discretization conforming to geometrically-complex fluid-mechanics domains may be desirable.

3.1.1 B-splines

NURBS are built from B-splines. A necessary component for the construction of B-splines is the knot vector. A knot vector in 1D is a non-decreasing set of coordinates in the parametric domain written as $\Xi = \{\xi_1, \xi_2, \ldots, \xi_{n+p+1}\}$, where $\xi_i \in \mathbb{R}$ is the i^{th} knot, i is the knot index, $i = 1, 2, \ldots, n+p+1$, p is the polynomial order, and n is the number of B-spline basis functions. Knots divide the parametric domain into elements.

For a given knot vector, the B-spline basis functions are defined recursively starting with piecewise constants ($p = 0$):

$$N_{i,0}(\xi) = \begin{cases} 1 \text{ if } \xi_i \leq \xi < \xi_{i+1}, \\ 0 \text{ otherwise.} \end{cases} \tag{3.1}$$

For $p = 1, 2, 3, \ldots$, they are defined by

$$N_{i,p}(\xi) = \frac{\xi - \xi_i}{\xi_{i+p} - \xi_i} N_{i,p-1}(\xi) + \frac{\xi_{i+p+1} - \xi}{\xi_{i+p+1} - \xi_{i+1}} N_{i+1,p-1}(\xi), \tag{3.2}$$

which is the Cox-de Boor recursion formula [75, 76].

Knot vectors may be open or closed. In an open knot vector the first and last knot values appear $p+1$ times. B-spline basis functions constructed using an open knot vector are interpolatory at the endpoints of the parametric interval, which facilitates imposition of boundary conditions. In general, B-splines are not interpolatory at interior knots. Only open knot vectors are employed in the present work.

Basis functions of order p have $p - m_i$ continuous derivatives at knot ξ_i, where m_i is the multiplicity of the knot ξ_i in the knot vector.

The B-spline basis functions are pointwise non-negative, satisfy the partition of unity, that is,

$$\sum_{i=1}^{n} N_{i,p}(\xi) = 1 \quad \forall \xi \in \Xi, \tag{3.3}$$

and the support of each basis function $N_{i,p}$ is compact and contained in the interval $[\xi_i, \xi_{i+p+1}]$.

3.1.2 NURBS

Geometric entities in $\mathbb{R}^{\mathrm{d}}$ are obtained by a projective transformation of B-spline curves in $\mathbb{R}^{\mathrm{d}+1}$, where d is the space dimension. Conic sections may be exactly constructed by projective transformations of piecewise quadratic curves. This projective transformation gives rise to NURBS basis functions with the following structure:

$$R_i^p(\xi) = \frac{N_{i,p}(\xi) w_i}{W(\xi)}, \tag{3.4}$$

where $W(\xi)$ is the weighting function given by

$$W(\xi) = \sum_{i=1}^{n} N_{i,p}(\xi) w_i, \tag{3.5}$$

where w_i's are positive weights. As is evident from the above expressions, unlike B-spline or standard FEM basis functions that are piecewise polynomials, NURBS are piecewise rational functions.

NURBS curves are constructed using a linear combination of NURBS basis functions as

$$\mathbf{C}(\xi) = \sum_{i=1}^{n} R_i^p(\xi) \mathbf{B}_i, \tag{3.6}$$

where $\mathbf{B}_i \in \mathbb{R}^{\mathrm{d}}$ are the control points. Given additional knot vectors $H = \{\eta_1, \eta_2, \ldots, \eta_{m+q+1}\}$ and $Z = \{\zeta_1, \zeta_2, \ldots, \zeta_{l+r+1}\}$, NURBS basis functions in 2D and 3D may be defined as

$$R_{i,j}^{p,q}(\xi,\eta) = \frac{N_{i,p}(\xi) M_{j,q}(\eta) w_{i,j}}{\sum_{\hat{i}=1}^{n} \sum_{\hat{j}=1}^{m} N_{\hat{i},p}(\xi) M_{\hat{j},q}(\eta) w_{\hat{i},\hat{j}}}, \tag{3.7}$$

and

$$R_{i,j,k}^{p,q,r}(\xi,\eta,\zeta) = \frac{N_{i,p}(\xi) M_{j,q}(\eta) L_{k,r}(\zeta) w_{i,j,k}}{\sum_{\hat{i}=1}^{n} \sum_{\hat{j}=1}^{m} \sum_{k=1}^{l} N_{\hat{i},p}(\xi) M_{\hat{j},q}(\eta) L_{\hat{k},r}(\zeta) w_{\hat{i},\hat{j},\hat{k}}}, \tag{3.8}$$

respectively, where $w_{\hat{i},\hat{j}}$ and $w_{\hat{i},\hat{j},\hat{k}}$ are the corresponding weights.

Following the properties of B-splines, NURBS basis functions in all dimensions are pointwise nonnegative, form a partition of unity, are compactly supported, and reduce to B-splines if all the weights are equal.

Analogously to NURBS curves, NURBS surfaces and volumes are defined as

$$\mathbf{S}(\xi,\eta) = \sum_{i=1}^{n} \sum_{j=1}^{m} R_{i,j}^{p,q}(\xi,\eta) \mathbf{B}_{i,j} \tag{3.9}$$

and

$$\mathbf{V}(\xi,\eta,\zeta) = \sum_{i=1}^{n} \sum_{j=1}^{m} \sum_{k=1}^{l} R_{i,j,k}^{p,q,r}(\xi,\eta,\zeta) \mathbf{B}_{i,j,k}, \tag{3.10}$$

respectively, where $\mathbf{B}_{i,j}$'s and $\mathbf{B}_{i,j,k}$ form a control mesh.

3.1.3 Analysis framework

We write $\hat{N}(\boldsymbol{\xi})$ and $N(\mathbf{x})$ to refer to a generic NURBS basis function defined on the parametric and physical domains, respectively. We also make use of a single-index notation, and let indices $A, B, C, \ldots$ label the NURBS basis

functions. In this setting, the geometry mapping may be expressed as

$$\mathbf{x}(\boldsymbol{\xi}) = \sum_{A=1}^{\mathrm{n_{np}}} \mathbf{x}_A \hat{N}_A(\boldsymbol{\xi}), \tag{3.11}$$

where $\mathrm{n_{np}}$ denotes the number of control points in the mesh with coordinates given by $\mathbf{x}_A$'s. This mapping may be restricted to a NURBS patch or element.

The IGA solution in the parametric domain, taken to be scalar-valued for the purposes of illustration, is assumed to be governed by the same NURBS basis functions, and may be expressed as

$$\hat{u}^h(\boldsymbol{\xi}) = \sum_{A=1}^{\mathrm{n_{np}}} u_A \hat{N}_A(\boldsymbol{\xi}), \tag{3.12}$$

where u_A's are the control variables or degrees of freedom (DOF). The IGA solution in the physical domain is defined as a push-forward of its parametric counterpart given by Eq. (3.12) by the geometrical mapping given by Eq. (3.11), and may be expressed as

$$u^h(\mathbf{x}) = \sum_{A=1}^{\mathrm{n_{np}}} u_A N_A(\mathbf{x}), \tag{3.13}$$

where

$$N_A(\mathbf{x}) = \hat{N}_A(\boldsymbol{\xi}^{-1}(\mathbf{x})). \tag{3.14}$$

Equations (3.11)-(3.14) constitute the well-known isoparametric construction widely used in FEM and IGA. The above construction guarantees optimal approximation properties of NURBS spaces as shown in [71, 77].

The first and second partial derivatives of the basis functions in Eq. (3.14) with respect to physical coordinates, which are employed in the weak formulation of the FSI problem presented in chapter 2, are computed using the chain rule in a manner similar to FEM. To carry out the background-domain weak-form integrals, standard Gaussian quadrature is employed. It should be noted that more efficient quadrature rules for IGA have been recently proposed (see, e.g., [78, 79]) and may be employed for better efficiency of the computational procedures. Dirichlet boundary conditions in IGA may be imposed strongly by selecting appropriate values of control variables belonging to essential boundaries, or weakly by means of Nitsche-like methods [80]. Because of the variational structure of IGA, Neumann boundary conditions are enforced weakly as in standard FEM.

3.2 RKPM-based Meshfree methods

Like IGA, Meshfree methods is a class of numerical methods that solve partial differential equations. They retain the useful characteristics of the FEM, such as good approximation properties and compact support of shape

functions, but attempt to overcome some of the disadvantages, like mesh entanglement, material distortion, mesh dependency, and difficulty in constructing approximations with arbitrary order of continuity [42]. Meshfree methods share a common feature that no standard mesh data structures are required to define the discrete approximation spaces, which are constructed based on scattered points (or particles). These methods provide considerable advantages over traditional FEM for solving problems involving large deformations, damage, h-adaptive refinement, and evolving discontinuities. The Reproducing Kernel Particle Method (RKPM) [43, 44, 45, 81] is a prominent representative of a class of Meshfree methods, and is presented in what follows.

3.2.1 RKPM

We assume that the problem domain (in our case, the solid domain Ω^s) is discretized by a set of $\mathrm{n_{np}}$ Lagrangian particles. An RKPM basis function associated with a given particle A, $\Psi_A(\mathbf{x})$, is constructed by multiplying a kernel function $\Phi_a(\mathbf{x}-\mathbf{x}_A)$ with a correction function $C(\mathbf{x},\mathbf{x}-\mathbf{x}_A)$ as

$$\Psi_A(\mathbf{x}) = C(\mathbf{x},\mathbf{x}-\mathbf{x}_A)\Phi_a(\mathbf{x}-\mathbf{x}_A). \tag{3.15}$$

The function $C(\mathbf{x},\mathbf{x}-\mathbf{x}_A)$ may be expressed as

$$\begin{aligned} C(\mathbf{x},\mathbf{x}-\mathbf{x}_A) &= \sum_{|\boldsymbol{\alpha}|\leq p} (\mathbf{x}-\mathbf{x}_A)^{\boldsymbol{\alpha}} b_{\boldsymbol{\alpha}}(\mathbf{x}) \\ &= \mathbf{p}^T(\mathbf{x}-\mathbf{x}_A)\mathbf{b}(\mathbf{x}), \end{aligned} \tag{3.16}$$

where $\mathbf{p}(\mathbf{x}-\mathbf{x}_A)$ is the p^{th}-order monomial basis vector, $\mathbf{b}(\mathbf{x})$ is the unknown coefficient vector, $\boldsymbol{\alpha}$ is a multi-index, and $|\boldsymbol{\alpha}|$ is its norm. The unknown coefficient vector $\mathbf{b}(\mathbf{x})$ is determined by imposing p^{th}-order polynomial reproducing conditions on the space spanned by RKPM basis functions, namely,

$$\sum_{A=1}^{\mathrm{n_{np}}} \Psi_A(\mathbf{x})\mathbf{x}_A^{\boldsymbol{\alpha}} = \mathbf{x}^{\boldsymbol{\alpha}}, \quad |\boldsymbol{\alpha}| \leq p, \tag{3.17}$$

or, equivalently,

$$\sum_{A=1}^{\mathrm{n_{np}}} \Psi_A(\mathbf{x})\mathbf{p}(\mathbf{x}-\mathbf{x}_A) = \mathbf{p}(\mathbf{0}). \tag{3.18}$$

Substituting the expression for $\Psi_A(\mathbf{x})$ from Eq. (3.15) into Eq. (3.18), and solving for $\mathbf{b}(\mathbf{x})$, gives

$$\mathbf{b}(\mathbf{x}) = \mathbf{M}^{-1}(\mathbf{x})\mathbf{p}(\mathbf{0}), \tag{3.19}$$

where the moment matrix $\mathbf{M}(\mathbf{x})$ is given by

$$\mathbf{M}(\mathbf{x}) = \sum_{A=1}^{\mathrm{n_{np}}} \mathbf{p}(\mathbf{x}-\mathbf{x}_A)\mathbf{p}^T(\mathbf{x}-\mathbf{x}_A)\Phi_a(\mathbf{x}-\mathbf{x}_A). \tag{3.20}$$

The moment matrix is invertible at location $\mathbf{x}$ if the reproducing conditions given by Eq. (3.17) are linearly independent [82, 81]. An explicit form of the RKPM basis functions is obtained by substituting the result from Eq. (3.19) into Eq. (3.15):

$$\Psi_A(\mathbf{x}) = \mathbf{p}^T(\mathbf{0})\mathbf{M}^{-1}(\mathbf{x})\mathbf{p}(\mathbf{x}-\mathbf{x}_A)\Phi_a(\mathbf{x}-\mathbf{x}_A). \tag{3.21}$$

For the kernel function we choose a radial cubic B-spline, namely,

$$\Phi_a(\mathbf{x}-\mathbf{x}_A) = \tilde{\Phi}_a(s) = \begin{cases} \frac{2}{3} - 4s^2 + 4s^3, \ 0 \leqslant s \leqslant \frac{1}{2} \\ \frac{4}{3}(1-s)^3, \ \frac{1}{2} \leqslant s \leqslant 1 \\ 0, \text{ otherwise} \end{cases}, \tag{3.22}$$

where

$$s = \frac{\|\mathbf{x}-\mathbf{x}_A\|}{a} \tag{3.23}$$

and a is the support radius. More discussion on the choice of the kernel function may be found in [43]. Note that the continuity of the RKPM discretization is inherited by that of the kernel function, and thus arbitrarily smooth discretizations that are independent of the order of approximation may be easily constructed.

The discrete RKPM solution $u^h(\mathbf{x})$ is given by

$$u^h(\mathbf{x}) = \sum_{A=1}^{\mathrm{n_{np}}} \Psi_A(\mathbf{x})u_A \tag{3.24}$$

where u_A's are the unknown DOFs associated with Lagrangian particles. As in the case of NURBS-based IGA, RKPM basis functions are generally non-interpolatory at the Lagrangian-particle locations.

3.2.2 Domain integration for RKPM

As shown in the previous section, the RKPM basis functions are constructed directly in the physical domain without the requirement of an underlying mesh and the corresponding data structures. While this flexibility makes RKPM attractive for approximating large deformation and fragmentation of the material, it also leads to challenges associated with domain integration. The fact that the RKPM basis functions are non-polynomial (see Eq. (3.18) for their structure) leads to additional challenges for domain integration.

Domain integration in RKPM is usually carried out using either Gaussian quadrature or nodal integration. To carry out Gaussian quadrature one needs to generate a background mesh, which, in some sense, goes against the philosophy of Meshfree methods. In addition, in order to reap the full benefits of Gaussian quadrature, the integration cells need to be aligned with the supports of the RKPM basis functions, which is not easily accomplished.

On the other hand, pure nodal integration, despite its efficiency, exhibits low convergence rates and rank instability [83]. Special techniques have been developed for RKPM in recent years to circumvent these issues. These include Stabilized Conforming Nodal Integration (SCNI) [84], Stabilized Non-Conforming Nodal Integration (SNNI) [85], Variationally Consistent Integration (VCI) [84, 86, 87], and Naturally Stabilized Nodal Integration (NSNI) with VCI correction [88] techniques, among others. The main idea of the SCNI technique is to "smooth" the basis-function gradient over conforming integration cells that partition the problem domain. The smoothed gradient $\tilde{\nabla}$ in each integration cell Ω_A is computed using the divergence theorem as follows

$$\tilde{\nabla}\Psi_B(\mathbf{x}_A) = \frac{1}{|\Omega_A|}\int_{\Omega_A} \nabla\Psi_B \, d\Omega = \frac{1}{|\Omega_A|}\int_{\partial\Omega_A} \Psi_B \mathbf{n} \, d\Gamma, \tag{3.25}$$

where $|\Omega_A|$ is the area in 2D or volume in 3D of the integration cell corresponding to node A, $\mathbf{n}$ is the unit outward normal to the cell boundary $\partial\Omega_A$, and index B points to all RKPM basis functions that are supported in Ω_A. The conforming integration with strain smoothing satisfies the so-called integration constraint, which ensures that the patch tests are satisfied. Strain smoothing also avoids taking direct derivatives at the Lagrangian nodes. (Doing so in the Lagrangian setting yields instability in the Galerkin solution due to severe underestimation of the strain energy of short-wavelength modes.) While SCNI preserves first-order exactness, for problems involving very large deformation or fragmentation the requirement of conforming cells is challenging to maintain because these need to be periodically regenerated during the simulation. For these reasons, SNNI was introduced in [85], and presents a simplification of SCNI in that the smoothing zones, which are typically simple geometric shapes, are no longer required to be conforming. However, relaxation of the conforming-cell condition can yield non-convergent solutions, because the integration constraint, and thus the linear exactness in the Galerkin solution, are no longer satisfied. Recently, in [88], the authors developed the NSNI technique that overcomes the instabilities of nodal integration by introducing a first-order Taylor expansion of the strains in the internal virtual-work terms. This approach introduces higher-order derivatives in the formulation, which may be accommodated in the RKPM and IGA frameworks since both employ smooth discretizations. An implicit gradient [89] has been introduced in NSNI to avoid taking higher-order derivatives of the shape functions.

3.3 Numerical aspects of IGA-RKPM coupling

In this section we focus on the numerical aspects of air-blast FSI that specifically pertain to the IGA-RKPM coupling. We repeat the semi-discrete formulation of the coupled problem from chapter 2 of this paper for convenience: Find $\mathbf{Y}^h \in \mathcal{S}^h$, such that $\forall \mathbf{W}^h \in \mathcal{V}^h$,

$$
\begin{aligned}
& M^f_{\Omega}(\mathbf{W}^h, \mathbf{Y}^h) + B^f_{\Omega}(\mathbf{W}^h, \mathbf{Y}^h) - F^f_{\Omega}(\mathbf{W}^h) + B^{st}_{\Omega}(\mathbf{W}^h, \mathbf{Y}^h) + B^{dc}_{\Omega}(\mathbf{W}^h, \mathbf{Y}^h) \\
& \qquad + \\
& M^s_{\Omega^s}(\mathbf{W}^h, \mathbf{Y}^h) + B^s_{\Omega^s}(\mathbf{W}^h, \mathbf{Y}^h) - F^s_{\Omega^s}(\mathbf{W}^h) \\
& \qquad - \\
& M^f_{\Omega^s}(\mathbf{W}^h, \mathbf{Y}^h) + B^f_{\Omega^s}(\mathbf{W}^h, \mathbf{Y}^h) - F^f_{\Omega^s}(\mathbf{W}^h) + B^{st}_{\Omega^s}(\mathbf{W}^h, \mathbf{Y}^h) + B^{dc}_{\Omega^s}(\mathbf{W}^h, \mathbf{Y}^h) \\
& \qquad + \\
& \int_{\tilde{\Gamma}^f} \beta h \, [[\mathbf{w}^h_{,i} n_i]] \cdot [[\mathbf{u}^h_{,j} n_j]] \, d\tilde{\Gamma} \\
& \qquad = \\
& \qquad 0,
\end{aligned}
\tag{3.26}
$$

where $\mathbf{Y}^h$ is the discrete vector-valued trial function corresponding to pressure-primitive variables, $\mathbf{W}^h$ is the discrete vector-valued test function, and $\mathcal{S}^h$ and $\mathcal{V}^h$ are the associated discrete function spaces. We remind the reader that superscript f refers to the fluid, and s to the solid parts of the problem, and Ω is the background domain occupied by the fluid and partially covered by the Lagrangian particles of the solid domain Ω^s.

We summarize the important IGA-RKPM coupling aspects in what follows:

- The spaces of discrete trial and test functions are defined on the background domain Ω, resulting in the FSI problem DOFs residing on the background mesh. Equal-order NURBS discretization is employed for all the unknowns in the variable set $\mathbf{Y}^h$.

- The terms on the first line of Eq. (6.26) are evaluated over the entire background NURBS domain using Gaussian quadrature with $p+1$ points in each tensor-product direction. More efficient quadrature rules are also possible (see [78, 79] for recent advances in numerical integration for IGA).

- The terms on the second and third lines of Eq. (6.26) are evaluated using RKPM domain-integration techniques. Nodal integration is performed *using the RKPM Lagrangian points* with two options for the background NURBS basis-function gradient evaluation: 1. Direct evaluation at the location corresponding to that of the Lagrangian

particle; 2. Smoothed definition as per Eq. (3.25) with the smoothing zone of simple shape constructed around each Lagrangian particle in the spirit of SNNI. We found that Option 1 is more economical and delivers stable results in the present setting. We are, however, aware of the potential instabilities and inaccuracies associated with this type of integration, and plan to explore an NSNI-type approach in the future work.

- The terms on the fourth line, which correspond to ghost-velocity stabilization [62], are identically zero because the basis functions employed in our discretization are smooth. In principle, the generalization of ghost penalties to higher-order bases involves jumps of higher derivatives, leaving nonzero terms even for spline spaces of maximal continuity. (See, e.g., Remark 1 in [90] or Eq. (11) in [91].) Although we are aware of this generalization, we did not find penalization of jumps in higher derivatives necessary in the present framework.

- Domain integration of the terms on the second and third lines of Eq. (6.26) require the evaluation of the determinant of the deformation gradient from the solid reference to its current configuration at a Lagrangian-node location $\mathbf{X}_A$, which is the nodal quadrature point. In this work the deformation gradient is taken directly from the foreground RKPM discretization, and may be expressed as

$$\mathbf{F}(\mathbf{X}_A) = \frac{\partial \mathbf{x}}{\partial \mathbf{X}}(\mathbf{X}_A) = \sum_{B=1}^{\mathrm{n_{np}}} \mathbf{x}_B \frac{\partial \Psi_B}{\partial \mathbf{X}}(\mathbf{X}_A), \tag{3.27}$$

  where the above sum is performed only over the RKPM basis functions supported at location $\mathbf{X}_A$ in the reference configuration. Note that only the current position of the Lagrangian particle $\mathbf{x}_B$ and the RKPM basis-function gradient with respect to the spatial coordinates of the reference configuration $\mathbf{X}$ are required to evaluate the above expression. In our computations, the RKPM basis-function gradient is replaced by its smoothed counterpart over the integration cell in the reference configuration as per Eq. (3.25), and is computed only once in the beginning of the simulation for efficiency.

  As an alternative approach, the determinant of the deformation gradient may be computed from the generating equation for $\mathbf{F}$ (see, e.g., [52])

$$\left.\frac{\partial \mathbf{F}}{\partial t}\right|_{\mathbf{X}} = \nabla \mathbf{u}\, \mathbf{F}, \tag{3.28}$$

  or for the determinant itself,

$$\left.\frac{\partial J}{\partial t}\right|_{\mathbf{X}} = \nabla \cdot \mathbf{u}\, J. \tag{3.29}$$

  Definitions in Eqs. (6.28) and (3.29) do not rely on the discretization of the solid domain and may be better suited when fragmentation scenarios are simulated.

- Stress update described in chapter 2 is performed at the Lagrangian nodes of the foreground discretization where the history variables are stored. If damage is included in the modeling, which is not the case in the present paper,

the corresponding history variables would also be stored at the same locations.

3.4 Numerical examples

In this section we present one 1D and five 2D computational examples that demonstrate the capabilities, robustness, and accuracy of IGA-RKPM coupling for air-blast FSI. The computational examples are: Sod shock tube, Sedov blast, Taylor bar impact, chamber detonation, flexible panel subjected to a shock load, and detonation with multiple objects. The first three examples test the accuracy of standalone compressible-flow and solid mechanics formulations. Examples four and five are the same as in reference Kazem. The former example demonstrates the ability of the proposed framework to produce convergent FSI solutions under mesh refinement, while the latter example validates the formulation using experimental data. The final example, which is similar to the one presented in reference Kazem, shows the ability of the proposed methodology to handle blast in the presence of multiple objects without restriction on their motion and including contact between the objects. C^1-continuous quadratic NURBS and RKPM functions with linear consistency and kernel given by Eq. (3.22) are employed in all computations. Unless otherwise stated, in all computations the fluid is assumed to have properties of air with constant viscosity $\mu = 1.81 \times 10^{-5}$ kg/(m s), Prandtl number 0.72, and adiabatic index $\gamma = 1.4$. The time step for each problem is selected from considerations of stability and two-to-four explicit corrector passes are employed in the computations.

3.4.1 Sod shock tube problem

We compute a 1D Sod shock tube problem [92], which is an inviscid hydrodynamics example. At the initial time, two material states are prescribed on each half of a unit-length domain. As time evolves, a rarefaction wave, contact discontinuity and shock discontinuity are formed in the domain. On the left, the initial conditions are $\rho = 1.0$, $v = 0.0$, and $p = 1.0$, while on the right, the initial conditions are $\rho = 0.1$, $v = 0.0$, and $p = 0.125$. (The problem is specified in non-dimensional units.) The discretization consists of 300 uniform elements, and the numerical results at time $t = 0.2$ are compared to the analytical solution in Figure 3.1. As can be seen in the figure, the numerical results have no oscillations, and match the exact solution very well.

3.4.2 Sedov blast problem

We compute the 2D inviscid Sedov blast problem [93] on a square domain with edge length $L = 1.1$. A sudden release of energy at the origin creates an expanding shock wave. The initial conditions of the problem consist of zero velocity field and a Dirac-delta distribution of the internal-energy density at the origin so the total energy is equal to 0.25. (The problem is also specified in non-dimensional units.) The initial density is set to $\rho = 1$, the temperature is set consistent with the internal energy density, and pressure is set consistent with the ideal gas law. Meshes of 64×64,

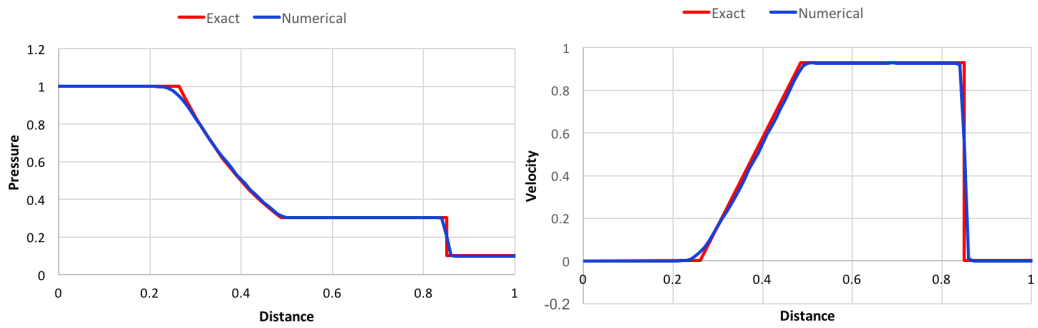

(a) Pressure (b) Velocity

(c) Density (d) Internal Energy

Figure 3.1: Sod shock tube problem in 1D. Solution at time $t = 0.2$

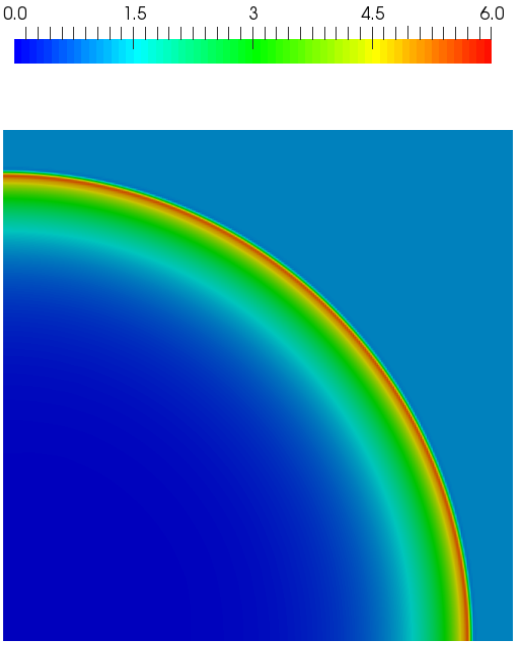

Figure 3.2: Sedov blast problem in 2D. Density contours at time $t = 1.0$.

128×128, and 256×256 elements are employed in the computations. Figure 3.2 shows the density contours at time $t = 1.0$ on the mesh of 256×256 elements. The solution appears to be smooth, stable, and radially symmetric. Figure 3.3 shows the scatter plot of density vs. distance from the origin at time $t = 1.0$ for all three meshes. Convergence to the

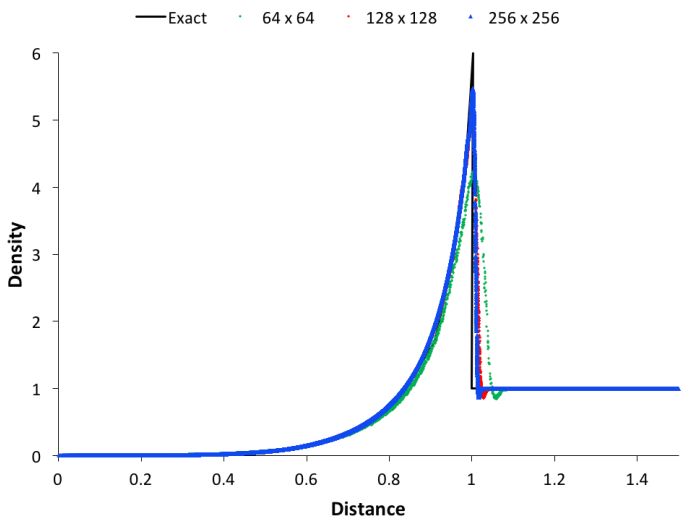

Figure 3.3: Sedov blast problem in 2D. Scatter plot of density vs. radial coordinate for the three meshes employed. The exact solution is also plotted to illustrate convergence with mesh refinement.

Table 3.1: Taylor bar impact. Material properties.

Young's modulus E	200 GPa
Poisson's ratio ν	0.30
Density ρ	2700 kg/m^3
Yield stress σ_y	0.29 GPa
Hardening modulus h	0.1 GPa

analytical result is evident from the plot. Very little scatter in the data is also observed, suggesting the methodology has excellent symmetry preservation properties.

3.4.3 Taylor bar impact

We simulate a steel bar impacting a rigid wall at the initial velocity of 227 m/s. The bar has an initial height of 32 mm, width of 6.4 mm, and is discretized using 250×150 particles. The background domain has a height of 36 mm, width of 21 mm, and is discretized using 77×45 elements.

No-penetration and zero tangential-stress boundary conditions are applied at the bottom wall. The bar is also assumed to be placed in vacuum, that is, only the solid mechanics equations are solved without contributions from the surrounding fluid. Figure 3.4 shows the problem setup while Figure 3.5 shows the background and foreground problem meshes. The material properties are summarized in Table 3.1.

Results of the immersed approach are compared with those obtained by solving the problem using a Lagrangian RKPM formulation. The Taylor-bar height and width time histories are plotted in Figure 3.6. Excellent agreement between the two computations is achieved for these quantities. Figure 3.7 shows the final deformed shape of the Taylor bar with a zoom on the impact region where most of the deformation occurs. The immersed and RKPM computations are in very good agreement with each other, demonstrating that the immersed methodology is capable of accurately

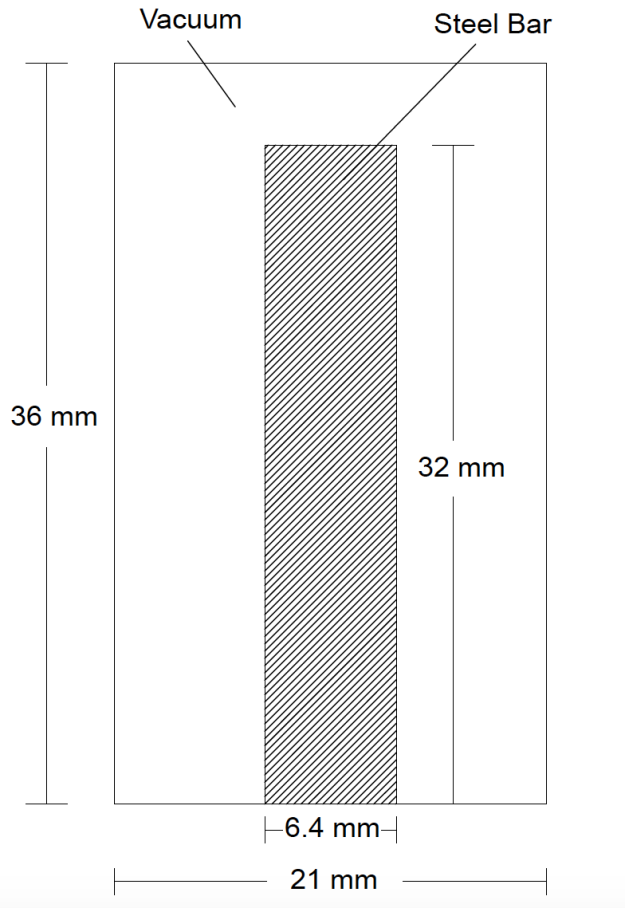

Figure 3.4: Taylor bar impact. Problem setup.

Table 3.2: Chamber detonation. Material properties of a steel bar.

Young's modulus E	200 GPa
Poisson's ratio ν	0.29
Density ρ	7870 kg/m^3
Yield stress σ_y	0.4 GPa
Hardening modulus h	0.1 GPa

capturing the solid plastic deformations.

3.4.4 Chamber detonation

In this coupled FSI example, a steel bar is subjected to a detonation blast load. A bar with dimensions 0.2 m $\times$ 0.1 m is placed at the center of a closed chamber with dimensions 0.4 m $\times$ 0.4 m. The bar thickness is set to 3.5 mm. Figure 3.8 shows the problem description. The bar material properties correspond to those of steel, and are summarized in Table 3.2. The air in the chamber is initially at rest with $T = 270$ K and $p = 100,000$ Pa. The detonation is initiated by setting higher-than-ambient values of the pressure, $p = 6,746,268.65$ Pa, and temperature, $T = 1,465$ K, in a semi-circular region centered on the left wall and with radius of 6.1 mm. Free-slip and no-penetration boundary

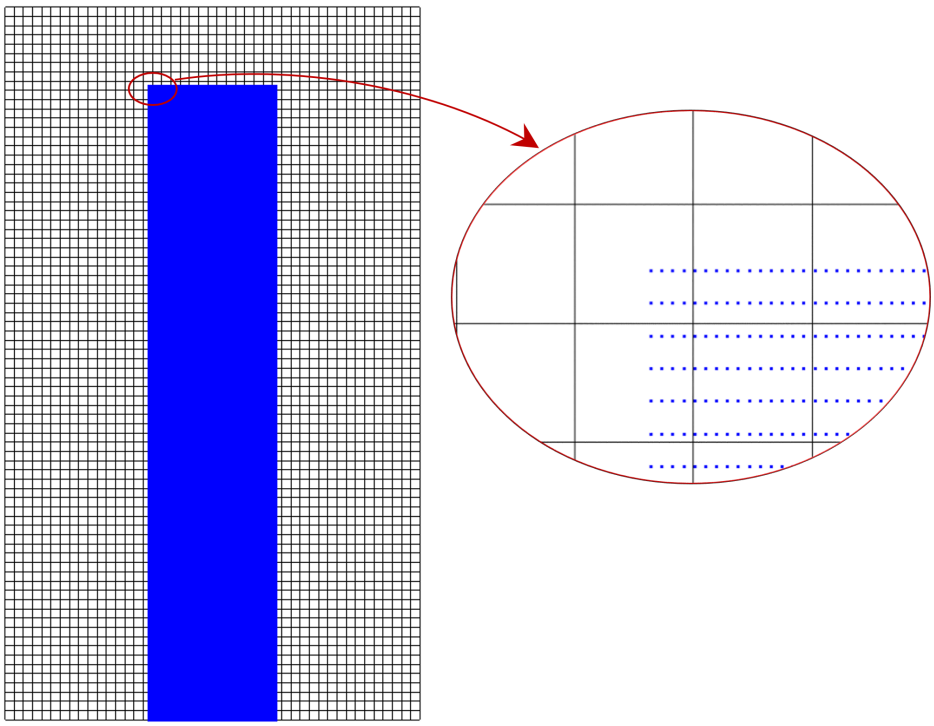

Figure 3.5: Taylor bar impact. Background and foreground problem meshes.

Table 3.3: Shock wave impacting an elastic panel. Material properties of the steel panel.

Young's modulus E	220 GPa
Poisson's ratio ν	0.33
Density ρ	7600 kg/m^3

conditions are assumed at the chamber walls.

Four problem discretizations with increasing mesh refinement levels are considered: 1) Fluid: 40×40 elements; Solid: 53×26 particles; 2) Fluid: 80×80 elements; Solid: 105×53 particles; 3) Fluid: 120×120 elements; Solid: 158×79 particles; 4) Fluid: 160×160 elements; Solid: 210×105 particles. Figure 3.9 shows the air pressure at different time instants and the final, deformed shape of the bar computed on the finest mesh. Note the "mushrooming" at the left edge of the bar and very large deformation at the bar corners. Also note the permanent indentation on the right edge of the bar resulting from shock waves bouncing off the right wall and impacting the specimen.

Figure 3.10 shows the time history of the bar center-of-mass displacement, and pressure at the detonation center (Point 1 in the figure) and right-wall center (Point 2 in the figure). The results exhibit good convergence with mesh refinement, and are in good agreement with the ALE results from reference Kazem. Shock waves bouncing between the right wall and moving bar are captured very well in the simulations.

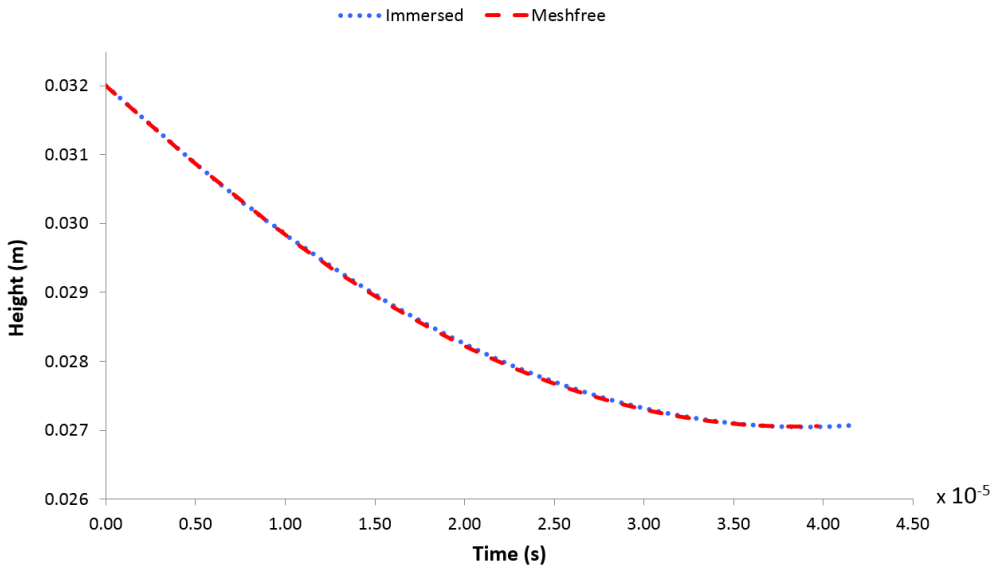

(a)

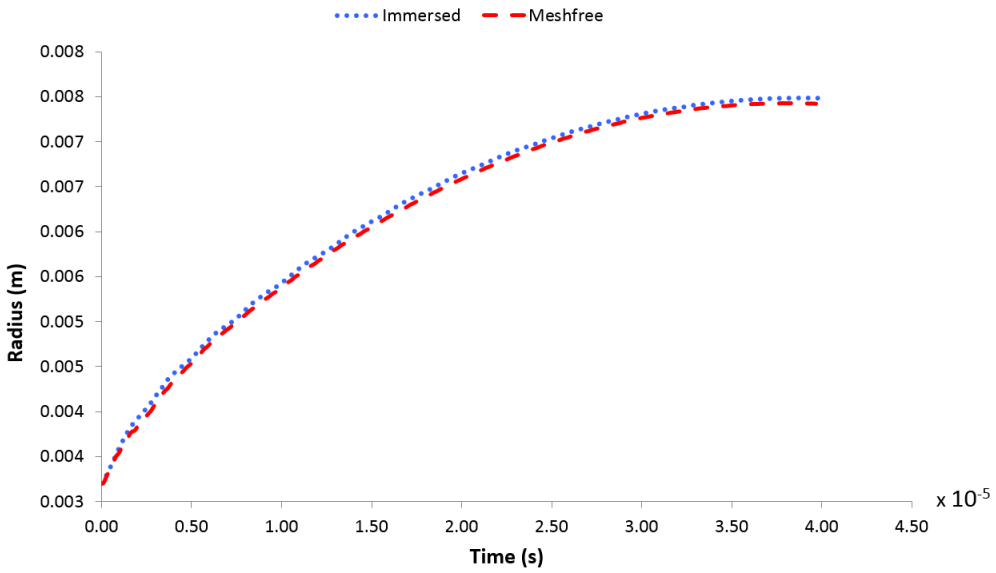

(b)

Figure 3.6: Taylor bar impact. Comparison of the time history of Taylor bar height (a) and width (b) between the immersed and Lagrangian RKPM simulations.

3.4.5 Shock wave impacting an elastic panel

In this example, a thin steel panel is impacted by a planar shock wave in air. The problem setup is shown in Figure 3.11. The panel thickness is 1 mm, and it extends 40 mm from a mounting point with forward-facing step geometry where it is clamped. The fluid domain has dimensions 600 mm × 80 mm. The step has a height of 15 mm and starts 335 mm from the left boundary. Inflow boundary conditions are applied on the left side while rigid-wall boundary conditions are applied elsewhere. In this example the panel material is assumed to be elastic with the properties given

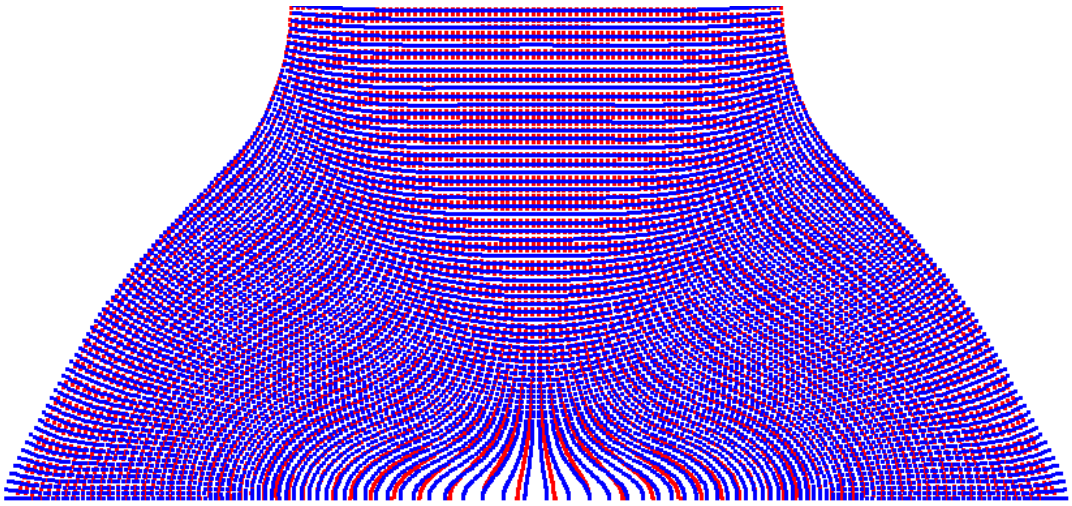

Figure 3.7: Taylor bar impact. Overlapping, deformed configurations of the Taylor bar from the immersed (blue) and RKPM (red) simulations. Zoom on the region near the impact where most of the deformation occurs.

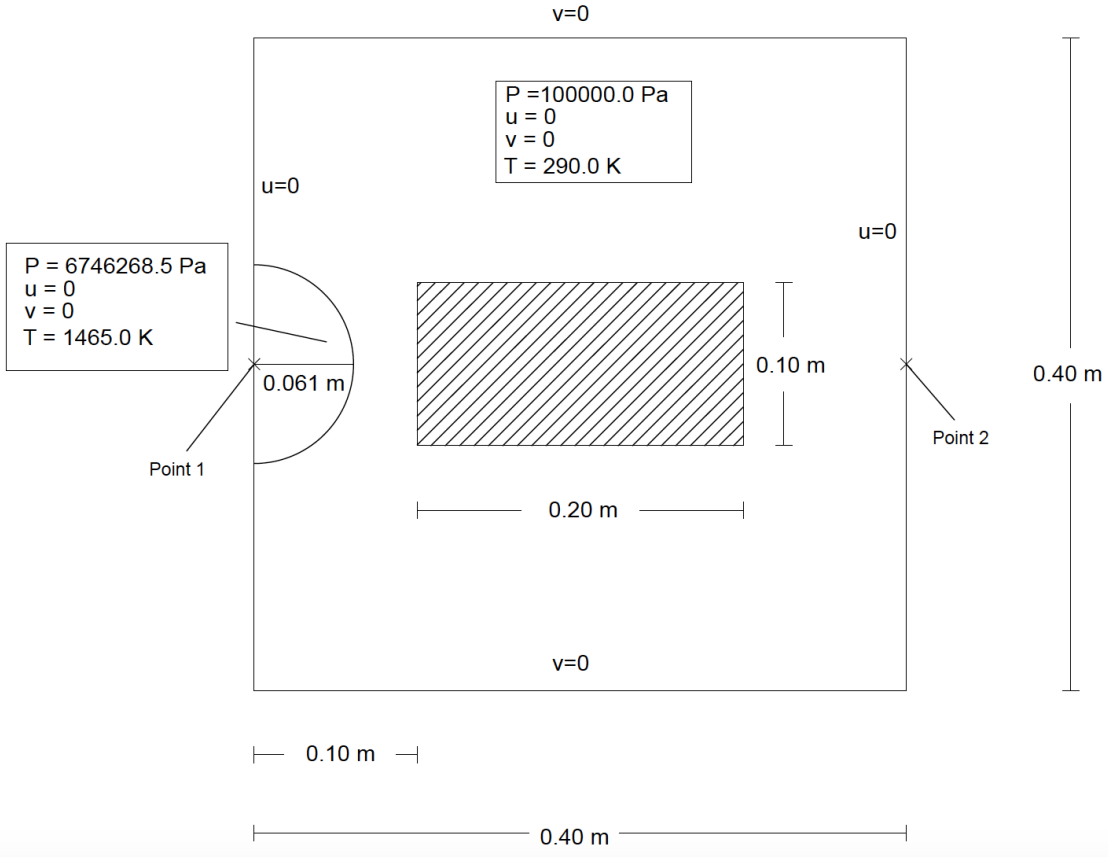

Figure 3.8: Chamber detonation. Problem setup and dimensions.

in Table 3.3. The shock is placed at 330 mm from the left wall and travels into air at rest with density $\rho = 1.2$ kg/m^3 and pressure $p = 100$ kPa. Behind the shock the density is $\rho = 1.6458$ kg/m^3, the pressure is $p = 156.18$ kPa, and the horizontal velocity $v = 112.61$ m/s. The background mesh has 480×64 elements, while the panel foreground mesh makes use of 10×500 Lagrangian particles. The step is modeled in an immersed fashion with zero velocity assigned

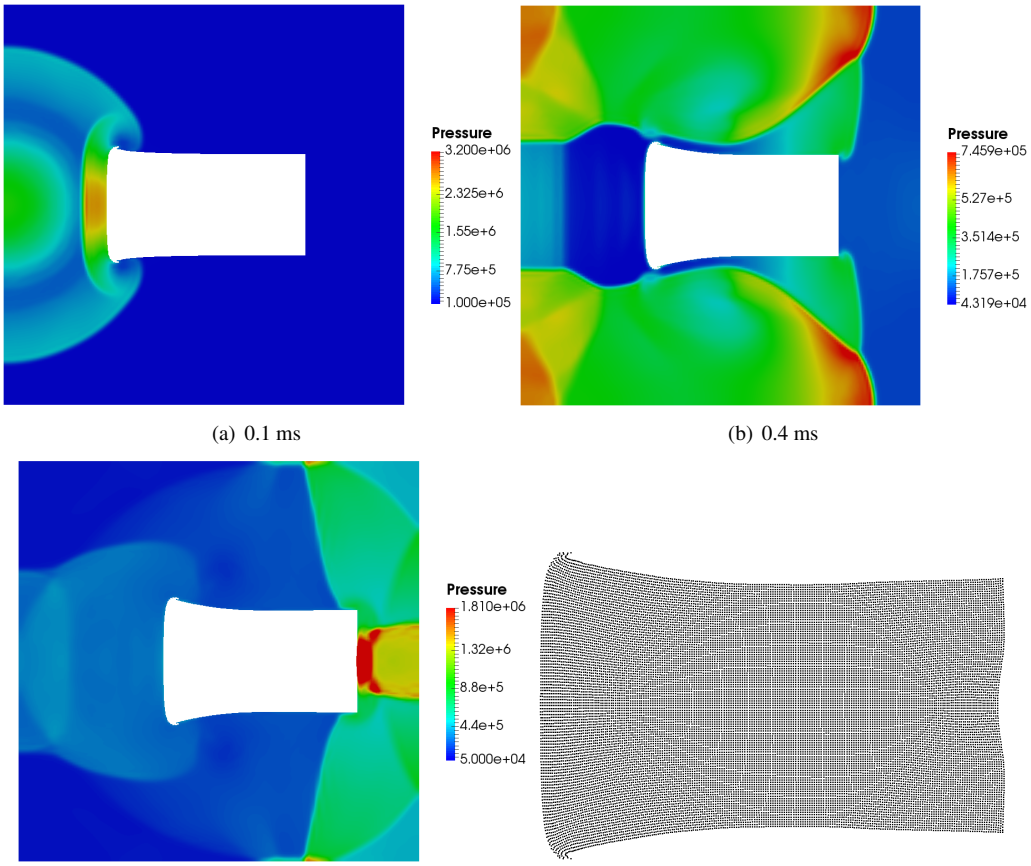

(a) 0.1 ms (b) 0.4 ms

(c) 0.7 ms (d) Final configuration

Figure 3.9: Chamber detonation. Pressure at different time instants and final, deformed configuration of a steel bar.

to the block of control points corresponding to the step location. The problem has been previously investigated both experimentally and numerically in [94, 95], and is also computed in reference Kazem.

Figure 3.12 shows the pressure field and panel displaced configuration at different time instants. After the initial impact of the shock wave the panel begins to oscillate. Figure 3.13a shows a comparison of the computed and measured panel-tip displacement time histories. The two quantities are in good agreement, both in terms of the oscillation magnitude and frequency, suggesting that the background mesh is sufficiently fine to provide the appropriate level of the panel through-thickness resolution. Figure 3.13b shows a comparison of the computed and measured pressure time histories at the pressure-sensor position. Very good agreement is obtained in this case as well, suggesting that the complex dynamics of shocked flow is well captured in the simulation.

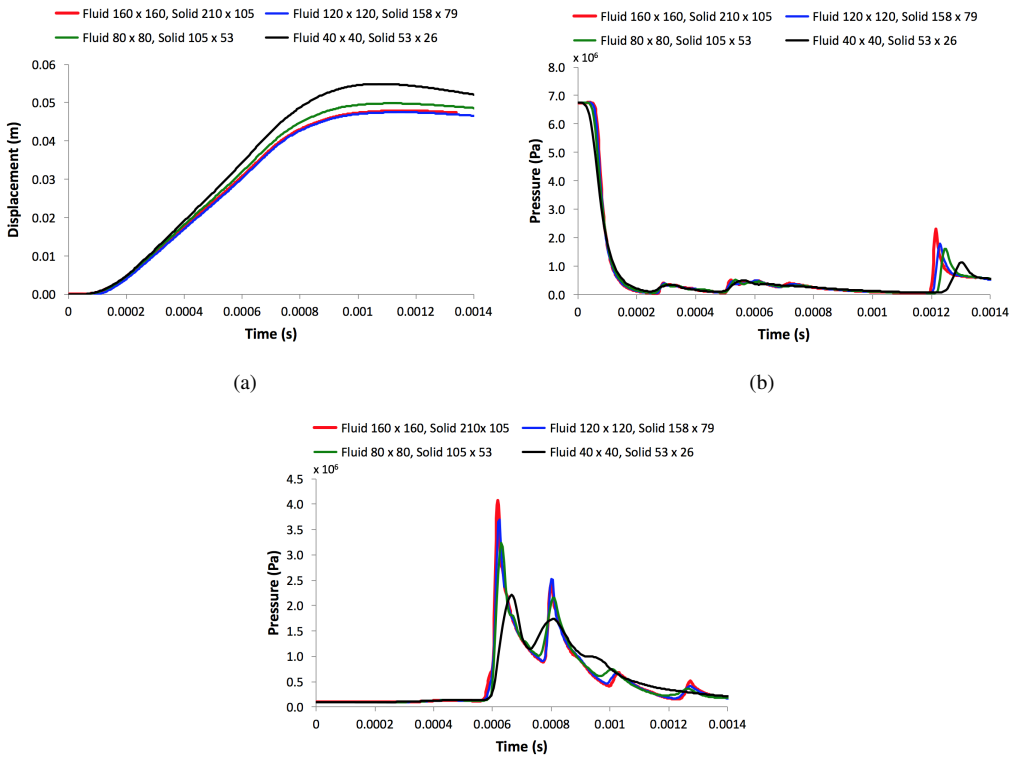

Figure 3.10: Chamber detonation. (a) Horizontal displacement of the bar center of mass; (b) Pressure at the center of detonation; (c) Pressure at the center of the right wall.

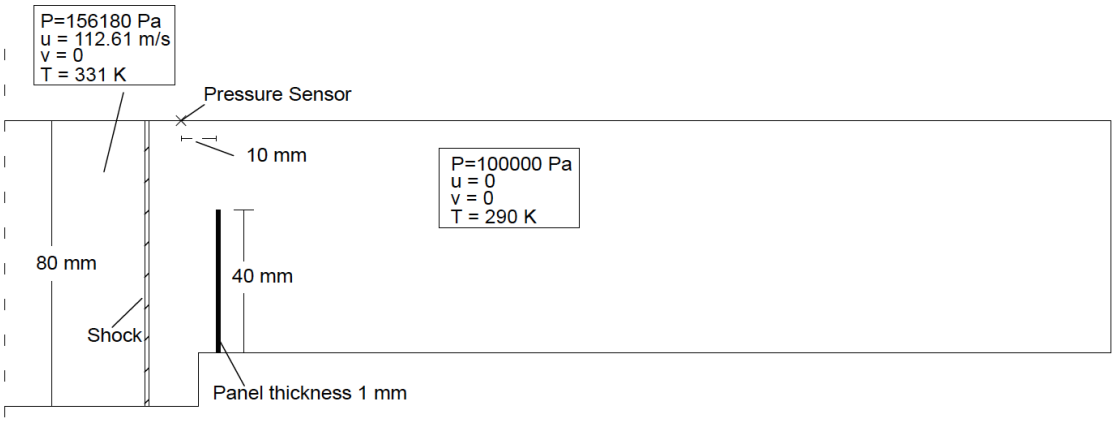

Figure 3.11: Shock wave impacting an elastic panel. Problem setup.

3.4.6 Detonation with multiple objects

This last example shows the ability of the proposed method to naturally handle scenarios of detonation in the presence of multiple objects. Several rectangular objects are placed in a rectangular chamber with dimensions 1.2 m $\times$ 0.8 m, and are subjected to a detonation load. Figure 3.14 shows the problem setup. The largest objects have dimensions 0.26 m $\times$ 0.075 m, the smallest ones 0.0375 m $\times$ 0.05 m, and the rest 0.075 m $\times$ 0.1 m. The detonation is initiated by assuming air at rest with $T = 270$ K and $p = 100{,}000$ Pa, and elevating the pressure to $p = 11.0$ MPa

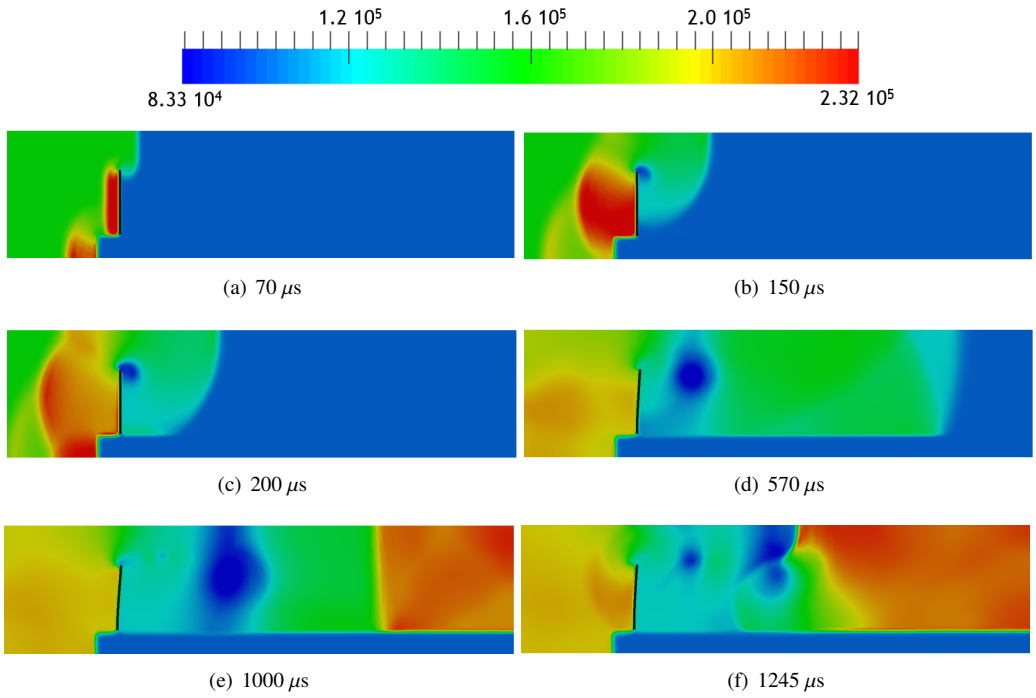

(a) 70 μs (b) 150 μs

(c) 200 μs (d) 570 μs

(e) 1000 μs (f) 1245 μs

Figure 3.12: Shock wave impacting an elastic panel. Pressure field and deflected panel at different time instants.

and temperature to $T = 1,550$ K in the zone of radius 0.05 m. All objects are assumed to have the material properties of steel, and are modeled as elastic. Slip boundary conditions are applied at the chamber walls. Uniform mesh with dimension 0.006 m for the air and 0.0034 m for the solid objects is employed for the problem discretization.

Figure 3.15 shows the air speed and the solid deformed configuration at different instants after the detonation is initiated. The solid objects contact each other, impact the chamber walls, and, in general, move without any restrictions under the action of blast waves. The flow solution remains stable with crisp resolution of the shock waves throughout the computation.

3.5 Conclusions

A computational framework for ABSI based on an immersed approach, which models the interaction of compressible flow in the high-Mach-number regime with inelastic solids and structures, is discretized using the IGA-RKPM coupling. The NURBS-based isogeometric background discretization is fixed and provides the discrete trial and test function spaces for the coupled FSI problem. The RKPM-based foreground discretization is moving with the solid material particles and is employed to track its current position, store history-dependent variables, and perform numerical quadrature.

Several attributes of the coupled IGA-RKPM formulation are exploited to improve the accuracy and robustness of the immersed air-blast FSI framework. Most notably, the higher-order accuracy and smoothness of the background

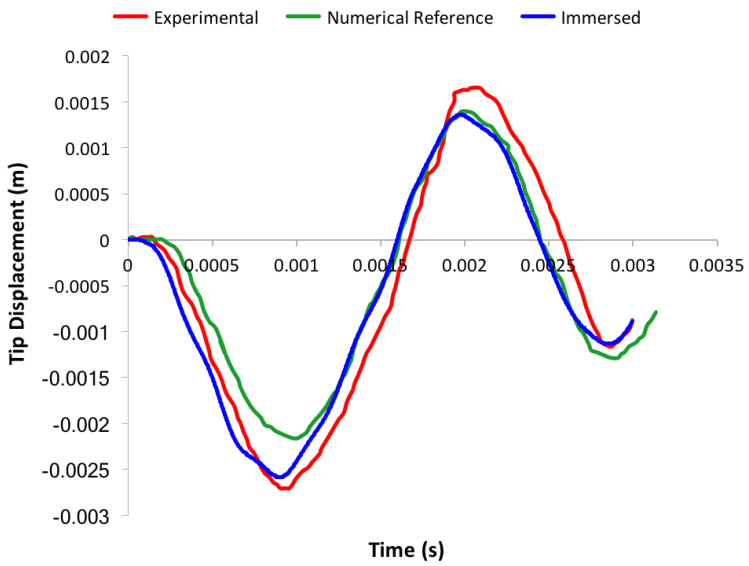

(a)

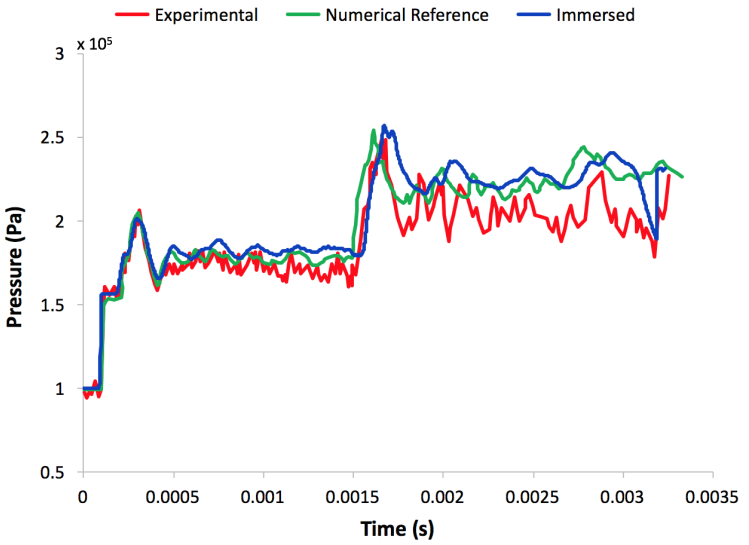

(b)

Figure 3.13: Shock wave impacting an elastic panel. Time history of (a) Panel tip displacement; (b) Pressure at the sensor location. Computational results from [95] are also shown for comparison.

discretization delivers high-quality compressible-flow solutions with shocks. In addition, the higher-order smoothness of the background basis functions gives a continuous representation of the strain-rate field, which greatly improves the quality of the solid mechanics solution. Finally, the ghost velocity stabilization needed for the stability of the C^0-continuous case presented in chapter 2 is completely obviated.

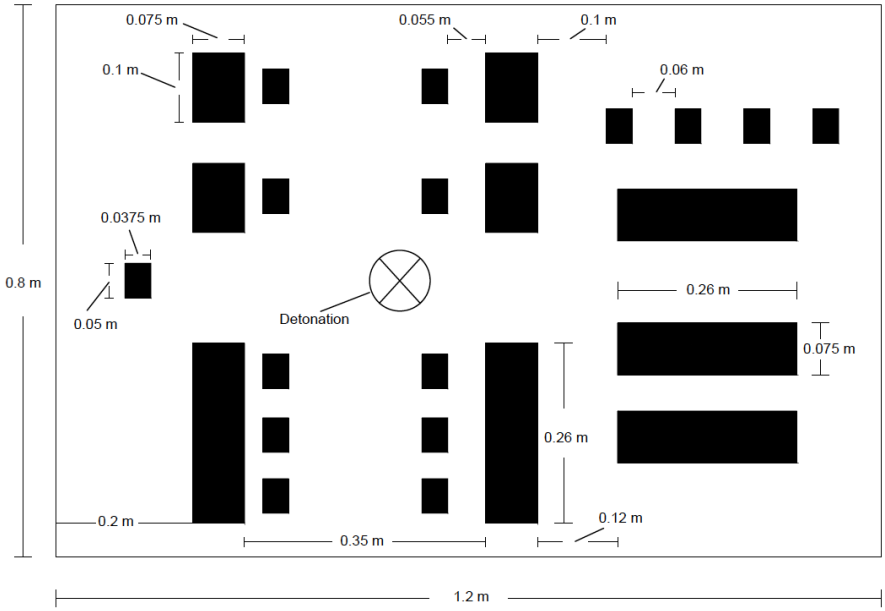

Figure 3.14: Detonation with multiple objects. Problem setup.

3.6 Acknowledgements

Chapter 3, in part, is a reprint of the material as it appears in: "A new formulation for air-blast fluid–structure interaction using an immersed approach: part II–coupling of IGA and meshfree discretizations" (with Y. Bazilevs, J. Bueno, K. Kamran, D. Kamensky, M. Hilman, H. Gomez, and J.S. Chen), *Computational Mechanics*, 60, 2017. The dissertation author was the primary investigator and author of the paper.

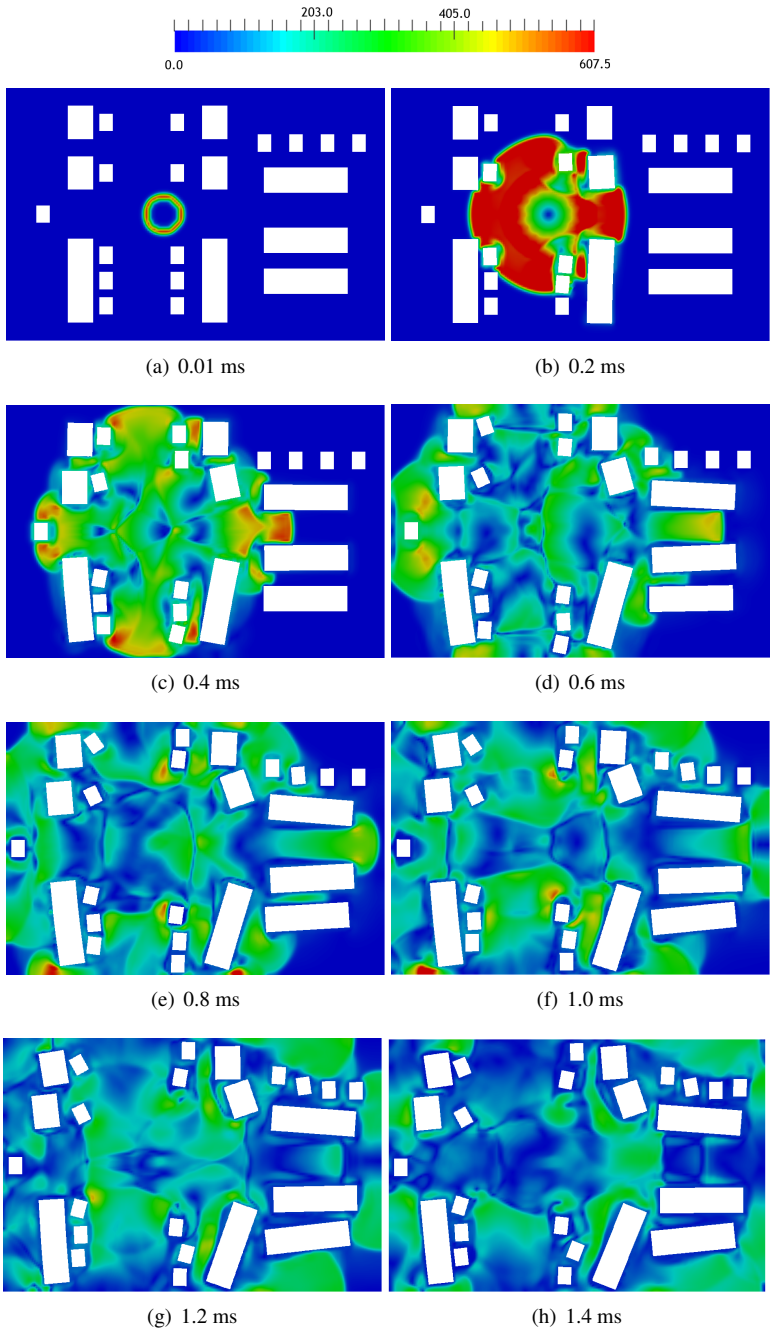

(a) 0.01 ms (b) 0.2 ms

(c) 0.4 ms (d) 0.6 ms

(e) 0.8 ms (f) 1.0 ms

(g) 1.2 ms (h) 1.4 ms

Figure 3.15: Detonation with multiple objects. Air speed and solid in the current configuration at different instants during the simulation.

Chapter 4

Modeling concrete structures subjected to blast loadings

Concrete is a very common construction material when it comes to civil structures. Blast loading on civil structures is a multi-physical process that involves the initiation of a detonation, a shock wave propagation, and an air-blast structure interaction that can result in damage, fragmentation, progressive collapse of the concrete structure, and even in human casualties. In this chapter we present the basics of a concrete model as well a high explosive modeling technique. At the end of the chapter a numerical example is presented and demonstrates that the approach is capable of reproducing all the major qualitative characteristics of blast on concrete structures.

4.1 Concrete constitutive modeling

A three invariant smooth cap model based on [96, 50] is presented here. This model has been shown to be capable of adequately modeling damage-based softening and modulus reduction, shear compaction, and strain rate effects [97]. The key points of the model are summarized below:

- **Additive decomposition of the rate-of-deformation tensor**:

$$\mathbf{D} = \nabla^s \mathbf{u} = \frac{1}{2}(\nabla \mathbf{u} + \nabla \mathbf{u}^T) = \mathbf{D}^e + \mathbf{D}^p, \tag{4.1}$$

where $\mathbf{D}^e$ and $\mathbf{D}^p$ are its elastic and plastic components, respectively.

- **Stress-rate constitutive relation**:

$$\boldsymbol{\sigma}^{\nabla J} = \mathbb{C} : \mathbf{D}^e = \mathbb{C} : (\mathbf{D} - \mathbf{D}^p), \tag{4.2}$$

where $\mathbb{C}$ is the constitutive material tensor, and $\boldsymbol{\sigma}^{\nabla J}$ is the objective Jaumann rate of the Cauchy stress [52] given by

$$\boldsymbol{\sigma}^{\nabla J} = \dot{\boldsymbol{\sigma}} - \boldsymbol{\sigma}\boldsymbol{\omega}^T - \boldsymbol{\omega}\boldsymbol{\sigma}, \tag{4.3}$$

where $\dot{\boldsymbol{\sigma}}$ is the material time derivative of the Cauchy stress, and

$$\boldsymbol{\omega} = \frac{1}{2}(\nabla \mathbf{u} - \nabla \mathbf{u}^T) \tag{4.4}$$

is the spin tensor.

- **Yield surface**:

The model is a cap model with a smooth intersection between the failure surface and the hardening cap. The shape of the yield surface in the meridonal plane is shown in Figure 4.1. A multiplicative decomposition that combines the shear surface and the hardening compaction surface smoothly and continuously is used. The smooth intersection helps alleviate the numerical complexity of treating the compressive corner between the shear surface and the cap. The yield surface is a function of all three stress invariants, J_1, $J_2^{'}$, and $J_3^{'}$, that correspond to the first invariant of the stress tensor, the second invariant of the deviatoric stress tensor, and the third invariant of the deviatoric stress tensor respectively.

$$J_1 = 3P \tag{4.5}$$

$$J_2^{'} = \frac{1}{2}\mathrm{tr}(\boldsymbol{\sigma}^{'2}) \tag{4.6}$$

$$J_3^{'} = \det(\boldsymbol{\sigma}^{'}) \tag{4.7}$$

where

$$P = \frac{1}{3}(\mathrm{tr}(\boldsymbol{\sigma})) \tag{4.8}$$

and

$$\boldsymbol{\sigma}^{'} = \boldsymbol{\sigma} - P\mathbf{I} \tag{4.9}$$

Then the three invariant yield function is defined as:

$$f(J_1, J_2^{'}, J_3^{'}, \kappa) = J_2^{'} - R^2 F_f^2 F_c \tag{4.10}$$

F_f is the shear failure surface, F_c is the hardening cap, R is the so-called Rubin scaling factor [96], and κ is the cap hardening parameter and corresponds to the pressure invariant value at the intersection of the cap with the shear failure surface. The multiplicative form of the equation allows the shear surfaces and the cap to take on the same slope at their intersection. The shear failure surface is defined as:

$$F_f(J_1) = \alpha - \lambda \exp(-\beta J_1) + \theta J_1 \tag{4.11}$$

The values of α, β, λ, θ are parameters that depend on the particular concrete strength that is being used and their values can be found in [50]. The purpose of the cap is to model plastic volume change related to pore collapse. The cap surface function is defined as

$$F_c(J_1, \kappa) = 1 - \frac{(J_1 - L(\kappa))(|J_1 - L(\kappa)| + J_1 - L(\kappa))}{2(X(\kappa) - L(\kappa))^2} \tag{4.12}$$

The details of the parameters in the above equation can be found in [50].

- **Flow rule**

$$\mathbf{D}^p = \dot{\gamma} \frac{\partial f}{\partial \boldsymbol{\sigma}}, \tag{4.13}$$

where $\dot{\gamma}$ is the so-called consistency parameter [54] that needs to be determined.

- **Consistency condition**:

$$\dot{f} = \frac{\partial f}{\partial \boldsymbol{\sigma}} : \dot{\boldsymbol{\sigma}} = 0, \tag{4.14}$$

The time discrete counterpart of the consistency parameter $\Delta\gamma$ is determined iteratively through the cutting plane algorithm developed by Simo and Hughes [54].

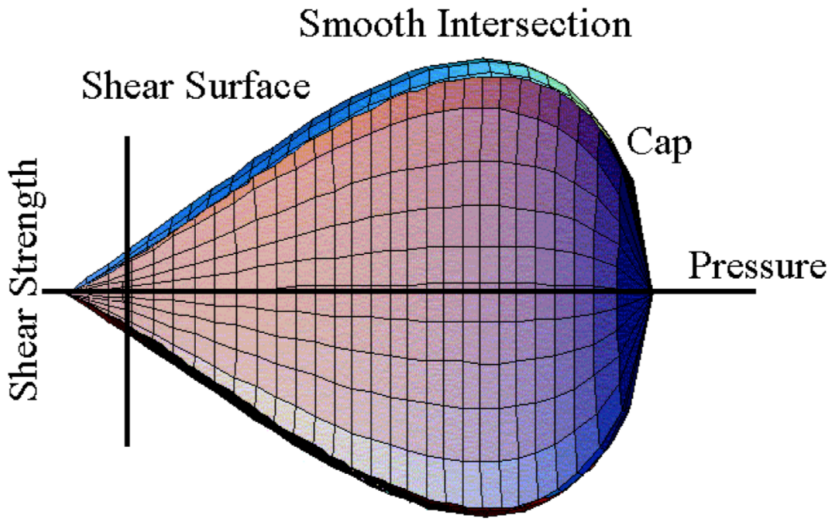

Figure 4.1: General shape of the concrete model yield surface in two dimensions in the meridonal plane [50]

.

- **Viscoplastic rate effects**

  Concrete has been shown to have higher strength and stiffness when the loading rate is very high, which is the case of blast loading. Rate effects are modeled through a viscoplastic formulation that interpolates between the elastic trial stress and the plastic stress without rate effects. The viscoplastic stress is then defined as

$$\boldsymbol{\sigma}^{vp} = (1-\gamma)\boldsymbol{\sigma}^{T} + \gamma\boldsymbol{\sigma}^{p} \tag{4.15}$$

  where $\boldsymbol{\sigma}^{vp}$ is the viscoplastic stress with rate effects, $\boldsymbol{\sigma}^{T}$ is the elastic trial stress, and $\boldsymbol{\sigma}^{p}$ is the plastic stress obtained from the return mapping algorithm. The details of calculating the value of parameter γ can again be found in [50].

- **Damage formulation**

$$\boldsymbol{\sigma}^{d} = (1-d)\boldsymbol{\sigma}^{vp} \tag{4.16}$$

  The damage formulation models both strain softening and modulus reduction. The scalar parameter d transforms the viscoplastic stress tensor without damage $\boldsymbol{\sigma}^{vp}$, to the stress tensor with damage $\boldsymbol{\sigma}^{d}$. The damage parameter ranges from zero for intact specimens to 1 for fully damaged ones. Damage initiates and accumulates when strain-based energy terms exceed the specified damage thresholds. Two damage formulations exist; one corresponding to brittle damage and the other corresponding to ductile damage. Brittle damage accumulates when the pressure (P) is tensile while ductile damage accumulates when the pressure is compressive. For more details on the

damage thresholds and on the softening functions that correspond to brittle and ductile damage the interested reader should consult [50].

4.2 High explosive (HE) modeling

The HE modeling process starts with a chemical reaction that converts the explosives into gas products at high pressure and temperature. The process has three zones that can be seen in Figure 4.2 and in [98]; the original high explosive zone, the reaction zone, and the detonation-produced explosive gas zone. The detonation is the propagation of the reactive wave through the explosive with constant velocity, the detonation velocity. In this work it is assumed that the chemical reaction and the entire detonation process have already taken place and all the explosives are assumed to have already been converted to gaseous products in their entirety. According to [99] the pressure transient behind the detonation wave is given by:

$$P(x) = \frac{16}{27}\frac{\rho_0}{D}\left(\frac{x}{2t} + \frac{D}{4}\right)^3 \tag{4.17}$$

where D is the detonation velocity, ρ_0 is the initial density of the explosive, t is the current time and $t = 0$ corresponds to the initiation of the detonation. In this work $D = 6930$ m/s and $\rho_0 = 1630$ kg/m^3. The pressure profile is calculated through (4.17) assuming that the detonation front has reached the end of the explosive. The temperature is then calculated through the equation of state (EOS) of the explosives. In the current work we simply use the ideal gas EOS given by

$$P = (\gamma - 1)\rho C_v T \tag{4.18}$$

where C_v is the specific heat coefficient at constant pressure, γ is the ratio of the specific heats and T is the temperature.We set $C_v = 143.3$ J/kgK and $\gamma = 3$ according to [99].

4.3 Modeling of a concrete slab subjected to explosive loading

The example presented here is similar to the one found in [100]. A concrete slab is loaded with a plane wave generator which consists of an inner cone of TNT and an outer cone of Composition B. The slab has a thickness of 0.32 m and an area of 1.2 m ×1.2 m and is discretized with ∼ 1900000 particles. The explosive cone has a diameter of 0.103 m, a height of 0.075 m, and is discretized with ∼ 100000 particles. Both the slab and the explosives are immersed into a background mesh with dimensions 1.8 m × 1.8 m × 1.8 m, that is discretized with 3375000 isogeometric elements. The compressive strength of the concrete is 48 MPa and the rest of the parameters can be found in [100]. The initial

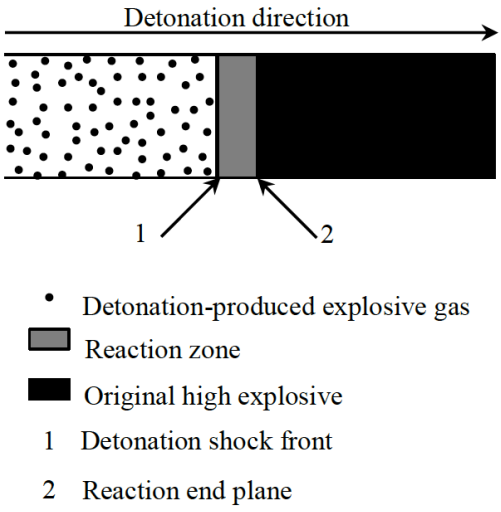

Figure 4.2: High explosive detonation zones [98]

pressure and temperature distributions are calculated from (4.17) and (4.18) and are applied as initial conditions along the height of the explosive cone assuming uniform distribution in the radial direction. Up to the point of computed results, there is qualitative agreement between the current computation and the one in [100] (this is still ongoing work), as can be seen in Figures 4.3,4.4,4.5. Figure 4.3 shows the full concrete specimen, while Figures 4.4 and 4.5 show the specimen with successive cuts along its length, to clearly show the damage evolution. Furthermore, as pointed out in [100], due to the large scatter in the experimental data, only qualitative predictions can be made for the problem under consideration. It should also be pointed out that the damage on the slab exhibits some checkerboard pattern. This is a well known phenomenon in computational mechanics and is associated with local damage models and strain localization. In the following chapters we propose a method to introduce a degree of non-locality to our formulation and improve the well-posedness of the problem.

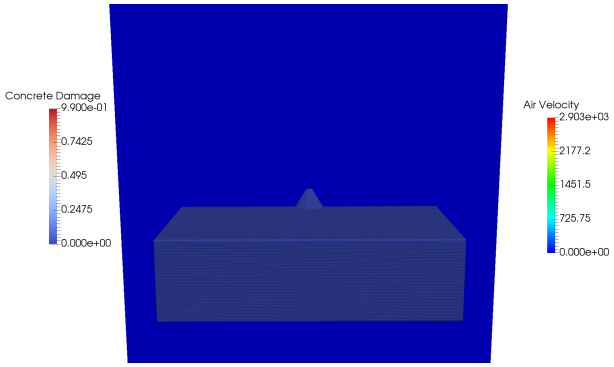

(a)

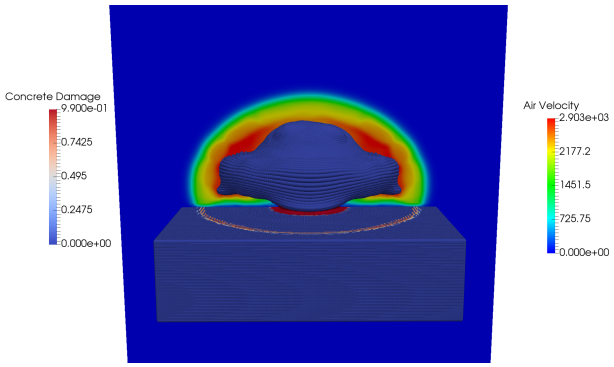

(b)

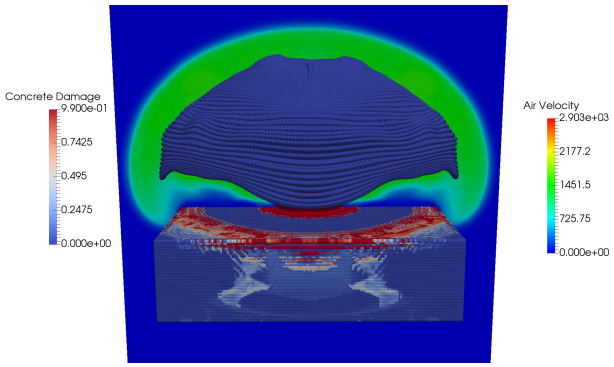

(c)

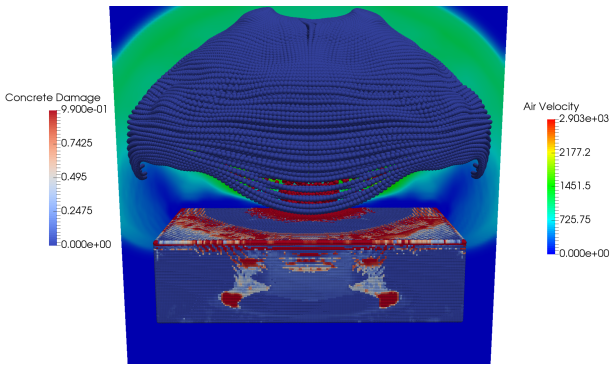

(d)

Figure 4.3: Concrete slab subjected to explosive loading. Evolution of damage. Full specimen.

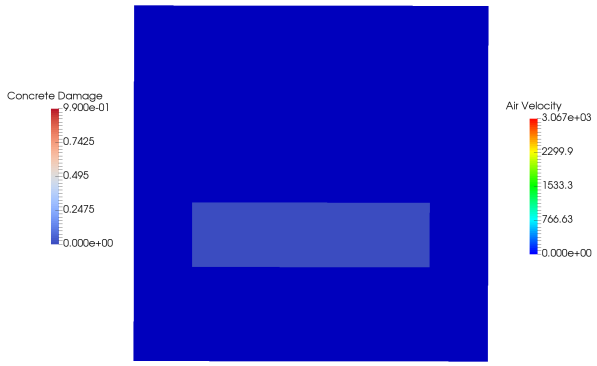

(a)

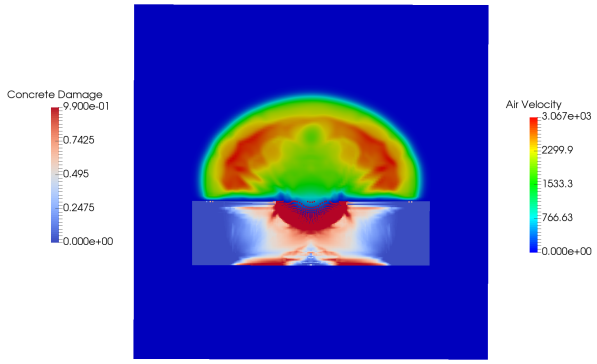

(b)

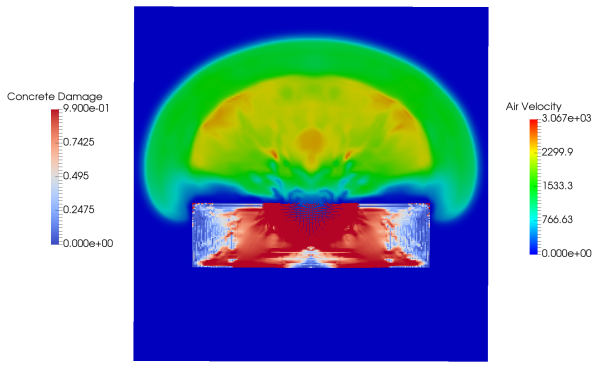

(c)

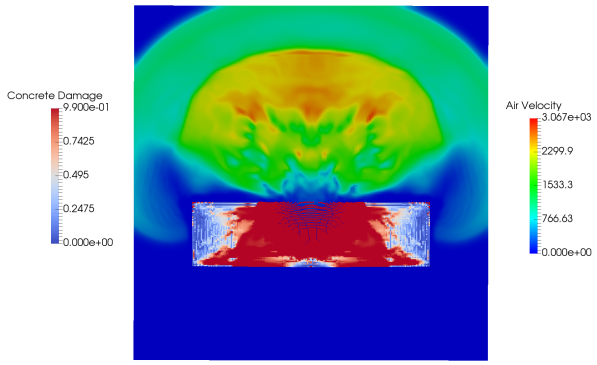

(d)

Figure 4.4: Concrete slab subjected to explosive loading. Evolution of damage. Cut at half length of specimen.

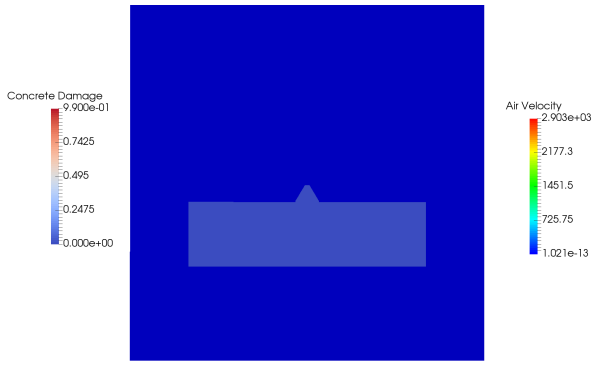

(a)

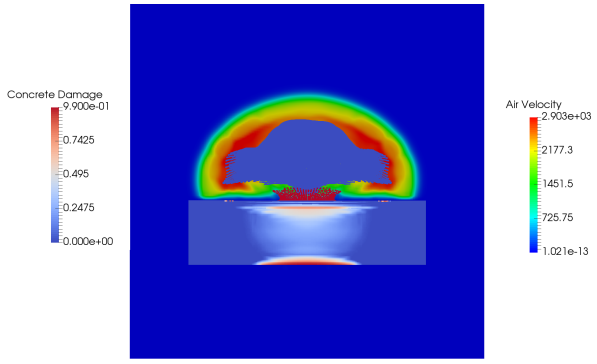

(b)

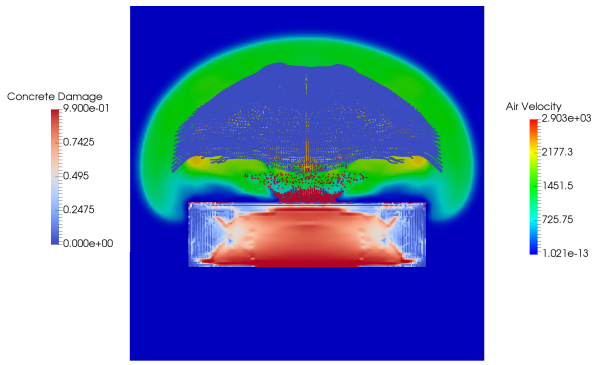

(c)

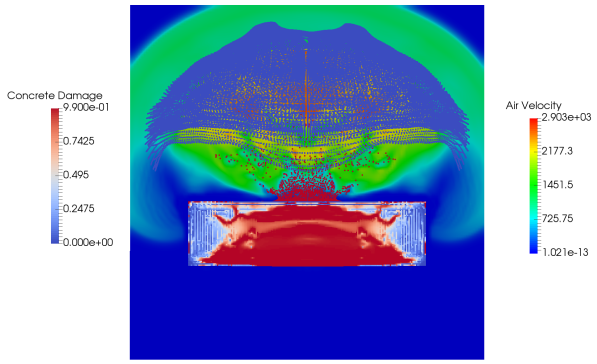

(d)

Figure 4.5: Concrete slab subjected to explosive loading. Evolution of damage. Cut and quarter length of specimen.

Chapter 5

Hyperbolic Phase Field Modeling of Brittle Fracture: main theory

In this chapter, we begin a discussion on treating the shortcomings of the local damage model presented in the previous chapter, by introducing a newly developed non-local damage model based on a phase-field approach.

Phase field models for brittle fracture (reviewed in [101]) have recently become popular, in academic circles, for finite element and isogeometric simulations of solid mechanics. Phase field models represent material integrity on a continuous scale from zero (the fully damaged phase) to one (the fully intact phase). The phase field of material integrity over a body is governed by a partial differential equation, which introduces a degree of nonlocality: the damage state at one point depends (through derivative information) on the states of neighboring points. This improves well-posedness relative to local damage models, in which history information at each point of the body determines the level of damage at that point. The use of a well-posed mathematical model ensures that sequences of discrete approximations converge to a definite limit. Finite element discretizations of local damage models typically fail to exhibit mesh independence. Local models can be partly salvaged by tuning *ad hoc* mechanisms, though, and remain widely implemented in commercial finite element packages.

A criticism frequently leveled at phase field models is that they are more computationally expensive than local damage models. In phase field models, an elliptic partial differential equation (PDE) must be solved for the damage parameter at every time step of a simulation. This adds computational cost, and makes such models incompatible with the lumped-mass explicit dynamics frameworks frequently used to efficiently simulate extreme events involving material rupture. Similar considerations apply to gradient-enhanced damage models [102], which, mathematically, are close cousins of phase field fracture models [103].

While some phase field models include time dependence (e.g., [104]), it typically results in a parabolic

PDE governing the phase field. Such PDEs cannot be efficiently discretized using explicit time integration. Explicit discretizations would be subject to Courant–Friedrichs–Lewy (CFL) stability restrictions [105] of the form

$$\Delta t \lesssim \Delta x^2 \,, \tag{5.1}$$

where Δt and Δx are time and length scales associated with the discretization. Adhering to such requirements becomes essentially intractable for large-scale computations in the limit of $\Delta x \to 0$. Other factors may hide this behavior in pre-asymptotic regimes; Ziaei-Rad and Shen [106] report acceptable performance results while using explicit time integration of a parabolic phase field model [106, Appendix B]. However, their critical time step analysis [106, Section 3.3] indicates that a CFL condition of the form (5.1) should dominate time step selection after sufficient refinement in space. Fully-resolving smoothed cracks in space may be necessary for direct numerical simulation of spatially-complex fracture dynamics, like microbranching instabilities [107]. If we could enforce some speed limit on the propagation of nonlocal damage effects, we could expect the usual hyperbolic stability condition of

$$c\Delta t \lesssim \Delta x \,, \tag{5.2}$$

where c is the wave speed. If we could model nonlocal damage effects using a hyperbolic equation, with a speed limit of the same order as (or slower than) the acoustic wave speed in the solid under consideration, then we could make highly-resolved phase field modeling more accessible in fully explicit computations.

Elliptic and parabolic phase field models may also be considered objectionable on the grounds that it is unphysical to have instant nonlocal communication in a material. For most purposes, it should suffice to consider the material's pressure wave speed (and, in classical linear elastic fracture mechanics, the slower Rayleigh wave speed) to be an upper bound on the rate of crack propagation. While it is now widely believed that supersonic fracture is possible, this phenomenon is exotic enough to have remained controversial for the entire 20$^{\text{th}}$ century [108], and it relies on physical mechanisms outside the scope of most, if not all, continuum damage and phase field fracture models, including those with instant nonlocal communication. The prevailing theoretical explanation for supersonic fracture is that a nonlinear hyperelastic material law locally increases the sound speed near crack tips [109].

Here we derive a hyperbolic phase field model for brittle fracture, by extending the microforce balance theory of Borden et al. [110, Section 2.3] to include microscopic inertia. We provide guidelines for the choice of parameters, based on an analogy to the conditions under which the related telegrapher's equation satisfies a maximum principle; this allays concerns that "wave-like" nonlocal damage models might lead to unphysical rippling of damage across an object, or the emergence of negative damage states with unclear physical interpretations.

5.1 As an extension of existing models

In this section, we propose a hyperbolic extension of an existing parabolic phase field model, based on heuristic reasoning. We will show how to derive this extension from more basic ideas in Section 5.2. However we first proceed with the present, less-principled approach, to provide the reader with a general overview of our idea, and to expose some of the issues that come up. Our point of departure is the model proposed by Kuhn and Müller [104], in which the damage parameter evolves according the the following equation of motion:

$$\frac{1}{M}\dot{s} + 2sW(\boldsymbol{\epsilon}) - G_c\left(2\varepsilon\Delta s + \frac{1-s}{2\varepsilon}\right) = 0\,, \tag{5.3}$$

where s is the phase field damage parameter, $\boldsymbol{\epsilon}$ is the linearized engineering strain, W is the un-damaged strain energy functional, G_c is the fracture energy (from Griffith's theory [111]), i.e., the amount of energy required to open a unit area of crack surface (in the quasi-static limit), and ε is a length scale over which cracks are smoothed. M is a parameter controlling the rate at which local damage information diffuses into the bulk material. Standard quasi-static phase field fracture models (e.g., [112]) that regularize Griffith's criterion (and their straightforward generalizations to dynamic fracture, e.g., [110]) correspond to the limit $M \to \infty$. The Kuhn–Müller model (5.3) serves to bridge the gap between these quasi-static models and the earlier dynamic phase-transition models of crack growth that originated in physics, based on an analogy to the Ginzburg–Landau theory of phase transitions in superconductors [113, 114]. See [101] for a more comprehensive review of the history of phase field fracture models.

A difficulty with the model (5.3) is that the phase field is governed by a parabolic heat-equation-like PDE with an unfavorable CFL condition and physically-unrealistic instantaneous communication. Noting that (5.3) is similar to the heat equation, we extend it by analogy to the so-called "telegrapher's equation", which is sometimes used to model heat conduction with a finite speed limit. In particular, we propose to add a second-order time derivative:

$$\frac{1}{M}\dot{s} + \frac{2G_c\varepsilon}{c^2}\ddot{s} + 2sW(\boldsymbol{\epsilon}) - G_c\left(2\varepsilon\Delta s + \frac{1-s}{2\varepsilon}\right) = 0\,, \tag{5.4}$$

where c is a speed limit on the propagation of the phase field through the undamaged material. We propose to set c to the speed of pressure waves, as this is the maximum speed at which information can be transmitted through the material. For an isotropic linear elastic material with shear modulus G, bulk modulus K, and mass density ρ,

$$c = \sqrt{\frac{K + \frac{4}{3}G}{\rho}}\,. \tag{5.5}$$

A possible cause for concern is that s will evolve in a wave-like manner if M is too large. Conceptually, we want s to be governed by "diffusion with a speed limit", not "wave propagation with some damping". M should be sufficiently small

to ensure that the system is "overdamped", in the sense that, if the damage parameter is initially positive, it can never become negative. Proceeding heuristicially, we can estimate the necessary upper bound on M by thinking about the damped harmonic oscillator

$$\frac{1}{M}\dot{x} + \frac{2G_c\varepsilon}{c^2}\ddot{x} = -\left(2W(\boldsymbol{\epsilon}) + \frac{G_c}{2\varepsilon}\right)x + (\text{external forces}) \tag{5.6}$$

and requiring that it be overdamped. Thus one might suppose that a sufficient condition for s to maintain a maximum property would be

$$\frac{(2\zeta\omega_0)^2}{4\omega_0^2} > 1 \,, \tag{5.7}$$

where

$$\omega_0^2 = \frac{c^2}{G_c\varepsilon}W(\boldsymbol{\epsilon}) + \frac{c^2}{4\varepsilon^2} \tag{5.8}$$

and

$$2\zeta\omega_0 = \frac{c^2}{2MG_c\varepsilon} \,, \tag{5.9}$$

in which ω_0 is the undamped resonant frequency and ζ is the canonical damping ratio. Substituting definitions and simplifying, this imposes the upper bound

$$M < \frac{c}{2\sqrt{4G_c\varepsilon W(\boldsymbol{\epsilon}) + G_c^2}} \,. \tag{5.10}$$

Remarkably, a more rigorous analysis of maximum principles for the telegrapher's equation also supports this bound, under periodicity assumptions in space and time. In summary, Ortega and Robles-Pérez [115] analyze equations of the form

$$\ddot{s} - s'' + C\dot{s} - \lambda s = f \,, \tag{5.11}$$

and conclude that there exists some ν such that, if $f \geq 0$, then $s \geq 0$, as long as $0 < -\lambda \leq \nu$. They show that ν is bounded above and below like

$$\frac{C^2}{4} < \nu \leq \frac{C^2}{4} + \frac{1}{4} \,. \tag{5.12}$$

Thus we can ensure $s \geq 0$ by enforcing $-\lambda < C^2/4$. For our problem, the analogous equation to (5.11) is

$$\ddot{s} - c^2 s'' + \frac{c^2}{2G_c\varepsilon M}\dot{s} + \left(\frac{c^2 W(\boldsymbol{\epsilon})}{G_c\varepsilon} + \frac{c^2}{4\varepsilon^2}\right)s = \frac{G_c}{2\varepsilon} \,. \tag{5.13}$$

Because the dimensions of coefficients for $\dot{s}$ and s (i.e. our "C" and "$-\lambda$") are $1/\text{time}$ and $1/(\text{time})^2$, we can re-scale the length units to make the coefficient of the s'' term equal to unity without affecting the condition $-\lambda < C^2/4$. Making the

necessary substitutions, one obtains exactly the condition (5.10), which was derived from more heuristic considerations.

Remark 1. An alternative approach to avoiding a negative phase field might be to simply include an inequality constraint that $s \geq 0$, which would allow M to be selected independently. However, this would complicate the mathematical structure of the problem and introduce difficulties in the discretized setting, so, in the present work, we have not pursued the constraint-based approach to phase field non-negativity.

5.2 Derivation from microforce balance

To arrive at a suitable model for large-displacement analysis, we now approach the problem more systematically, from the standpoint of nonlinear continuum mechanics and Gurtin's concept of "microforce balance" [116]. Microforce is a rather abstract concept but can be thought of as an auxiliary scalar field, π, that does work needed to rearrange the microscopic configuration of matter in a system. This microscopic configuration is characterized at each point by the phase field s, and $\pi\dot{s}$ is the rate of work done per unit volume, at the microscopic level, as s changes. In other words, $\dot{s}$ is rate-of-work conjugate to the microforce density. This is analogous to how $\mathbf{f} \cdot \dot{\mathbf{x}}$ is the rate of work done by an ordinary force $\mathbf{f}$ acting on a particle with position $\mathbf{x}$.

The derivation of standard phase-field fracture models from microforce balance in [117, Section 2.3] does not accommodate phase field evolution equations of the form (5.4). However, if we include an extra "microscopic inertia" term in the balance equations, the second time derivative emerges naturally. A similar idea has been considered previously in the context of continuum damage modeling by [118], but is largely dismissed therein as a mathematical curiosity, citing practical concerns of wave-like damage propagation [118, Remark 1 in Section 3.3]. These concerns are rendered unnecessary by enforcing a lower bound on the damping coefficient to ensure positivity of the phase field, as explained in Section 5.1. The role of microscale inertia in void growth has been investigated in detail by Ortiz and Molinari [119]. However, in the present work, we do not attempt to motivate the inclusion of microscopic inertia by appealing to any particular physical process; it is simply a phenomenological device introduced to limit the speed at which non-local damage effects propagate.

We now derive our phase field equation of motion from microforce balance, borrowing heavily from [117]. For simplicity, we assume an isothermal setting. The usual laws of linear and angular momentum balance apply; in a concise differential form, in the Lagrangian description, these are

$$\nabla \cdot (\mathbf{F}\mathbf{S}) + \mathbf{B} = \rho_0 \ddot{\mathbf{U}} \qquad , \qquad \mathbf{S} = \mathbf{S}^T \, , \tag{5.14}$$

where $\mathbf{U}$ is the displacement, $\mathbf{F} = \mathbf{I} + \nabla\mathbf{U}$ is the deformation gradient, $\mathbf{S}$ is the second Piola–Kirchhoff stress, and $\mathbf{B}$ is a body force density. All spatial derivatives are understood to be taken with respect to Cartesian coordinates of the

reference configuration. To incorporate damage, we supplement these standard laws with a *microforce balance law*. In integral form, the conservation law for the scalar microforce density π on some arbitrary material region Ω_0 of a solid continuum is

$$\int_{\partial\Omega_0} \boldsymbol{\xi}\cdot\mathbf{N}\, d\Gamma + \int_{\Omega_0} l\, d\Omega + \int_{\Omega_0} \pi\, d\Omega = \frac{D}{Dt}\int_{\Omega_0} \rho_s \dot{s}\, d\Omega_0 \,, \tag{5.15}$$

where $\boldsymbol{\xi}$ is a microforce flux vector, $\mathbf{N}$ is the normal to $\partial\Omega_0$, and l is a volumetric microforce source term. For simplicity, the physical parameter $\rho_s > 0$ is assumed to be constant. The corresponding differential form of this modified balance law is

$$\nabla\cdot\boldsymbol{\xi} + \pi + l = \rho_s \ddot{s} \,. \tag{5.16}$$

The additional term in this balance law implies that ongoing damage has some tendency to continue its progression. This is not altogether implausible; one might expect widening micro-cracks to continue widening in the absence of external forces, due simply to the inertia of the surrounding material. With the modified microforce balance law, energy balance is

$$\begin{aligned}&\frac{D}{Dt}\int_{\Omega_0}\left(\frac{1}{2}\rho_0|\dot{\mathbf{U}}|^2 + \frac{1}{2}\rho_s\dot{s}^2 + \rho_0 e\right) d\Omega \\ &\quad= \int_{\partial\Omega_0} (\mathbf{FSN})\cdot\dot{\mathbf{U}}\, d\Gamma + \int_{\Omega_0} \mathbf{B}\cdot\dot{\mathbf{U}}\, d\Omega + \int_{\partial\Omega_0} (\boldsymbol{\xi}\cdot\mathbf{N})\,\dot{s}\, d\Gamma + \int_{\Omega_0} l\dot{s} \,,\end{aligned} \tag{5.17}$$

where e is internal energy. Note the presence of an extra "microscopic kinetic energy" term. Using (5.15) and momentum balance, (5.17) implies

$$\rho_0\dot{e} = \frac{1}{2}\mathbf{S}:\dot{\mathbf{C}} + \boldsymbol{\xi}\cdot\nabla\dot{s} - \pi\dot{s} \,, \tag{5.18}$$

where $\mathbf{C} = \mathbf{F}^T\mathbf{F}$ is the right Cauchy–Green deformation tensor. The Clausius–Duhem inequality implies (under isothermal conditions) that energy change bounds the rate-of-change of Helmholtz free energy, ψ:

$$\rho_0\dot{\psi} \le \rho_0\dot{e} \,. \tag{5.19}$$

Expanding this inequality, under the assumption that ψ can depend on $\mathbf{C}$, s, and ∇s,

$$\begin{aligned}\int_{\Omega_0}\rho_0\dot{\psi}\, d\Omega &= \int_{\Omega_0}\left(\rho_0\frac{\partial\psi}{\partial\mathbf{C}}:\dot{\mathbf{C}} + \rho_0\frac{\partial\psi}{\partial s}\dot{s} + \rho_0\frac{\partial\psi}{\partial\nabla s}\cdot\nabla\dot{s}\right) d\Omega \\ &\le \int_{\Omega_0}\left(\frac{1}{2}\mathbf{S}:\dot{\mathbf{C}} + \boldsymbol{\xi}\cdot\nabla\dot{s} - \pi\dot{s}\right) d\Omega \,.\end{aligned} \tag{5.20}$$

Because this inequality must hold for arbitrary admissible histories of $\mathbf{C}$, s, ∇s, and their time derivatives, we get that

$$2\rho_0 \frac{\partial \psi}{\partial \mathbf{C}} = \mathbf{S} \,, \tag{5.21}$$

$$\rho_0 \frac{\partial \psi}{\partial \nabla s} = \boldsymbol{\xi} \,, \tag{5.22}$$

and, considering only $\dot{s} \leq 0$ admissible, i.e., forbidding crack healing,

$$\left(\pi + \rho_0 \frac{\partial \psi}{\partial s} + \lambda \right) \geq 0 \,, \tag{5.23}$$

where λ is a Lagrange multiplier for the constraint $\dot{s} \leq 0$, satisfying the dual feasibility and complementary slackness conditions,

$$\lambda \geq 0 \,, \tag{5.24}$$

$$\lambda \dot{s} = 0 \,, \tag{5.25}$$

the second of which ensures that $\lambda = 0$ whenever the phase field is decreasing. Interpreted in the context of microforces, λ is a constraint microforce, but the complementary slackness condition ensures that λ does no microscopic work, and therefore does not affect the energy balance equation stated before formulating the constraint. We may re-write the last inequality as

$$\pi + \rho_0 \frac{\partial \psi}{\partial s} + \lambda + \beta \dot{s} = 0 \,, \tag{5.26}$$

where $\beta \geq 0$ is some function of $\mathbf{C}$, s, and/or ∇s that encapsulates additional dissipative effects of damage processes. Using (5.16) to replace π in (5.26), then using (5.22) to replace $\boldsymbol{\xi}$, we get a PDE governing the time evolution of s:

$$\nabla \cdot \left(\rho_0 \frac{\partial \psi}{\partial \nabla s} \right) + l - \rho_0 \frac{\partial \psi}{\partial s} - \lambda = \rho_s \ddot{s} + \beta \dot{s} \,. \tag{5.27}$$

Following Borden [117], we assume that $l = 0$ and choose

$$\rho_0 \psi = g(s) W^+ + W^- + G_c \left(\frac{(1-s)^2}{4\varepsilon} + \varepsilon |\nabla s|^2 \right) \,, \tag{5.28}$$

where W^+ and W^- are stored energy functionals corresponding to the tensile and compressive responses of the undamaged material and $g(s)$ is the *degradation function*, which allows the phase field to damage the tensile material response. Unless stated otherwise, this work assumes that

$$g(s) = s^2 \,. \tag{5.29}$$

Note, in particular, that $g(1) = 1$ in the undamaged state, and $g(0) = 0$ in the completely damaged state. Other possible choices of degradation function are discussed in [120, Section 4.1].

Remark 2. In many other papers on phase field fracture, the degradation function $g(s)$ is replaced with

$$g_\eta(s) = (1-\eta)g(s) + \eta \qquad \text{or} \qquad g_\eta(s) = g(s) + \eta \,, \tag{5.30}$$

where $0 \le \eta \ll 1$ is a small dimensionless parameter, to provide additional residual strength in the fully damaged state. The claim is that this extra residual strength provides stability, although we have found that $\eta = 0$ is typically sufficient, and $\eta > 0$ can lead to much worse results in certain dynamic fracture problems (with or without time derivative terms in the phase field equation of motion).

5.3 A complete model with approximate irreversibility

We now spell out the details of implementing the model derived in Section 5.2, assuming an isotropic St. Venant–Kirchhoff constitutive model for the elastic regime. We relax the constraint that $\dot{s} < 0$ by using a strain history functional to approximately enforce non-healing of fractures.

5.3.1 Constitutive modeling

To derive the terms W^+ and W^- in the free energy functional (5.28), we first choose a desired constitutive model for the un-damaged material with strain energy W, then additively decompose it like

$$W = W^+ + W^- \,. \tag{5.31}$$

This decomposition is not unique; the particular choice affects how cracks nucleate and propagate. The effective damaged strain energy functional determining the stress–strain response with fixed s is then

$$\widetilde{W} = g(s)W^+ + W^- \,, \tag{5.32}$$

such that the second Piola–Kirchhoff stress is $\mathbf{S} = 2\partial\widetilde{W}/\partial\mathbf{C}$.

In this work, we take the simplest route to extending the linear-elastic framework of [110] to handle large rotations. We select the un-damaged free energy to be that of the St. Venant–Kirchhoff model:

$$W = \frac{1}{2}\lambda\,(tr\mathbf{E})^2 + \mu \mathrm{tr}\left(\mathbf{E}^2\right) \,, \tag{5.33}$$

where λ and μ are the Lamé parameters. This essentially uses the Green–Lagrange strain $\mathbf{E} = \frac{1}{2}(\mathbf{C} - \mathbf{I})$ in place of the engineering strain in the model of [110].

Remark 3. The St. Venant–Kirchhoff model has well-known shortcomings in the case of strong compression [121, Section 6.5, Exercise 4]. Borden et al. [117, Section 3.1] suggest an alternative using the Hencky strain, but report convergence difficulties. For many cases of interest, though, compressive deformations are not sufficient to induce the unstable behavior of the St. Venant–Kirchhoff model. An important caveat is that, when using this model, the strain energy must remain undamaged in compression. Some phase field fracture models, e.g. that of [122], have used the trivial "split" of $W^+ = W$, which relies on $W \to \infty$ as $\det\mathbf{F} \to 0$ and a regularized degradation function of the form discussed in Remark 2 to prevent damaged material from collapsing to zero volume under compression. The potential (5.33) does not possess the property of diverging under compression and, if its response to compression is damaged, the resulting instability may become significant.

Further pursuing the substitution of $\boldsymbol{\epsilon} \to \mathbf{E}$ throughout the formulation of [110], we assign[1]

$$W^+ = \frac{1}{2}\lambda\{\mathrm{tr}\mathbf{E}\}_+^2 + \mu\mathrm{tr}\left(\mathbf{E}^+\mathbf{E}^+\right) \tag{5.34}$$

and

$$W^- = \frac{1}{2}\lambda\{\mathrm{tr}\mathbf{E}\}_-^2 + \mu\mathrm{tr}\left(\mathbf{E}^-\mathbf{E}^-\right) , \tag{5.35}$$

where $\{\cdot\}_\pm$ selects the $\pm$ part of its argument, i.e.,

$$\{x\}_\pm = \begin{cases} x & x \in \mathbb{R}^\pm \\ 0 & \text{otherwise} \end{cases} , \tag{5.36}$$

and $\mathbf{E}^\pm$ are determined by diagonalizing $\mathbf{E}$ and isolating portions corresponding to positive and negative eigenvalues. In particular, let

$$\mathbf{E} = \mathbf{P}\boldsymbol{\Lambda}\mathbf{P}^T , \tag{5.37}$$

where $\boldsymbol{\Lambda} = \mathrm{diag}(\lambda_1, \lambda_2, \lambda_3)$ has the eigenvalues of $\mathbf{E}$ on its diagonal and $\mathbf{P}$ has the corresponding eigenvectors as its columns. Then

$$\mathbf{E}^+ = \mathbf{P}\boldsymbol{\Lambda}^+\mathbf{P}^T , \tag{5.38}$$

$$\mathbf{E}^- = \mathbf{P}\boldsymbol{\Lambda}^-\mathbf{P}^T , \tag{5.39}$$

where

$$\boldsymbol{\Lambda}^\pm = \mathrm{diag}\left(\{\lambda_1\}_\pm, \{\lambda_2\}_\pm, \{\lambda_3\}_\pm\right) . \tag{5.40}$$

[1] N.b. that $\{\mathrm{tr}\mathbf{E}\}_\pm \neq \mathrm{tr}\left(\mathbf{E}^\pm\right)$.

The second Piola–Kirchhoff stress can then be computed by differentiating $\widetilde{W}$ with respect to $\mathbf{E}$:

$$\mathbf{S} = g(s)\mathbf{S}^+ + \mathbf{S}^- \ , \tag{5.41}$$

where

$$\mathbf{S}^\pm = \frac{\partial W^\pm}{\partial \mathbf{E}} = \lambda\{\mathrm{tr}\mathbf{E}\}_\pm \mathbf{I} + 2\mu\mathbf{E}^\pm \ . \tag{5.42}$$

5.3.2 Approximate enforcement of irreversibility

To simplify the mathematical structure of the problem, we remove the Lagrange multiplier λ used to enforce the constraint $\dot{s} \le 0$ in Section 5.2. However, to have a practical model, we still need some mechanism to ensure that fractures do not heal. Following Borden [120, Section 3.6.1], we introduce a strain history functional

$$\mathcal{H}(\mathbf{X}, t) = \max_{\tau \le t} \left(W^+(\mathbf{F}(\mathbf{X}, \tau)) \right) \ , \tag{5.43}$$

to be used in place of the tensile strain energy W^+ in the phase field's governing equation. Essentially, we are making the approximation

$$\lambda \approx g'(s)\left(\mathcal{H} - W^+\right) \ . \tag{5.44}$$

While the use of a history functional may not strictly follow from the microforce derivation, it has several practical advantages in computations, as discussed by Borden in [120, Section 3.6.1]. An alternative approach is that of Wheeler et al. [123], in which the Lagrange multiplier field is computed using augmented Lagrangian iteration. In explicit computations, one might also consider simply applying the constraint explicitly at each time step, but we have not studied that alternative in detail.

5.3.3 Weak form and finite element discretization

Pulling together the ideas from previous sections, we now state the weak form of the coupled nonlinear elastic and hyperbolic phase field equations, assuming the St. Venant–Kirchhoff elasticity model and approximating irreversibility with the strain history functional. The weak problem is: Find displacement $\mathbf{y} \in \mathcal{S}_y$ and phase field $s \in \mathcal{S}_s$ such that, for all $\mathbf{w} \in \mathcal{V}_y$ and $r \in \mathcal{V}_s$,

$$\begin{aligned} &(\rho_0 \ddot{\mathbf{y}} - \mathbf{f}, \mathbf{w})_{L^2(\Omega_0)} + (\mathbf{S}, D_{\mathbf{w}}\mathbf{E})_{L^2(\Omega_0)} - (\mathbf{h}, \mathbf{w})_{L^2((\Gamma_h)_0)} \\ &\quad + \left(\left(\frac{2G_c\varepsilon}{c^2}\ddot{s} + \frac{1}{M}\dot{s} + g'(s)\mathcal{H} + \frac{G_c(s-1)}{2\varepsilon} \right), r \right)_{L^2(\Omega_0)} + (2\varepsilon G_c \nabla s, \nabla r)_{L^2(\Omega_0)} = 0 \ , \end{aligned} \tag{5.45}$$

where Ω_0 is the reference configuration of the body, ρ_0 is the mass density in the reference configuration, $\mathbf{f}$ is a body force, $\mathbf{S}$ is the second Piola–Kirchhoff stress given by (5.41),

$$D_{\mathbf{w}}\mathbf{E} = \frac{d}{d\epsilon}\mathbf{E}(\mathbf{y}+\epsilon\mathbf{w})\Big|_{\epsilon=0} , \tag{5.46}$$

$\mathbf{h}$ is a prescribed traction on the Neumann boundary $(\Gamma_h)_0 \subset \partial\Omega_0$, G_c is the fracture energy, ε is the phase field length scale parameter, and $\mathcal{H}$ is the history parameter defined in (5.43). Based on the heuristic exposition of Section 5.1, using $g(s) = s^2$, we choose the phase field speed limit parameter c according to (5.5) and M according to

$$M = C_M \frac{c}{2\sqrt{4G_c\varepsilon\mathcal{H} + G_c^2}} . \tag{5.47}$$

In principle, we should select $C_M \in (0,1)$. As a default value in computations, we use $C_M = 1$, unless otherwise specified, to avoid excessive artificial damping.[2] The question of whether or not this ensures that the phase field remains non-negative remains open, but we do not observe significant negative values of s in any of our numerical experiments (beyond levels attributable to discretization error, as seen also with models not involving $\ddot{s}$). We elaborate in the sequel how one might alternatively select c in a phenomenological way, to model empirically-observed rate toughening effects, but a careful investigation of that possibility is left for future research.

Remark 4. Note that, for different choices of degradation function, M should be selected differently. The coefficient of the reaction term (corresponding to $-\lambda$ in the model problem (5.11) of [115]) would become nonlinear in the phase field, i.e.,

$$\frac{g'(s)}{s}\mathcal{H} , \tag{5.48}$$

rather than $2\mathcal{H}$. For reasons of numerical stability, (5.48) should be simplified based on the analytical expression for $g'(s)$, to avoid dividing by s, which we expect to become very small.

The weak problem (5.45) can be stably discretized in space using the Bubnov–Galerkin approach, i.e., posing (5.45) directly on finite-dimensional subspaces of the test and trial spaces. In the present paper, we use standard Lagrange finite element spaces, to clearly separate new modeling (i.e., alteration of the PDE used for phase field fracture analysis) from new discretization techniques.

We discretize in time using the generalized-α method [63]. This is an implicit, second-order accurate time integration scheme which evaluates displacements, velocities, and accelerations at intermediate "α-levels" between time steps, based on a collection of parameters α_f, α_m, β, and γ that are uniquely-determined by a scalar $\rho_\infty \in [0,1]$. The parameter ρ_∞ is the spectral radius of the method's amplification matrix as the time step, Δt, goes to infinity. As

[2] To satisfy purists, one might formally say that $C_M = 1-\epsilon$, to agree with the non-inclusive upper bound, then take ϵ smaller than machine precision.

explained in [124], the implicit method of [63] can be extended to an explicit predictor–multi-corrector scheme by using a fixed number of Newton iterations with an approximate tangent matrix to resolve the implicit nonlinear problem, regardless of convergence.[3] We refer to [65] for a detailed account of the generalized-α method in the notation used here. The only non-standard aspect of applying this approach to the present problem is the treatment of the strain history functional, $\mathcal{H}$. The most natural approach is to evaluate $\mathcal{H}$ at the same intermediate time level as the displacement when assembling the residual of the nonlinear implicit problem:

$$\mathcal{H}^{n+\alpha_f} = \max\left\{\mathcal{H}^{\text{old}}\ ,\ (W^+)^{n+\alpha_f}\right\}\ , \tag{5.49}$$

where $(W^+)^{n+\alpha_f}$ is computed from the α_f-level structural strain state and $\mathcal{H}^{\text{old}}$ is the previous maximum value of W^+. Once the solution for the $n+1$-level displacement field $\mathbf{y}^{n+1}$ is obtained, $\mathcal{H}^{\text{old}}$ is updated to $\mathcal{H}^{\text{old}} \leftarrow \mathcal{H}^{n+\alpha_f}$.

For explicit computations using the quadratic degradation function $g(s) = s^2$, we employ the following approximate tangent form:

$$\begin{aligned} D_{\{\Delta\mathbf{y}^{n+1},\,\Delta s^{n+1}\}}&\text{Res}\,(\mathbf{y}^{n+\alpha_f}, \dot{\mathbf{y}}^{n+\alpha_f}, \ddot{\mathbf{y}}^{n+\alpha_m}, s^{n+\alpha_f}, \dot{s}^{n+\alpha_f}, \ddot{s}^{n+\alpha_m}, \mathbf{w}, r) \\ &\approx \frac{\alpha_m}{\beta\Delta t^2}\left\{\left(\rho_0\Delta\mathbf{y}^{n+1}, \mathbf{w}\right)_{L^2(\Omega_0)} + \left(\frac{2G_c\varepsilon}{c^2}\Delta s^{n+1}, r\right)_{L^2(\Omega_0)}\right\} \\ &\quad + \frac{\alpha_f\gamma}{\beta\Delta t}\left(\frac{1}{M^{n+\alpha_f}}\Delta s^{n+1}, r\right)_{L^2(\Omega_0)} + \alpha_f\left(\left(2\mathcal{H}^{n+\alpha_f} + \frac{G_c}{2\varepsilon}\right)\Delta s^{n+1}, r\right)_{L^2(\Omega_0)}\ , \end{aligned} \tag{5.50}$$

where $\text{Res}(\mathbf{y}, \dot{\mathbf{y}}, \ddot{\mathbf{y}}, s, \dot{s}, \ddot{s}, \mathbf{w}, r)$ is the residual of the weak problem (5.45) and $D_{\{\Delta\mathbf{y}^{n+1},\,\Delta s^{n+1}\}}$ indicates directional differentiation with respect to $\mathbf{y}^{n+1}$ and s^{n+1}, in the directions $\Delta\mathbf{y}^{n+1}$ and Δs^{n+1} (cf. (5.46)). (All α-level quantities can be considered to be functions of these $(n+1)$-level unknowns; see [65] for detailed formulas.) The CFL conditions emanate mainly from omitting the spatial derivative terms

$$D_{\{\Delta\mathbf{y}^{n+1},\,\Delta s^{n+1}\}}\left\{(\mathbf{S}^{n+\alpha_f}, D_{\mathbf{w}}\mathbf{E}^{n+\alpha_f})_{L^2(\Omega_0)} + (2\varepsilon G_c\nabla s^{n+\alpha_f}, \nabla r)_{L^2(\Omega_0)}\right\} \tag{5.51}$$

from the tangent form. Matrix representations of (6.27) in finite element bases have the discrete structure of mass matrices; one might expect improved computational speed (and possibly greater stability) from applying standard mass lumping techniques [126, Section 7.3.2]. However, explicitly-integrated computations in this paper leave these mass-like matrices in consistent form to isolate the effects of omitting (5.51) on the CFL stability condition.

[3] If a single corrector pass is used in structural dynamics problems and the approximate tangent is the mass matrix, optimal generalized-α parameters are provided in [125]. These differ from those derived from ρ_∞ in the implicit scheme. However, in the present work, we solve a different PDE system, use a different approximate tangent, apply multiple corrector passes, and use the parameter selection from the implicit scheme.

5.4 Conclusions

Using a hyperbolic PDE system to model dynamic brittle fracture appears to be an attractive option. Pathological wave-like damage propagation can be avoided by including an appropriately-tuned dissipation mechanism. Our proposed model admits two interpretations:

1. A further regularization of the traditional elliptic phase field model that one obtains from a Mumford–Shah style approximation of Griffith fracture. (The limit of $c \to \infty$ clearly corresponds to the elliptic model and, under additional simplifying assumptions, the limit of $\varepsilon \to 0$ in the elliptic model (Γ-)converges to Griffith fracture [127].)

2. A constitutive model, in which $\varepsilon > 0$ and $c < \infty$ might be tuned to capture macroscopic process zone size, deterministic size effect [128], and rate toughening. One might also use this rate-toughening effect with a length scale larger than the true process zone size, to model energy dissipation through small branches that cannot be practically resolved. Microbranching is discussed as a rate-toughening mechanism in [129, Section III.C].

In the present proof-of-concept study, we selected the phase field propagation speed in terms of other parameters of the problem, for convenience, and with the goal of having a similar CFL condition to elastodynamics. Such a mathematically-motivated parameter selection is more in line with the first interpretation. However, in view of the available experimental data, converged solutions resulting from this simple-minded approach are not obviously less valid than those from the elliptic model. Further work may attempt to fine-tune the selection of the phase field speed limit parameter, to model rate toughening effects.

In the next chapter, the model developed here will be implemented within the isogeometric–meshfree hybrid framework for air-blast–structure interaction analysis presented in the previous chapters.. In that setting, accuracy considerations for compressible flow and elastodynamics drive the time step down to a size for which explicit simulation using a lumped mass matrix is much more efficient than implicit time integration. By using a hyperbolic phase field model in this setting, we will be able to avoid slowing this framework down by adding a linear solve at each time step, as would be needed with an elliptic model, or extreme reduction of the time step as the spatial discretization is refined, as would be needed for explicit time integration of a parabolic model.

5.5 Acknowledgements

Chapter 5, in part, is a reprint of the material as it appears in: "Hyperbolic phase field modeling of brittle fracture: Part I—Theory and simulations" (with D. Kamensky and Y. Bazilevs), *Journal of the Mechanics and Physics of Solids*, 2018. The dissertation author was one of the primary investigators and authors of the paper.

Chapter 6

Hyperbolic Phase Field Modeling of Brittle Fracture: immersed IGA-RKPM coupling for ABSI

In this chapter we present the coupling of the ABSI formulation developed in chapters 2 and 3 with the phase-field damage model developed in chapter 5.

6.1 Mathematical modeling

This section states how we represent compressible fluid interacting with a brittle solid as a system of PDEs. To facilitate the development of variational numerical methods, we state the PDE system in a weak form. Our basic modeling assumptions are that the solid behaves as described in chapter 5, and the fluid is as modeled in [55, 124, 130], namely, a compressible flow with Newtonian viscosity, equal thermodynamic and mechanical pressures, and an ideal gas equation of state. Standard kinematic and dynamic compatibility conditions are assumed at the fluid–structure interface.

6.1.1 Weak form of the coupled FSI–phase field problem

Let $\Omega \subset \mathbb{R}^d$ denote a region of d-dimensional space occupied by compressible fluid and brittle solid. Let Ω^f and Ω^s denote the individual, time-dependent fluid and solid subdomains, such that $\overline{\Omega^f} \bigcup \overline{\Omega^s} = \overline{\Omega}$ and $\Omega^f \bigcap \Omega^s = \emptyset$. Let Ω^{so} denote the solid subdomain in the reference configuration, such that $\mathbf{x} = \phi(\mathbf{X}, t)$, where $\mathbf{x}$ is a material point Ω^s, $\mathbf{X}$ is

the corresponding material point in the reference configuration Ω^{so}, and ϕ defines the motion of the body. $\nabla_{\mathbf{x}}$ denotes differentiation with respect to coordinates of the current configuration, and $\nabla_{\mathbf{X}}$ denotes differentiation with respect to coordinates of the reference configuration.

Find a vector of Eulerian velocity, pressure, and temperature fields $\mathbf{Y} \in \mathcal{S}_y$ and a scalar phase field $s \in \mathcal{S}_s$ such that, for all test functions $\mathbf{W} \in \mathcal{V}_y$ and $r \in \mathcal{V}_s$,

$$\begin{aligned} & M^f_{\Omega^f}(\mathbf{W},\mathbf{Y}) + B^f_{\Omega^f}(\mathbf{W},\mathbf{Y}) - F^f_{\Omega^f}(\mathbf{W}) \\ + \; & M^s_{\Omega^s}(\mathbf{W},\mathbf{Y}) + B^s_{\Omega^s}(\mathbf{W},\mathbf{Y}) - F^s_{\Omega^s}(\mathbf{W}) \\ + \; & K_{\Omega^{so}}(r,s) \;=\; 0, \end{aligned} \tag{6.1}$$

where $\mathcal{S}_{(\cdot)}$ and $\mathcal{V}_{(\cdot)}$ are trial solution and test function spaces, forms superscripted f correspond to the fluid subproblem, forms superscripted s correspond to the structure subproblem, the form K defines the phase field subproblem, and subscripts on forms indicate the domain over which they are integrated. Note that functions in the spaces $\mathcal{S}_y$ and $\mathcal{V}_y$ are defined on all of Ω. The spaces $\mathcal{S}_s$ and $\mathcal{V}_s$, on the other hand, consist of functions defined on the reference solid domain, Ω^{so}. The various forms appearing in (6.1) are defined as follows:

$$M^f_\omega(\mathbf{W},\mathbf{Y}) = \int_\omega \mathbf{W} \cdot \left(\mathbf{A}^f_0 \mathbf{Y}_{,t}\right) \, d\omega, \tag{6.2}$$

$$B^f_\omega(\mathbf{W},\mathbf{Y}) = \int_\omega \mathbf{W} \cdot \left(\mathbf{A}^a_i \mathbf{Y}_{,i}\right) \, d\omega - \int_\omega \mathbf{W}_{,i} \cdot (\mathbf{F}^p_i - \mathbf{F}^d_i) \, d\omega, \tag{6.3}$$

$$F^f_\omega(\mathbf{W}) = \int_\omega \mathbf{W} \cdot \mathbf{S}^f \, d\omega + \int_{\Gamma^f_H} \mathbf{W} \cdot \mathbf{H}^f \, d\Gamma, \tag{6.4}$$

$$M^s_\omega(\mathbf{W},\mathbf{Y}) = \int_\omega \mathbf{W} \cdot \left(\mathbf{A}^s_0 \mathbf{Y}_{,t}\right) \, d\omega, \tag{6.5}$$

$$B^s_\omega(\mathbf{W},\mathbf{Y}) = \int_\omega \mathbf{W} \cdot \left(\mathbf{A}^s_i \mathbf{Y}_{,i}\right) \, d\omega + \int_\omega \mathbf{W}_{,i} \cdot \mathbf{F}^\sigma_i \, d\omega, \tag{6.6}$$

$$F^s_\omega(\mathbf{W}) = \int_\omega \mathbf{W} \cdot \mathbf{S}^s \, d\omega + \int_{\Gamma^s_H} \mathbf{W} \cdot \mathbf{H}^s \, d\Gamma, \tag{6.7}$$

$$K_\omega(r,s) = \int_\omega r \cdot \left(\frac{2G_c\varepsilon}{c^2}\ddot{s} + \frac{1}{M}\dot{s} + g'(s)\mathcal{H} + \frac{G_c(s^h - 1)}{2\varepsilon} \right) d\omega + \int_\omega (2\varepsilon G_c \nabla_{\mathbf{X}} r \cdot \nabla_{\mathbf{X}} s)\ d\omega \tag{6.8}$$

The repeated index i is implicitly summed over the range $1,\ldots,d$, and the subscript "$,i$" indicates partial differentiation of a quantity in the direction i. Γ_H^f and Γ_H^s are the subsets of the fluid- and solid-domain boundaries where natural boundary conditions are imposed, and $\mathbf{H}^f$ and $\mathbf{H}^s$ contain the prescribed values of the natural boundary conditions. The Euler Jacobians $\mathbf{A}_0^f$, $\mathbf{A}_i^\alpha$, $\mathbf{A}_0^s$, and $\mathbf{A}_i^s$, fluxes $\mathbf{F}_i^p$, $\mathbf{F}_i^d$, and $\mathbf{F}_i^\sigma$, and source terms $\mathbf{S}^f$, $\mathbf{S}^s$, $\mathbf{H}^f$, and $\mathbf{H}^s$ for the Eulerian fluid and solid subproblems are defined in [124]. G_c is the fracture energy (from Griffith's theory [111]), i.e., the amount of energy required to open a unit area of crack surface (in the quasi-static limit), ε is a length scale over which cracks are smoothed, M is a parameter controlling the rate at which local damage information diffuses into the bulk material, $\mathcal{H}$ is a strain history variable driving damage evolution, and g is the so-called degradation function, which modulates material strength. Throughout the current paper, the quadratic degradation function is used:

$$g(s) = s^2\ . \tag{6.9}$$

Further details on the selection and interpretation of phase field subproblem parameters can be found in Part I.

6.1.2 Solid constitutive modeling

The fluxes $\mathbf{F}_i^\sigma$ appearing in the solid subproblem involve the solid's Cauchy stress, $\boldsymbol{\sigma}$. This stress is determined as in chapter 5: we choose a desired hyperelastic constitutive model for the un-damaged material, with strain energy W, then additively decompose it into tensile (+) and compressive (-) parts:

$$W = W^+ + W^-\ . \tag{6.10}$$

The effective damaged strain energy functional determining the stress–strain response with fixed s is then

$$\widetilde{W} = g(s)W^+ + W^-\ . \tag{6.11}$$

In Part I, we selected the un-damaged free energy to be that of the St. Venant–Kirchhoff model, and determined the split into tensile and compressive parts based on the eigenvalues of the Green–Lagrange strain tensor. However, the St. Venant–Kirchhoff model exhibits significant instabilities in the case of strong compression [121, Section 6.5, Exercise 4]. For this reason, a neo-Hookean material model (cf. [117]) is used for the coupled air-blast–structure interaction examples presented in the current work, where strong compression induced by the blast loading is expected. For a neo-Hookean material with bulk modulus K and shear modulus μ, deformed with deformation gradient $\mathbf{F}$, W^+

and W^- are given by

$$W^+ = \begin{cases} U(J) + \overline{W}(\overline{\mathbf{b}}) & J \geq 1 \\ \overline{W}(\overline{\mathbf{b}}) & J < 1 \end{cases} \tag{6.12}$$

and

$$W^- = \begin{cases} 0 & J \geq 1 \\ U(J) & J < 1 \end{cases} \tag{6.13}$$

where

$$U(J) = \frac{1}{2}K\left(\frac{1}{2}\left(J^2 - 1\right) - \ln J\right) , \tag{6.14}$$

$$\overline{W}(\overline{\mathbf{b}}) = \frac{1}{2}\mu\left(\mathrm{tr}\overline{\mathbf{b}} - 3\right) , \tag{6.15}$$

$$J = \det\mathbf{F} , \tag{6.16}$$

$$\mathbf{b} = \mathbf{F}\mathbf{F}^T , \tag{6.17}$$

and

$$\overline{\mathbf{b}} = J^{-2/3}\mathbf{b} . \tag{6.18}$$

We can obtain the Cauchy stress as follows:

$$\boldsymbol{\sigma} = \frac{2}{J}\mathbf{b}\frac{\partial\widetilde{W}}{\partial\mathbf{b}} . \tag{6.19}$$

$$\boldsymbol{\sigma} = J^{-1}\mathbf{F}\mathbf{S}\mathbf{F}^T \tag{6.20}$$

For the given form of the strain energy, this results in the following expression:

$$\boldsymbol{\sigma} = \frac{2}{J}\mathbf{b}\begin{cases} g(s)\left(U'(J)\frac{\partial J}{\partial\mathbf{b}} + \frac{\partial\overline{W}(\overline{\mathbf{b}})}{\partial\mathbf{b}}\right) & J \geq 1 \\ U'(J)\frac{\partial J}{\partial\mathbf{b}} + g(s)\frac{\partial\overline{W}(\overline{\mathbf{b}})}{\partial\mathbf{b}} & J < 1 \end{cases} \tag{6.21}$$

The necessary derivatives can be computed as follows:

$$U'(J) = \frac{1}{2}K\left(J - J^{-1}\right) . \tag{6.22}$$

$$\frac{\partial J}{\partial\mathbf{b}} = \frac{\partial\sqrt{\det\mathbf{b}}}{\partial\mathbf{b}} = \frac{1}{2}J\mathbf{b}^{-1} . \tag{6.23}$$

$$\frac{\partial \overline{W}}{\partial \mathbf{b}} = \frac{\partial \overline{W}}{\partial \overline{\mathbf{b}}} \frac{\partial \overline{\mathbf{b}}}{\partial \mathbf{b}} = \frac{J^{-2/3}}{2} \mu \left(\mathbf{I} - \frac{1}{3} (\mathrm{tr}\mathbf{b}) \mathbf{b}^{-1} \right) . \tag{6.24}$$

Substituting these into the definition of the Cauchy stress, we get

$$\boldsymbol{\sigma} = \begin{cases} g(s) \left\{ \frac{1}{2} K \left(J - J^{-1} \right) \mathbf{I} + J^{-5/3} \mu \left(\mathbf{b} - \frac{1}{3} (\mathrm{tr}\mathbf{b}) \mathbf{I} \right) \right\} & J \geq 1 \\ \\ \frac{1}{2} K \left(J - J^{-1} \right) \mathbf{I} + g(s) \left\{ J^{-5/3} \mu \left(\mathbf{b} - \frac{1}{3} (\mathrm{tr}\mathbf{b}) \mathbf{I} \right) \right\} & J < 1 \, . \end{cases} \tag{6.25}$$

6.2 Numerical implementation

In order to obtain a numerical method, we pose the weak FSI–phase field problem over finite-dimensional subspaces $\mathcal{S}^h_{(\cdot)}$ and $\mathcal{V}^h_{(\cdot)}$ of $\mathcal{S}_{(\cdot)}$ and $\mathcal{V}_{(\cdot)}$. Pulling together the constructions from [124, 130] and chapter 5, the spatially-discretized weak form is: Find $\mathbf{Y}^h \in \mathcal{S}^h_y$ and phase field $s^h \in \mathcal{S}^h_s$ such that, for all $\mathbf{W}^h \in \mathcal{V}^h_y$ and $r^h \in \mathcal{V}^h_s$,

$$\begin{aligned} & M^f_\Omega(\mathbf{W}^h, \mathbf{Y}^h) + B^f_\Omega(\mathbf{W}^h, \mathbf{Y}^h) - F^f_\Omega(\mathbf{W}^h) + B^{st}_\Omega(\mathbf{W}^h, \mathbf{Y}^h) + B^{dc}_\Omega(\mathbf{W}^h, \mathbf{Y}^h) \\ + \; & M^s_{\Omega^s}(\mathbf{W}^h, \mathbf{Y}^h) + B^s_{\Omega^s}(\mathbf{W}^h, \mathbf{Y}^h) - F^s_{\Omega^s}(\mathbf{W}^h) \\ - \; & \left(M^f_{\Omega^s}(\mathbf{W}^h, \mathbf{Y}^h) + B^f_{\Omega^s}(\mathbf{W}^h, \mathbf{Y}^h) - F^f_{\Omega^s}(\mathbf{W}^h) + B^{st}_{\Omega^s}(\mathbf{W}^h, \mathbf{Y}^h) + B^{dc}_{\Omega^s}(\mathbf{W}^h, \mathbf{Y}^h) \right) \\ + \; & K_{\Omega^{so}}(r^h, s^h) \; = \; 0 \, . \end{aligned} \tag{6.26}$$

We emphasize several important departures from the original weak problem. Note first that the semi-discrete fluid subproblem contains additional terms superscripted *st* (for "stabilization") and *dc* (for "discontinuity capturing"). These are incorporated to enhance stability of the numerical method in the presence of advection and shocks. Precise definitions of these terms may be found in [55]. Secondly, the seemingly-redundant notation of adding, then subtracting the fluid suproblem terms on Ω^s reflects our numerical quadrature procedure: integration over Ω is approximated with a quadrature rule defined on a background mesh, while integration over Ω^s is approximated with quadrature over the foreground meshfree discretization. Integration over Ω^f is accomplished by taking the difference of these two quadrature rules.

We select isogeometric splines for the background spaces $\mathcal{S}^h_y$ and $\mathcal{V}^h_y$, and RKPM meshfree spaces for $\mathcal{S}^h_s$ and $\mathcal{V}^h_s$ in the foreground. In particular, the background spaces are chosen as equal-order non-uniform rational B-splines (NURBS), the details of which can be found in reference [40]. A brief review of this technology, with emphasis on aspects needed in the present work, can be found in [130, Section 2]. An account of the RKPM basis functions and quadrature rules used in this work can be found in [130, Section 3]. For all computations in this paper, we use C^1 quadratic B-splines for IGA. For RKPM, we use a cubic B-spline kernel with rectangular support and enforce linear reproducing conditions.

To obtain a fully-discrete problem, we discretize the semi-discrete problem (6.26) in time, using the lumped-mass explicit generalized-α predictor–multi-corrector detailed in [124, Section 3.3]. Extending this to include the phase field's dynamics, the "mass matrix" associated with that subproblem is obtained by assembling the bilinear form[1]

$$\begin{aligned}
&\alpha_m \left(\frac{2G_c\varepsilon}{c^2} \Delta \ddot{s}^{n+1}, r \right)_{L^2(\Omega^{so})} + \alpha_f \gamma \Delta t \left(\frac{1}{M^{n+\alpha_f}} \Delta \ddot{s}^{n+1}, r \right)_{L^2(\Omega^{so})} \\
&+ \alpha_f \beta \Delta t^2 \left(\left(2\mathcal{H}^{n+\alpha_f} + \frac{G_c}{2\varepsilon} \right) \Delta \ddot{s}^{n+1}, r \right)_{L^2(\Omega^{so})}
\end{aligned} \tag{6.27}$$

using nodal quadrature and row-sum mass-lumping. The form's arguments $\Delta\ddot{s}^{n+1}$ and r are trial and test functions in $\mathcal{V}_s^h$. For details concerning notation for the time integration procedure (e.g., definitions of α_f, β, γ, etc.), consult [124, Section 3.3]. The form (6.27) is consistent with the approximate tangent used for explicit finite element computations in chapter 5, but written for the acceleration-based predictor–multi-corrector of [124], as suggested by the choice of symbol for the trial function argument.

A crucial difference between the present computational framework and that of [130] is the treatment of the structure's deformation gradient, $\mathbf{F}$. The deformation gradient is needed in a number of contexts: (1) to obtain the quadrature weights for integrals over Ω^s, (2) to compute W^+, when updating $\mathcal{H}$, and (3) to compute the Cauchy stress, $\boldsymbol{\sigma}$. In [130], $\mathbf{F}$ was computed from a Lagrangian displacement field defined on the RKPM foreground discretization. This definition is obviously unsuitable for simulations involving fragmentation of the foreground structure. In the present work, the deformation gradient is treated as a history variable, stored at RKPM nodes, and is computed from the formula

$$\left. \frac{\partial \mathbf{F}}{\partial t} \right|_{\mathbf{X}} = \nabla_{\mathbf{x}} \mathbf{u}(\boldsymbol{\phi}(\mathbf{X}))\, \mathbf{F}(\mathbf{X}) \,, \tag{6.28}$$

where $\mathbf{u}$ is the Eulerian fluid–structure velocity field, whose components belong to the vector $\mathbf{Y}$ introduced earlier. In particular, we use the following finite difference approximation of (6.28):

$$\frac{\mathbf{F}_{n+1} - \mathbf{F}_n}{\Delta t} = \nabla_{\mathbf{x}} \mathbf{u}_{n+\alpha_f} \mathbf{F}_{n+\alpha_f} \qquad , \qquad \mathbf{F}_{n+\alpha_f} = \mathbf{F}_n + \alpha_f (\mathbf{F}_{n+1} - \mathbf{F}_n) \tag{6.29}$$

$$\Rightarrow \quad \mathbf{F}_{n+1} = \mathbf{F}_n + \Delta t (\nabla_{\mathbf{x}} \mathbf{u}_{n+\alpha_f} (\mathbf{F}_n + \alpha_f (\mathbf{F}_{n+1} - \mathbf{F}_n))) \tag{6.30}$$

$$\Rightarrow \quad \mathbf{F}_{n+1} = (\mathbf{I} - \alpha_f \Delta t \nabla_{\mathbf{x}} \mathbf{u}_{n+\alpha_f})^{-1} (\mathbf{F}_n + \Delta t \nabla_{\mathbf{x}} \mathbf{u}_{n+\alpha_f} (\mathbf{F}_n - \alpha_f \mathbf{F}_n)) \,. \tag{6.31}$$

This method of updating $\mathbf{F}$ appears to be very robust, even for extreme deformations of totally-damaged material. One might also consider applying ideas from semi-Lagrangian RKPM analysis [85], but this would require substantial reformulation and/or modification of the Lagrangian theory developed in Part I, so we defer exploration of that possibility to future studies.

[1] Note that this formula is specialized to our choice of degradation function, $g(s) = s^2$.

6.3 Framework verification

To verify the accuracy of the proposed IGA–RKPM discretization, we apply it to two well-known dynamic fracture problems. The problems selected illustrate a number of important fracture phenomena that have been observed in experiments. The purpose of these solid-only problems is to verify that the proposed standalone phase-field fracture formulation works. Therefore, as in [130], it is assumed that air does not play any role and is thus excluded. Fluid verification was performed in [130], and is thus not necessary here.

6.3.1 Dynamic crack branching

A plate with an initial crack is placed in tension, causing the crack to extend, then branch into two cracks. According to the immersed nature of the approach described in this paper, two geometries are discretized, for the foreground and background. To prevent communication between meshfree nodes on either side of the initial crack, the foreground solid geometry is approximated with a finite-thickness crack. For refinement level N, the foreground reference geometry is

$$\Omega_N^{so} = ((0.01L, 0.11L)\times(0.01L, 0.05L)) \setminus ((0.01L, 0.06L)\times(0.02L - W_N, 0.02L + W_N)) \,, \tag{6.32}$$

where $L = 1$ m, $W_N = W_0 \times 2^{-N}$ is half the width of crack, and W_0 is the full width of the crack at level $N = 1$. These geometries converge toward a zero-thickness crack as $N \to \infty$. The background domain Ω is taken to be

$$\Omega = ((0, 0.12L)\times(0, 0.06L)) \,. \tag{6.33}$$

The structure subproblem uses the St. Venant–Kirchhoff model presented in Part I with $E = 32\times10^9$ Pa and $\nu = 0.2$. The fracture energy is $G_c = 3$ Jm^{-2}, and the length scale is $\varepsilon = 2.5\times10^{-4}$ m.

We consider three discretizations, labeled MN, at refinement levels $N = 1, 2, 3$. M1 has 150×75 elements for the background grid and $\sim 200\times81$ particles for the foreground grid. M2 has 300×150 elements for the background and $\sim 400\times162$ particles for the foreground. M3 has 600×300 background elements and $\sim 800\times324$ foreground particles.[2] Figure 6.1 shows the background and foreground discretizations corresponding to M2. The time step used with discretization MN is $\Delta t = 5\times10^{-8}\times2^{1-N}$ s.

Figure 6.2 shows several snapshots of the phase field on M1–M3. The minor asymmetry observed, especially on M3, is explained as a physical instability in [131]. Figure 6.3 compares the speed of the cracks. We define crack speed in our phase field model of this problem to be: The rate of change with respect to time of the X_1 coordinate of the

[2] These foreground particle counts are approximate, because they do not account for removal of particles falling in the finite-size initial crack built into Ω_N^{so}. The true particle counts are slightly lower.

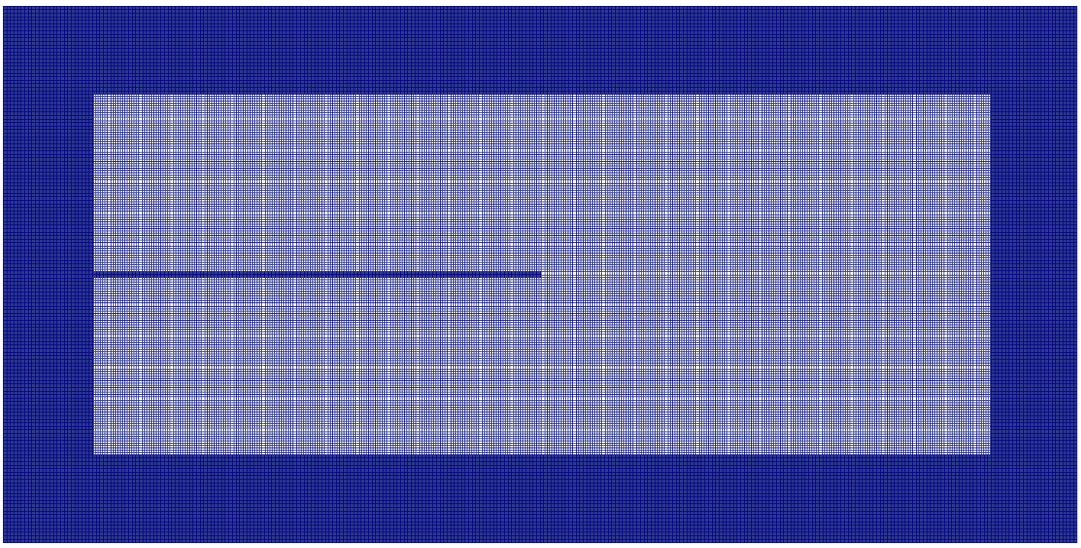

Figure 6.1: Discretization M2 used for the dynamic crack branching problem.

furthest-right point in the half-space $X_2 > 0$ of the phase field level curve at $s = 0.1$. Again, the solution on M1–M3 appears to converge towards slower crack speeds than the solutions documented by Borden et al. [110, Figure 10c]. The physical reason for this difference is discussed in [131]. For comparison purposes, the crack speed of the finest mesh (M3) of [131] is included in Figure 6.3. Overall, the results are both qualitatively and quantitatively in good agreement with the respective results of [131].

Remark 5. Very similar results can be obtained for this problem using the neo-Hookean model, but these results are omitted for the sake of brevity.

6.3.2 Shear loading

We reproduce the results of an experiment by Kalthoff and Winkler [132], in which a projectile impacts a pre-notched slab of steel, resulting in fracture of the steel slab. Only the lower-velocity impact cases of the experiment are considered, in which the steel slab failed in a brittle manner.

We model the steel slab as a St. Venant–Kirchhoff material with mass density $\rho_0 = 8000$ kg/m^3, Young's modulus $E = 190 \times 10^9$ Pa, and Poisson ratio $\nu = 0.3$. We set the fracture energy to $G_c = 2.213 \times 10^4$ J/m^2 and the phase field length scale to $\epsilon = 1.95 \times 10^{-4}$ m. Plane strain is assumed. The initial notch is again modeled with a resolution-dependent thickness, and the reference structure geometry at refinement level N is taken to be

$$\Omega_N^{so} = ((-0.05L, 0.05L) \times (-0.025L, 0.075L)) \setminus ((-0.05L, 0) \times (-W_N, +W_N)) \,, \tag{6.34}$$

M1:

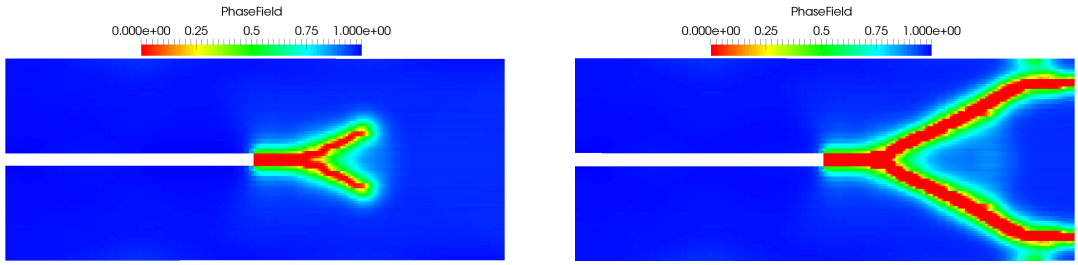

M2:

M3:

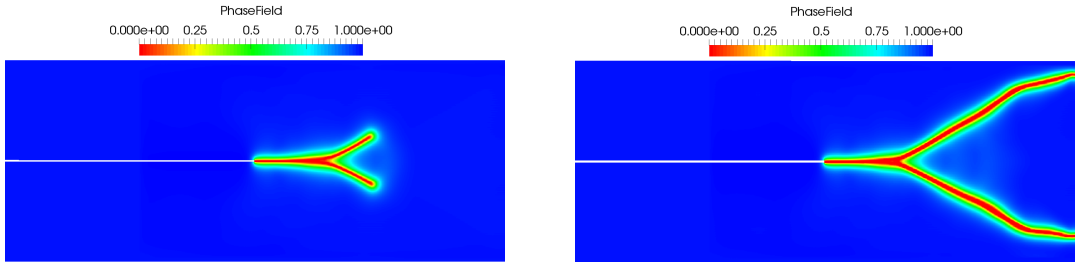

Figure 6.2: Snapshots of phase field solutions to the dynamic crack branching problem with discretizations M1–M3 at 50×10^{-6} s (left) and 90×10^{-6} s (right).

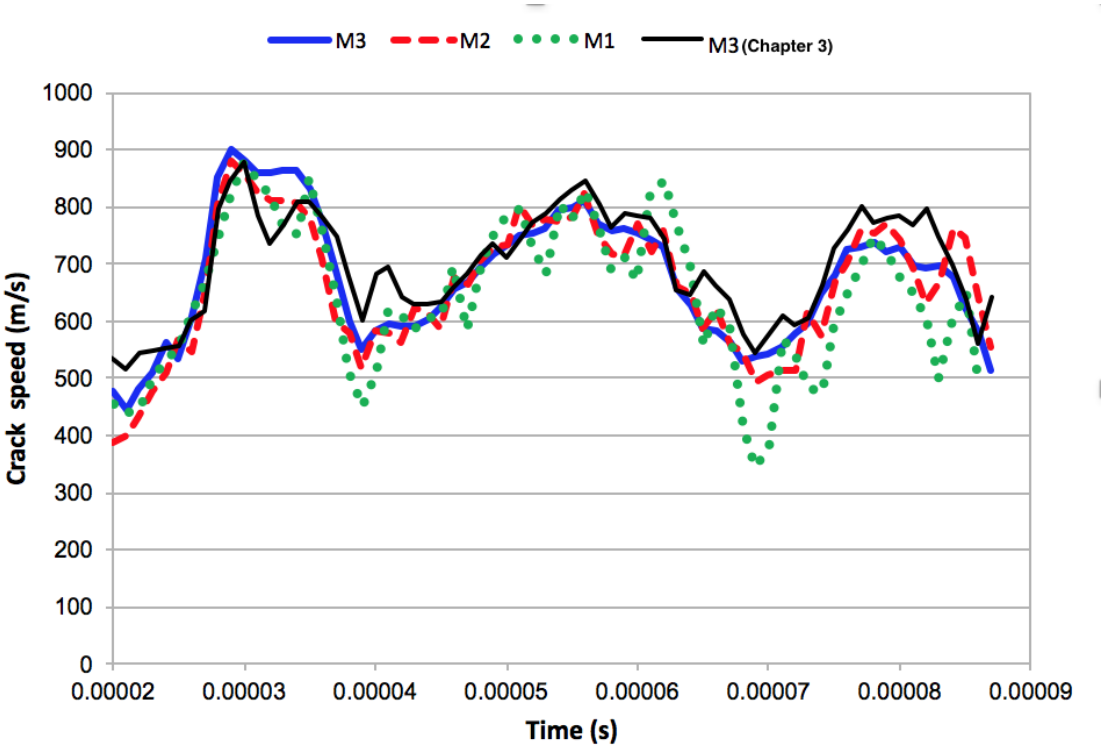

Figure 6.3: X_1-components of crack velocity over time, with discretizations M1–M3.

where $L = 1$ m, $W_N = W_0 \times 2^{-N}$ is half the width of crack at refinement level N, and W_0 is the full width of the crack at refinement level $N = 1$. The geometry of the Eulerian background domain is

$$\Omega = (-0.06L, 0.06L) \times (-0.03L, 0.08L) \, . \tag{6.35}$$

The vertical component of velocity is constrained along $x_2 = -0.025L$, and the following velocity Dirichlet condition is imposed for $x_1 \in (-0.06L, -0.045L)$, $x_2 \in (-0.03L, 0)$:

$$\mathbf{v} = \left\{ \begin{array}{ll} \dfrac{t}{T_0} v_0 & t \leq T_0 \\ v_0 & \text{otherwise} \end{array} \right\} \mathbf{e}_1 \, , \tag{6.36}$$

where $T_0 = 10^{-6}$ s and $v_0 = 16.5$ m/s. All other boundaries are traction-free.

We compute solutions to this problem on three discretizations, labeled MN, with refinement levels $N = 1, 2, 3$. M1 has 120×110 elements for the background grid and $\sim 201 \times 201$ particles for the foreground grid. M2 has 240×220 elements for the background grid and $\sim 401 \times 401$ particles for the foreground grid. M3 has 480×440 elements for the background grid and $\sim 801 \times 801$ particles for the foreground grid.[3] M2 is depicted in Figure 6.4. The time step used with MN is $\Delta t = 5 \times 10^{-8} \times 2^{1-N}$ s.

[3] As in Section 6.3.1, the initial crack is explicitly modeled in the geometry, and the true number of particles is slightly smaller.

The crack propagation in the resulting solutions matches the experimentally-observed behavior of a crack propagating at an angle of $\sim 70^\circ$ from the X_1-axis, as shown by the snapshots in Figure 6.5. The results are also in good agreement with [131] and with [110].

Remark 6. Although previous studies [133] have suggested using a mesh size smaller than half the length scale parameter, the computations of this section illustrate how this condition is not strictly necessary, especially if modeling uncertainty is substantial, and only qualitatively-accurate results are expected, as is frequently the case in simulations of extreme events.

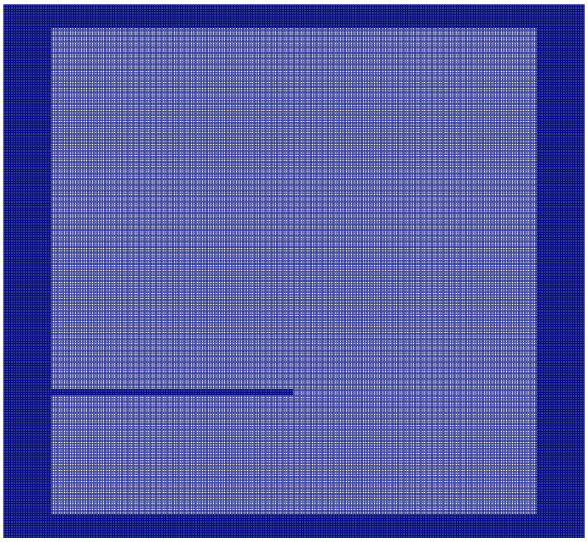

Figure 6.4: Discretization M2 used for the shear loading problem.

6.4 Blast loading and fragmentation

In this section, we apply the proposed framework to air-blast–structure interaction problems. In particular, we consider three examples that demonstrate the applicability of the model to extreme events modeling. As mentioned in Section 6.1.2, the inability of the St. Venant–Kirchoff model to withstand the high compression from blast loads leads us to use the neo-Hookean model throughout this section.

6.4.1 Detonation enclosed in hollow square block

In this example, a detonation is initiated at the center of a hollow square block. Taking into account the doubly symmetric nature of the problem data, only one quarter of the problem is computed. The foreground reference geometry is considered to be

$$\Omega^{so} = ((0, 0.3L) \times (0.3L, 0.4L)) \cup ((0.3L, 0.4L) \times (0, 0.4L)) \tag{6.37}$$

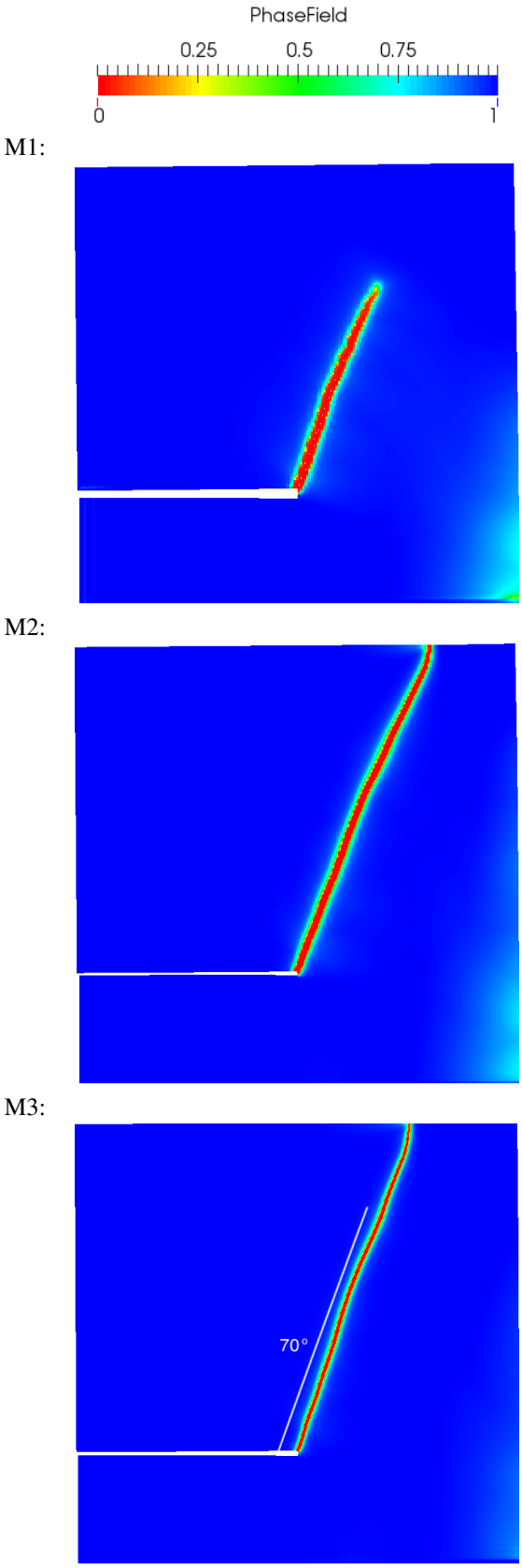

Figure 6.5: Snapshots of phase field solutions to the shear loading problem on M1–M3 at time 88×10^{-6} s.

and the Eulerian domain is set to

$$\Omega = (0, 1.0L) \times (0, 1.0L) \,, \tag{6.38}$$

where $L = 1$ m. We model the solid as having a mass density $\rho_0 = 8000$ kg/m^3, Young's modulus $E = 190 \times 10^9$ Pa, and Poisson ratio $\nu = 0.3$. We set the fracture energy to $G_c = 6.0 \times 10^5$ J/m^2 and the phase field length scale to $\epsilon = 2.5 \times 10^{-3}$ m. Plane strain is assumed.

The air in the computational domain is initially at rest, with temperature $T = 270$ K and pressure $p = 10000$ Pa. The detonation is initiated by setting higher-than-ambient values of pressure, $p = 6746268.65$ Pa, and temperature, $T = 1465$ K, in a quarter-circular region centered at the origin of the computational domain, with radius 0.15 m. Symmetry boundary conditions are applied along the lines of symmetry, and open boundaries are specified elsewhere.

We compute solutions to this problem on three discretizations, labeled M1, M2, and M3. M1 has 10000 elements for the background grid and 6600 particles for the foreground grid. M2 has 40000 elements for the background grid and 26000 particles for the foreground grid. M3 has 160000 elements for the background grid and 103200 particles for the foreground grid. The time step used with MN is $\Delta t = 4 \times 10^{-7} \times 2^{1-N}$ s. M1 is shown in Figure 6.6.

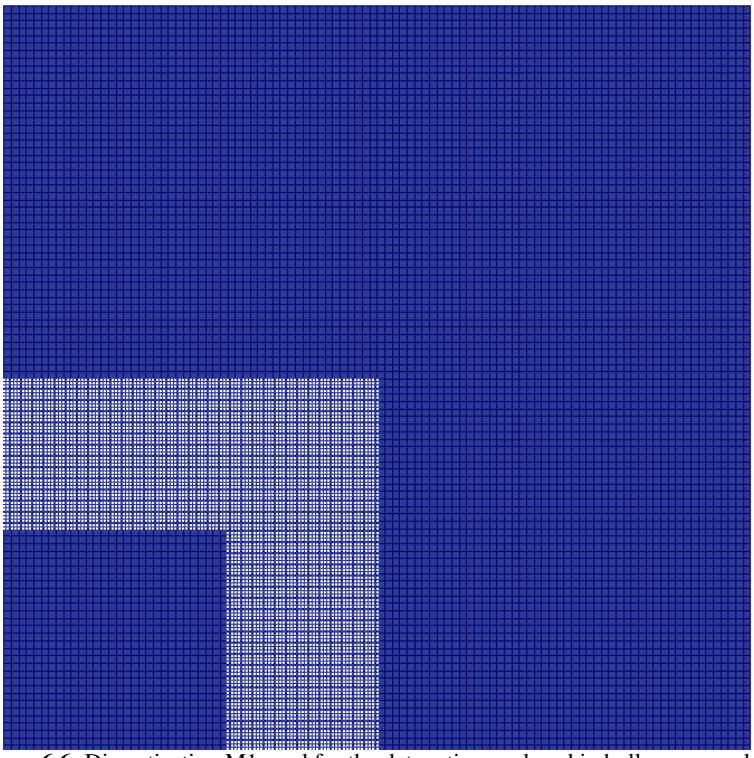

Figure 6.6: Discretization M1 used for the detonation enclosed in hollow square box.

The results for the three meshes are shown in Figures 6.7, 6.8, and 6.9 respectively. The air-speed is depicted on the background grid while the phase field is shown on the particles. A zoomed-in view of the solution on M3 during crack propagation is provided in Figure 6.10. As expected, a crack nucleates at the stress singularity caused by the reentrant inside corner of the hollow box. The crack initially propagates diagonally, then accelerates, broadens,

and branches, much like the crack from the problem considered in Section 6.3.1. Due to the nature of the immersed framework, fully-damaged particles are able to move inside the computational domain without the severe mesh distortion that would occur in a finite element foreground discretization. Although neither experimental nor prior computational results exist for this problem, the qualitative behavior is physically-reasonable. Further, the solutions from M1–M3 appear to converge toward some fixed limit, unlike discretizations of ill-posed local damage models, which often suffer from mesh dependency.

6.4.2 Detonation enclosed in hollow cylinder

A detonation is initiated at the interior of a hollow cylinder with a variable outer radius. Taking into account the doubly symmetric nature of the geometry, only one quarter of the problem is simulated. The purpose of this qualitative example is to demonstrate that the formulation developed in this paper is capable of representing complex fragmentation due to blast loads. The Eulerian fluid–structure domain is

$$\Omega = (0, 1.0L) \times (0, 1.0L) \,, \tag{6.39}$$

where $L = 1$ m. Figure 6.11 illustrates the geometry of the solid reference domain, Ω^{so}.

We model the solid material as having mass density $\rho_0 = 8000$ kg/m^3, Young's modulus $E = 190 \times 10^9$ Pa, and Poisson ratio $\nu = 0.3$. We set the fracture energy to $G_c = 6.0 \times 10^5$ J/m^2 and the phase field length scale to $\epsilon = 6.25 \times 10^{-4}$ m. Plane strain is assumed.

The air in the computational domain is initially at rest with $T = 270$ K and $p = 10000$ Pa. The detonation is initiated by setting higher-than-ambient values of pressure, $p = 6746268.65$ Pa, and temperature, $T = 1465$ K, in a quarter-circular region centered at the origin of the computational domain, with radius 0.15 m. Symmetry boundary conditions are applied along the lines of symmetry, and open boundaries are specified elsewhere.

We discretize this problem using a background grid with 57600 elements, 45900 foreground particles, and a time step of $\Delta t = 5 \times 10^{-8}$ s. The results are shown in Figure 6.12. Air-speed is depicted on the background grid while phase field is plotted on the particles. The inside of the ring initially enters a state of uniform tension, but, as the stress crosses a critical crack nucleation threshold (determined by the fracture length scale, as analyzed in [110]), this configuration becomes unstable, and damage localizes as this instability is triggered by the non-radially-symmetric discretization. After stress waves reach the outer surface, cracks also nucleate at the reentrant corners and begin to propagate inward. Cracks propagate radially until the cylinder fragments into pieces, roughly determined by the non-uniformity of the outer radius. The immersed and meshfree nature of our discretization allows these fragments to fly apart on independent trajectories, without any problematic mesh distortion.

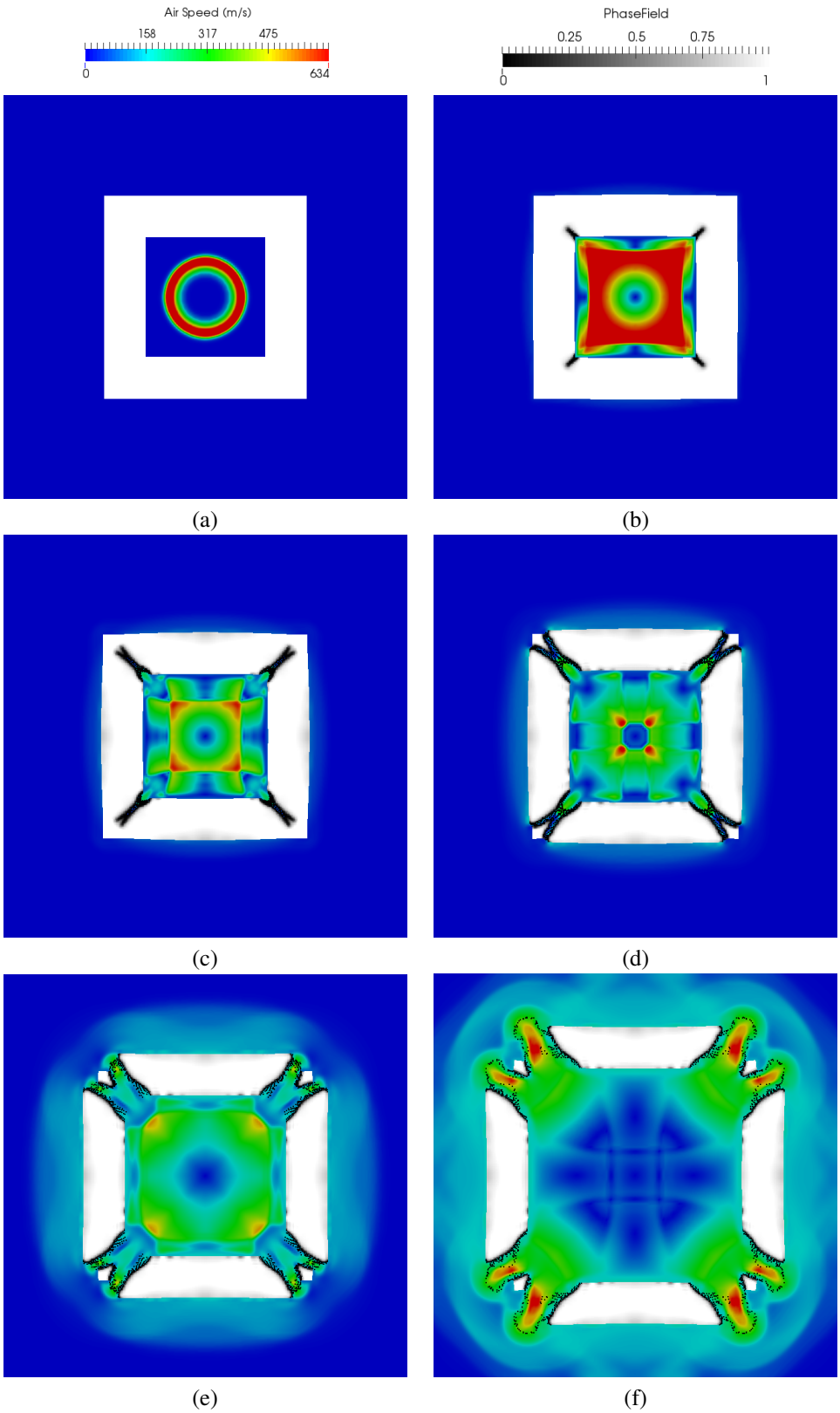

Figure 6.7: Detonation enclosed in hollow square box. Discretization M1. Air speed and phase field in the current configuration at different instants during the simulation. **a** 0.05 ms. **b** 0.325 ms. **c** 0.45 ms. **d** 0.65 ms. **e** 1.2 ms. **f** 2.0 ms.

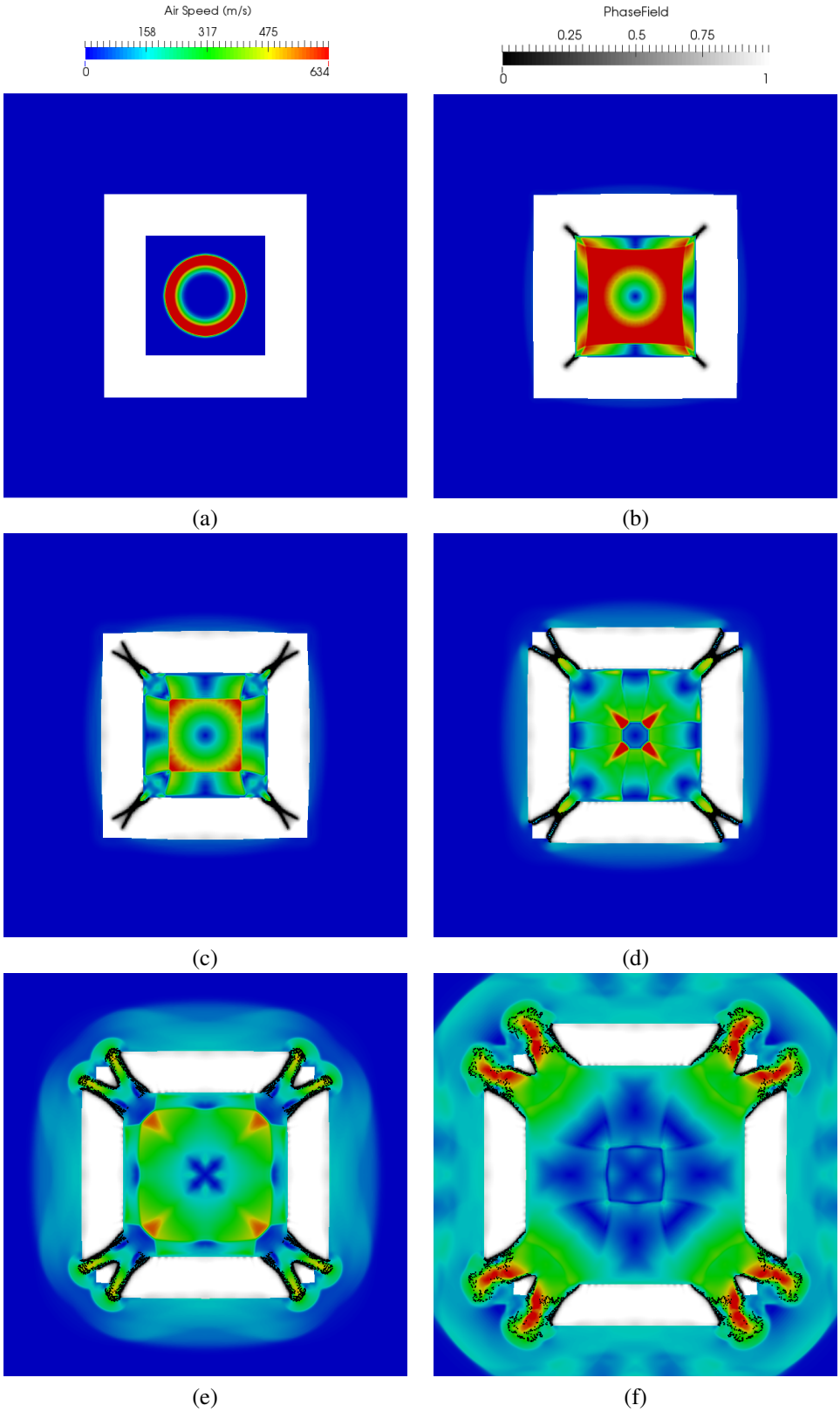

Figure 6.8: Detonation enclosed in hollow square box. Discretization M2. Air speed and phase field in the current configuration at different instants during the simulation. **a** 0.05 ms. **b** 0.325 ms. **c** 0.45 ms. **d** 0.65 ms. **e** 1.2 ms. **f** 2.0 ms.

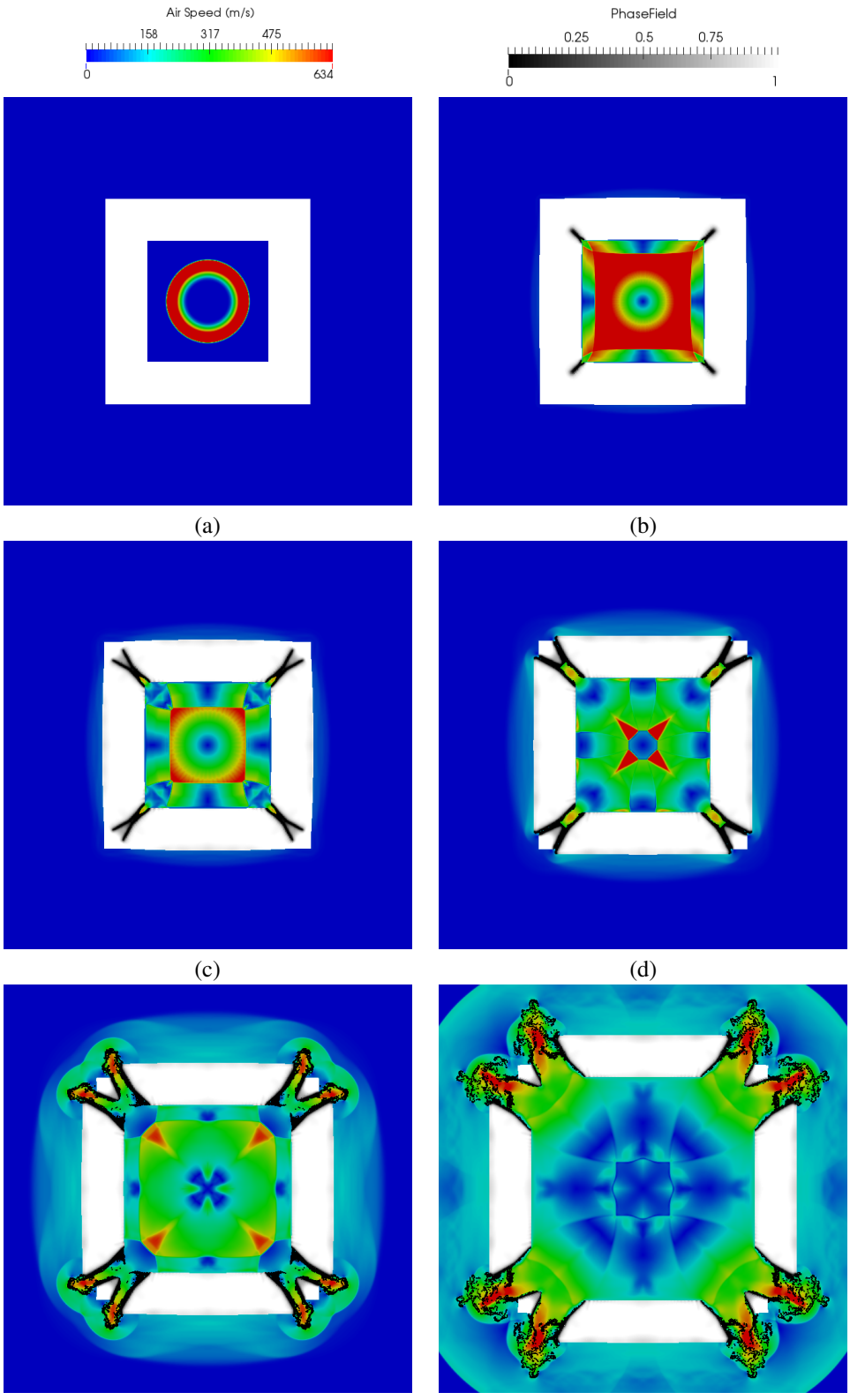

Figure 6.9: Detonation enclosed in hollow square box. Discretization M3. Air speed and phase field in the current configuration at different instants during the simulation. **a** 0.05 ms. **b** 0.325 ms. **c** 0.45 ms. **d** 0.65 ms. **e** 1.2 ms. **f** 2.0 ms.

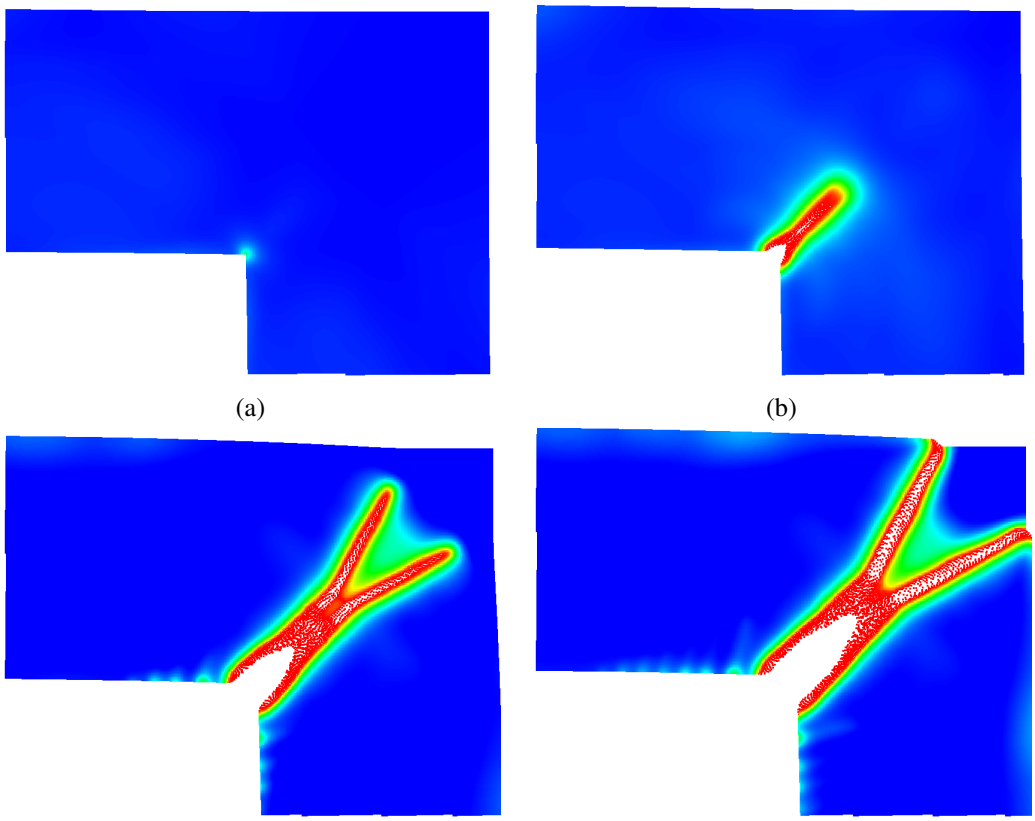

Figure 6.10: Detonation enclosed in hollow square box. Zoomed-in view of solution from M3. Phase field in the current configuration at different instants during the simulation. **a** 0.25 ms. **b** 0.325 ms. **c** 0.45 ms. **d** 0.525 ms.

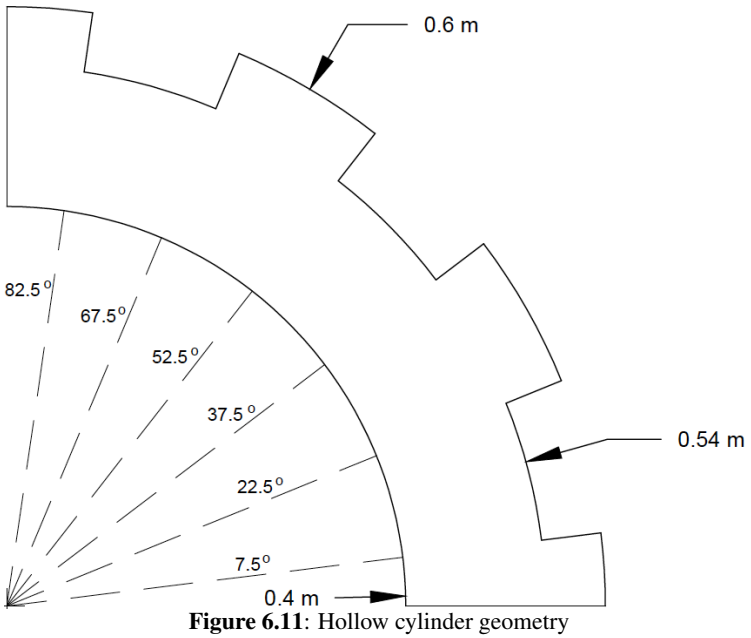

Figure 6.11: Hollow cylinder geometry

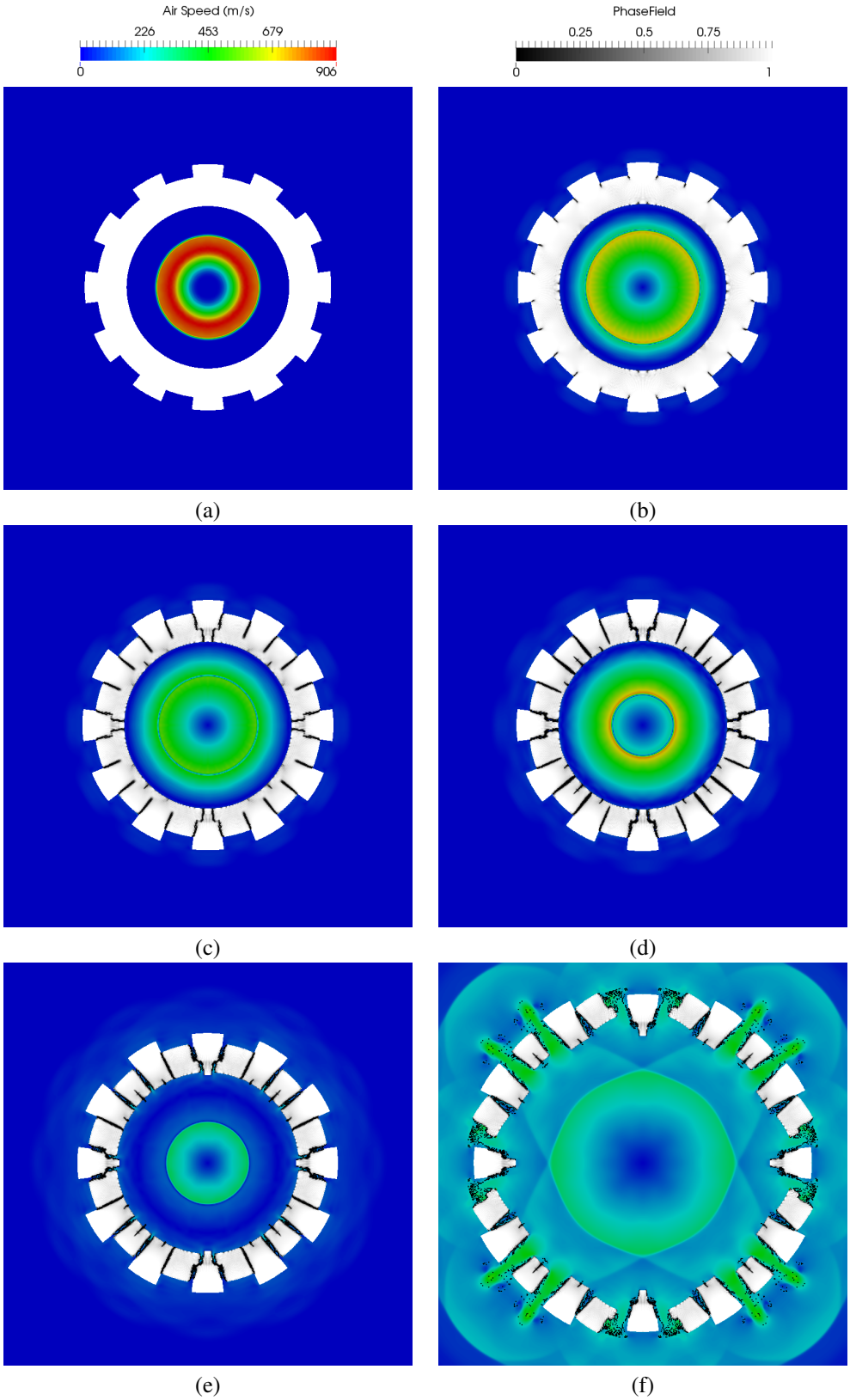

Figure 6.12: Detonation enclosed in hollow cylinder. Air speed and phase field in the current configuration at different instants during the simulation. **a** 0.05 ms. **b** 0.25 ms. **c** 0.275 ms. **d** 0.325 ms. **e** 0.5 ms. **f** 1.3 ms.

6.4.3 Blasting-induced fracture in PMMA specimens

In this example, we model the experiment reported in [134] where fracture plane control under blasting in PMMA is studied. The model consists of a charge hole (right) and a guide hole with notches (left), as shown in Figure 6.13. The foreground reference geometry is considered to be

$$\Omega^{so} = (0.01L, 0.11L) \times (0.02L, 0.22L) \tag{6.40}$$

and the Eulerian fluid–structure domain is

$$\Omega = (0, 0.11L) \times (0, 0.24L) \,, \tag{6.41}$$

where $L = 1$ m. The radius of the charge and guide hole is 0.0075 m. More details on the geometry can be found in [134].

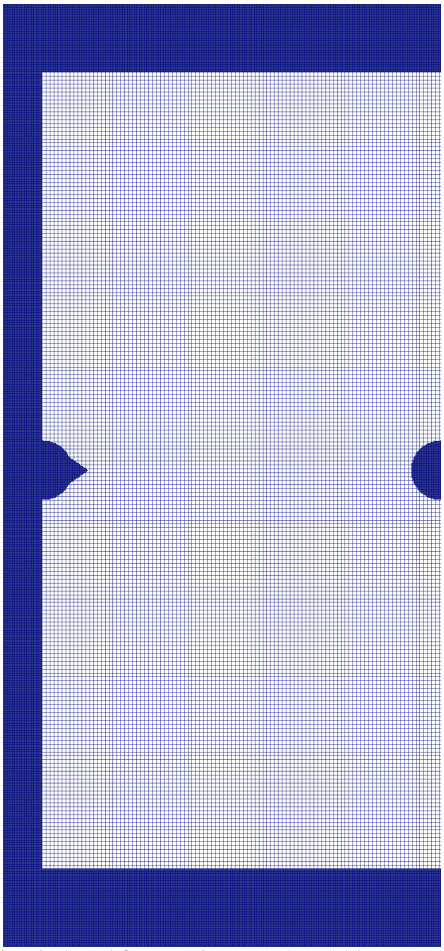

Figure 6.13: Blasting-induced fracture in PMMA. Problem setup and discretization

We model the solid material as having mass density $\rho_0 = 1188$ kg/m^3, Young's modulus $E = 5.39 \times 10^9$ Pa, and

Poisson ratio $\nu = 0.33$. We set the phase field length scale to $\epsilon = 1.0 \times 10^{-3}$ m. Plane strain is assumed. As described in [135], microscopic inhomogeneity plays a significant role in PMMA fracture propagation and fragmentation. We therefore set the fracture energy to have randomized fluctuations over the domain:

$$G_c(\mathbf{X}) = G_c^{\text{base}} + w(\mathbf{X}) \,, \tag{6.42}$$

where $G_c^{\text{base}} = 300\ \text{J/m}^2$ and $w(\mathbf{X})$ is randomly selected from a uniform distribution on the interval $(-100\,\text{J m}^{-2}, 100\,\text{J m}^{-2})$ at each point $\mathbf{X} \in \Omega^{so}$.

The air in the computational domain is initially at rest with $T = 270$ K and $p = 10^5$ Pa. The detonation is initiated by setting pressure, $p = 4.5 \times 10^5$ Pa, and temperature, $T = 450$ K, in a semi-circular region concentric to the charge hole, with radius 0.0035 m. These initial conditions attempt to mimic the PETN explosives used in [134].

A symmetry boundary condition is applied on the right face of the Eulerian domain, while traction–free boundary conditions are applied on the other faces.

We discretize the problem with 73200 elements for the background grid and 318123 particles for the foreground grid. The time step used is $\Delta t = 5 \times 10^{-8}$ s. The problem setup and discretization are shown in Figure 6.13.

The results are shown in Figure 6.14. The current computations reproduce the major qualitative features of the experiments depicted in Figure 6.14 and in [134, Figure 18]: the region immediately surrounding the charge hole is heavily damaged, with several distinct cracks emanating from it, while an additional fracture propagates in a roughly straight line from the notched guide hole toward the charge hole.

6.5 Conclusions

We presented a computational framework for simulating extreme events involving dynamic brittle fracture of materials subjected to blast loading. This novel approach combines the hyperbolic model for phase field fracture from chapter 5 with the IGA–RKPM framework for air-bast–structure interaction presented in chapters 2 and 3. In simulations of explosions, the need to resolve stress waves propagating through the material drives the time step down to a size for which explicit time integration of elastodynamics and compressible flow is much more efficient than implicit integration. The use of a hyperbolic phase field model allows us to explicitly integrate the phase field's governing PDE as well, without introducing the severe time step restrictions associated with parabolic models.

The results of fracture analyses performed using the proposed formulation match solutions calculated with standard finite element methods, as presented in [131]. Although neither experimental nor computational results exist for the first two air-blast–structure interaction problems presented in this work, the IGA–RKPM simulations reproduce phenomena expected from the underlying fluid, structure, and fracture mechanics, and exhibit qualitative convergence

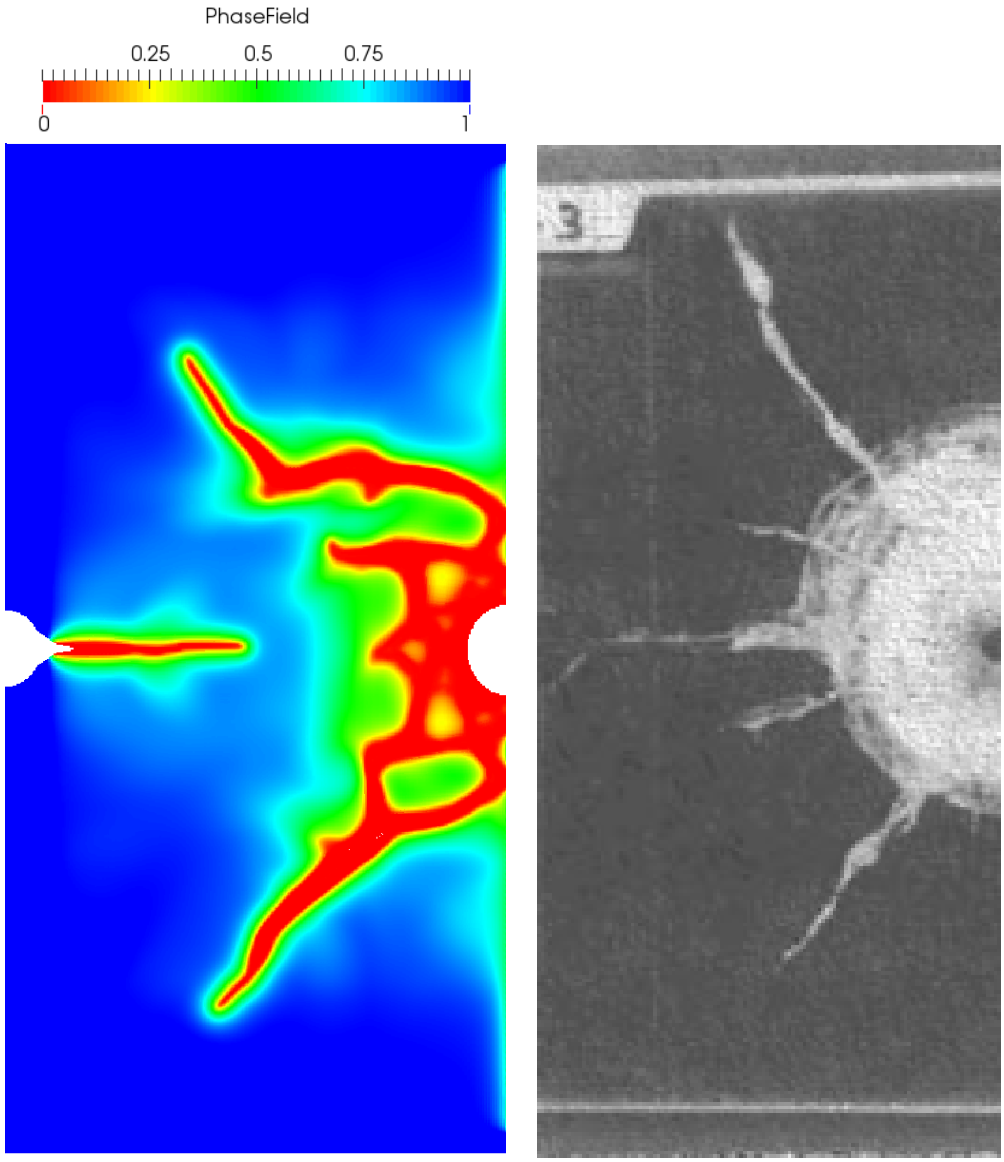

Figure 6.14: Blasting-induced fracture in PMMA. Phase field in the current configuration at the end of the computation (left), experiment from [134] (right).

toward physically-stable solution features under mesh refinement. In addition, the last air-blast–structure interaction example demonstrates qualitative agreement with the reference experimental results.

6.6 Acknowledgements

Chapter 6, in part, is a reprint of the material as it appears in: "Hyperbolic phase field modeling of brittle fracture: Part II—immersed IGA-RKPM coupling for air-blast–structure interaction" (with D. Kamensky, J.S. Chen and Y. Bazilevs), *Journal of the Mechanics and Physics of Solids*, 2018. The dissertation author was the primary investigator and author of the paper.

Chapter 7

Conclusions

In the current dissertation, a new immersed approach for air-blast–structure interaction is developed. Compressible flow in the high-Mach number regime is coupled with inelastic structures. Two discretizations are employed; a fixed background discretization that provides the discrete trial and test function spaces for the coupled FSI problem and a foreground discretization that moves with the solid material particles. The foreground discretization is used to track the current position of the structure, store history-dependent variables, and perform numerical quadrature. At first, the core formulation is presented. Then, a particular instantiation that couples isogeometric analysis with meshfree particles is developed and applied to benchmark problems and to a problem involving blasting of a concrete slab. In addition, the particles are equipped with RKPM basis functions that provide the discrete trial and test function spaces for the approximation of the hyperbolic phase field equation for brittle fracture modeling.

The formulation has the advantage over existing embedded domain methods in that a monolithic formulation is naturally obtained. Additionally, no restrictions on the solid motion are imposed, which enables handling any domain topological changes with relative ease. The higher-order accuracy and smoothness of the background discretization delivers high quality compressible flow solution with shocks and also gives a continuous representation of the strain-rate field, which greatly improves the quality of the solid mechanics solution. The non-local damage model presented in the end eliminates the shortcomings of local damage models such as loss of well-posedness, while its implementation within the ABSI framework provides a powerful tool for simulating structural disintegration and fragmentation that results from a mathematically well-posed damage evolution approach triggered by the blast loads applied on the structures. Finally, the hyperbolic nature of the damage evolution equation allows for an efficient explicit time integration that is not subjected to severe time step restrictions and is compatible with the explicit lumped-mass type approach adopted for the coupled ABSI problem.

Bibliography

[1] Cynthia Pearson and Norbert Delatte. Ronan point apartment tower collapse and its effect on building codes. *Journal of Performance of Constructed Facilities*, 19(2):172–177, 2005.

[2] W Gene Corley, Paul F Mlakar Sr, Mete A Sozen, and Charles H Thornton. The oklahoma city bombing: Summary and recommendations for multihazard mitigation. *Journal of Performance of Constructed Facilities*, 12(3):100–112, 1998.

[3] T.J.R. Hughes, W.K. Liu, and T.K. Zimmermann. Lagrangian-eulerian finite element formulation for incompressible viscous flows. *Computer methods in applied mechanics and engineering*, 29(3):329–349, 1981.

[4] W.K. Liu. Finite element procedures for fluid-structure interactions and application to liquid storage tanks. *Nuclear Engineering and Design*, 65(2):221–238, 1981.

[5] W.K. Liu, C. Herman, J.S. Chen, and T. Belytschko. Arbitrary lagrangian-eulerian petrov-galerkin finite elements for nonlinear continua. *Computer methods in applied mechanics and engineering*, 68(3):259–310, 1988.

[6] G. Hauke and T.J.R. Hughes. A comparative study of different sets of variables for solving compressible and incompressible flows. *Computer Methods in Applied Mechanics and Engineering*, 153(1):1–44, 1998.

[7] G. Hauke. Simple stabilizing matrices for the computation of compressible flows in primitive variables. *Computer methods in applied mechanics and engineering*, 190(51):6881–6893, 2001.

[8] A. N. Brooks and T. J. R. Hughes. Streamline upwind/Petrov-Galerkin formulations for convection dominated flows with particular emphasis on the incompressible Navier-Stokes equations. *Computer Methods in Applied Mechanics and Engineering*, 32:199–259, 1982.

[9] T. J. R. Hughes and T. E. Tezduyar. Finite element methods for first-order hyperbolic systems with particular emphasis on the compressible Euler equations. *Computer Methods in Applied Mechanics and Engineering*, 45:217–284, 1984.

[10] G. J. Le Beau, S. E. Ray, S. K. Aliabadi, and T. E. Tezduyar. SUPG finite element computation of compressible flows with the entropy and conservation variables formulations. *Computer Methods in Applied Mechanics and Engineering*, 104:397–422, 1993.

[11] T. E. Tezduyar and M. Senga. Stabilization and shock-capturing parameters in SUPG formulation of compressible flows. *Computer Methods in Applied Mechanics and Engineering*, 195:1621–1632, 2006.

[12] T. J. R. Hughes, G. Scovazzi, and T. E. Tezduyar. Stabilized methods for compressible flows. *Journal of Scientific Computing*, 43:343–368, 2010. DOI: 10.1007/s10915-008-9233-5.

[13] T. J. R. Hughes, M. Mallet, and A. Mizukami. A new finite element formulation for computational fluid dynamics: II. Beyond SUPG. *Computer Methods in Applied Mechanics and Engineering*, 54:341–355, 1986.

[14] T. J. R. Hughes and M. Mallet. A new finite element formulation for computational fluid dynamics: IV. A discontinuity-capturing operator for multidimensional advective-diffusive systems. *Computer Methods in Applied Mechanics and Engineering*, 58:329–339, 1986.

[15] T. E. Tezduyar, M. Senga, and D. Vicker. Computation of inviscid supersonic flows around cylinders and spheres with the SUPG formulation and YZβ shock-capturing. *Computational Mechanics*, 38:469–481, 2006.

[16] T. E. Tezduyar and M. Senga. SUPG finite element computation of inviscid supersonic flows with YZβ shock-capturing. *Computers & Fluids*, 36:147–159, 2007.

[17] F. Rispoli, R. Saavedra, A. Corsini, and T. E. Tezduyar. Computation of inviscid compressible flows with the V-SGS stabilization and YZβ shock-capturing. *International Journal for Numerical Methods in Fluids*, 54:695–706, 2007.

[18] F. Rispoli, R. Saavedra, F. Menichini, and T. E. Tezduyar. Computation of inviscid supersonic flows around cylinders and spheres with the V-SGS stabilization and YZβ shock-capturing. *Journal of Applied Mechanics*, 76:021209, 2009.

[19] R. Löhner, H. Luo, J.D. Baum, and D. Rice. Improvements in speed for explicit, transient compressible flow solvers. *International journal for numerical methods in fluids*, 56:2229–2244, 2008.

[20] R. Löhner, J. D. Baum, E. Mestreau, D. Sharov, C. Charman, and D. Pelessone. Adaptive embedded unstructured grid methods. *International Journal for Numerical Methods in Engineering*, 60(3):641–660, 2004.

[21] R. Löhner, R. J. Cebral, F. E. Camelli, S. Appanaboyina, J. D. Baum, E. L. Mestreau, and O. A. Soto. Adaptive embedded and immersed unstructured grid techniques. *Computer Methods in Applied Mechanics and Engineering*, 197:2173–2197, 2008.

[22] A. Hansbo, P. Hansbo, and M.G. Larson. A finite element method on composite grids based on Nitsche's method. *ESAIM: Mathematical Modelling and Numerical Analysis*, 37(3):495–514, 2003.

[23] R. Glowinski, T.W. Pan, T.I. Hesla, D.D. Joseph, and J. Periaux. A fictitious domain approach to the direct numerical simulation of incompressible viscous flow past moving rigid bodies: application to particulate flow. *Journal of Computational Physics*, 169(2):363–426, 2001.

[24] E. Burman and P. Hansbo. Fictitious domain finite element methods using cut elements: II. A stabilized Nitsche method. *Applied Numerical Mathematics*, 62(4):328–341, 2012.

[25] D.J. Benson and S. Okazawa. Contact in a multi-material Eulerian finite element formulation. *Computer Methods in Applied Mechanics and Engineering*, 193(39):4277–4298, 2004.

[26] M.A. Puso, E. Kokko, R. Settgast, J. Sanders, B. Simpkins, and B. Liu. An embedded mesh method using piecewise constant multipliers with stabilization: mathematical and numerical aspects. *International Journal for Numerical Methods in Engineering*, 104(7):697–720, 2015.

[27] X. Wang and W. K. Liu. Extended immersed boundary method using FEM and RKPM. *Computer Methods in Applied Mechanics and Engineering*, 193:1305–1321, 2004.

[28] F. Sotiropoulos and X. Yang. Immersed boundary methods for simulating fluid–structure interaction. *Progress in Aerospace Sciences*, 65:1–21, 2014.

[29] W. K. Liu, D.W. Kim, and S. Tang. Mathematical foundations of the immersed finite element method. *Computational Mechanics*, 39(3):211–222, 2007.

[30] L. T. Zhang, A. Gerstenberger, X. Wang, and W. K. Liu. Immersed finite element method. *Computer Methods in Applied Mechanics and Engineering*, 193:2051–2067, 2004.

[31] D. Sulsky, Z. Chen, and H.L. Schreyer. A particle method for history-dependent materials. *Computer Methods in Applied Mechanics and Engineering*, 118(1):179–196, 1994.

[32] A. Sadeghirad, R. M. Brannon, and J. Burghardt. A convected particle domain interpolation technique to extend applicability of the material point method for problems involving massive deformations. *International Journal for Numerical Methods in Engineering*, 86:1435–1456, 2011.

[33] J. Parvizian, A. Düster, and E. Rank. Finite cell method. *Computational Mechanics*, 41(1):121–133, 2007.

[34] H. Casquero, C. Bona-Casas, and H. Gomez. A nurbs-based immersed methodology for fluid–structure interaction. *Computer Methods in Applied Mechanics and Engineering*, 284:943–970, 2015.

[35] M.-C. Hsu, D. Kamensky, Y. Bazilevs, M. S. Sacks, and T. J. R. Hughes. Fluid–structure interaction analysis of bioprosthetic heart valves: significance of arterial wall deformation. *Computational Mechanics*, 54:1055–1071, 2014.

[36] D. Kamensky, M.-C. Hsu, D. Schillinger, J.A. Evans, A. Aggarwal, Y. Bazilevs, M.S. Sacks, and T.JR. Hughes. An immersogeometric variational framework for fluid–structure interaction: Application to bioprosthetic heart valves. *Computer Methods in Applied Mechanics and Engineering*, 284:1005–1053, 2015.

[37] T. J. R. Hughes, J. A. Cottrell, and Y. Bazilevs. Isogeometric analysis: CAD, finite elements, NURBS, exact geometry, and mesh refinement. *Computer Methods in Applied Mechanics and Engineering*, 194:4135–4195, 2005.

[38] J.A. Cottrell, T.J.R. Hughes, and Y. Bazilevs. *Isogeometric analysis: toward integration of CAD and FEA*. John Wiley & Sons, 2009.

[39] G.E. Farin. *NURBS: from projective geometry to practical use*. AK Peters, Ltd., 1999.

[40] L. Piegl and W. Tiller. *The NURBS book*. Springer Science & Business Media, 2012.

[41] D.F. Rogers. *An introduction to NURBS: with historical perspective*. Elsevier, 2000.

[42] J.S. Chen and T. Belytschko. Meshless and meshfree methods. In *Encyclopedia of Applied and Computational Mathematics*, pages 886–894. Springer, 2015.

[43] W.K. Liu, S. Jun, and Y.F. Zhang. Reproducing kernel particle methods. *International journal for numerical methods in fluids*, 20(8-9):1081–1106, 1995.

[44] W.K. Liu, S. Jun, S. Li, J. Adee, and T. Belytschko. Reproducing kernel particle methods for structural dynamics. *International Journal for Numerical Methods in Engineering*, 38(10):1655–1679, 1995.

[45] J.S. Chen, C. Pan, C.-T. Wu, and W.K. Liu. Reproducing kernel particle methods for large deformation analysis of non-linear structures. *Computer Methods in Applied Mechanics and Engineering*, 139(1):195–227, 1996.

[46] Y. Bazilevs, V. M. Calo, J. A. Cottrell, T. J. R. Hughes, A. Reali, and G. Scovazzi. Variational multiscale residual-based turbulence modeling for large eddy simulation of incompressible flows. *Computer Methods in Applied Mechanics and Engineering*, 197:173–201, 2007.

[47] J. A. Cottrell, A. Reali, Y. Bazilevs, and T. J. R. Hughes. Isogeometric analysis of structural vibrations. *Computer Methods in Applied Mechanics and Engineering*, 195(41):5257–5296, 2006.

[48] S. Lipton, J. A. Evans, Y. Bazilevs, T. Elguedj, and T. J. R. Hughes. Robustness of isogeometric structural discretizations under severe mesh distortion. *Computer Methods in Applied Mechanics and Engineering*, 199:357–373, 2010.

[49] S.G. Bardenhagen and E.M. Kober. The generalized interpolation material point method. *Computer Modeling in Engineering and Sciences*, 5(6):477–495, 2004.

[50] Yvonne D Murray. Users manual for ls-dyna concrete material model 159. Technical report, 2007.

[51] G. Hauke and T. J. R. Hughes. A unified approach to compressible and incompressible flows. *Computer Methods in Applied Mechanics and Engineering*, 113:389–396, 1994.

[52] T. Belytschko, W. K. Liu, and B. Moran. *Nonlinear Finite Elements for Continua and Structures*. Wiley, 2000.

[53] J. Lubliner. *Plasticity Theory*. Macmillan Publishing Company, 1990.

[54] J. C. Simo and T. J. R. Hughes. *Computational Inelasticity*. Springer-Verlag, New York, 1998.

[55] Fei Xu, George Moutsanidis, David Kamensky, Ming-Chen Hsu, Muthuvel Murugan, Anindya Ghoshal, and Yuri Bazilevs. Compressible flows on moving domains: stabilized methods, weakly enforced essential boundary conditions, sliding interfaces, and application to gas-turbine modeling. *Computers & Fluids*, 2017.

[56] J. Von Neumann and R.D. Richtmyer. A method for the numerical calculation of hydrodynamic shocks. *Journal of Applied Physics*, 21:232–237, 1950.

[57] W. F. Noh. Errors for calculations of strong shocks using an artificial viscosity and an artificial heat flux. *Journal of Computational Physics*, 72:78–120, 1987.

[58] T. J. R. Hughes. Generalization of selective integration procedure to anisotropic and nonlinear media. *International Journal for Numerical Methods in Engineering*, 15:1413–1418, 1980.

[59] T. Belytschko and L.P. Bindeman. Assumed strain stabilization of the 4-node quadrilateral with 1-point quadrature for nonlinear problems. *Computer Methods in Applied Mechanics and Engineering*, 88(3):311–340, 1991.

[60] Y.Y. Zhu and S. Cescotto. Unified and mixed formulation of the 4-node quadrilateral elements by assumed strain method: Application to thermomechanical problems. *International Journal for Numerical Methods in Engineering*, 38(4):685–716, 1995.

[61] T. Elguedj, Y. Bazilevs, V. M. Calo, and T. J. R. Hughes. B-bar and F-bar projection methods for nearly incompressible linear and nonlinear elasticity and plasticity using higher-order nurbs elements. *Computer Methods in Applied Mechanics and Engineering*, 197:2732–2762, 2008.

[62] A. Massing, M.G. Larson, A. Logg, and M.E. Rognes. A stabilized Nitsche fictitious domain method for the Stokes problem. *Journal of Scientific Computing*, 61(3):604–628, 2014.

[63] J. Chung and G. M. Hulbert. A time integration algorithm for structural dynamics with improved numerical dissipation: The generalized-α method. *Journal of Applied Mechanics*, 60:371–75, 1993.

[64] K. E. Jansen, C. H. Whiting, and G. M. Hulbert. A generalized-α method for integrating the filtered Navier–Stokes equations with a stabilized finite element method. *Computer Methods in Applied Mechanics and Engineering*, 190(3):305–319, 2000.

[65] Y. Bazilevs, V. M. Calo, T. J. R. Hughes, and Y. Zhang. Isogeometric fluid–structure interaction: theory, algorithms, and computations. *Computational Mechanics*, 43:3–37, 2008.

[66] F. Shakib, T.J.R. Hughes, and Z. Johan. A new finite element formulation for computational fluid dynamics: X. The compressible Euler and Navier-Stokes equations. *Computer Methods in Applied Mechanics and Engineering*, 89(1):141–219, 1991.

[67] E. Oñate and R. Owen. *Particle-based methods: fundamentals and applications*, volume 25. Springer Science & Business Media, 2011.

[68] S.R. Idelsohn, J. Marti, P. Becker, and E. Oñate. Analysis of multifluid flows with large time steps using the particle finite element method. *International Journal for Numerical Methods in Fluids*, 75(9):621–644, 2014.

[69] D.J. Benson. Computational methods in Lagrangian and Eulerian hydrocodes. *Computer Methods in Applied Mechanics and Engineering*, 99(2):235–394, 1992.

[70] D.J. Benson. *The Numerical Simulation of the Dynamic Compaction of Powders*, pages 233–255. Springer New York, New York, NY, 1997.

[71] Y. Bazilevs, L. Beirao da Veiga, J.A. Cottrell, T.J.R. Hughes, and G. Sangalli. Isogeometric analysis: approximation, stability and error estimates for h-refined meshes. *Mathematical Models and Methods in Applied Sciences*, 16(07):1031–1090, 2006.

[72] Y. Bazilevs, V.M. Calo, Y. Zhang, and T.J.R. Hughes. Isogeometric fluid–structure interaction analysis with applications to arterial blood flow. *Computational Mechanics*, 38(4-5):310–322, 2006.

[73] Y. Bazilevs, V.M. Calo, T.J.R. Hughes, and Y. Zhang. Isogeometric fluid-structure interaction: theory, algorithms, and computations. *Computational mechanics*, 43(1):3–37, 2008.

[74] D.J. Benson, Y. Bazilevs, M.-C. Hsu, and T.J.R. Hughes. Isogeometric shell analysis: the reissner–mindlin shell. *Computer Methods in Applied Mechanics and Engineering*, 199(5):276–289, 2010.

[75] G. Cox. The numerical evaluation of b-splines. *IMA Journal of Applied Mathematics*, 10(2):134–149, 1972.

[76] C. De Boor. On calculating with b-splines. *Journal of Approximation theory*, 6(1):50–62, 1972.

[77] L. Beirao da Veiga, D. Cho, and G. Sangalli. Anisotropic NURBS approximation in isogeometric analysis. *Computer Methods in Applied Mechanics and Engineering*, 209–212:1–11, 2012.

[78] T. J. R. Hughes, A. Reali, and G. Sangalli. Efficient quadrature for NURBS-based isogeometric analysis. *Computer Methods in Applied Mechanics and Engineering*, 199:301–313, 2010.

[79] F. Auricchio, F. Calabrò, T. J. R. Hughes, A. Reali, and G. Sangalli. A simple algorithm for obtaining nearly optimal quadrature rules for NURBS-based isogeometric analysis. *Computer Methods in Applied Mechanics and Engineering*, 249-252:15–27, 2012.

[80] J. Nitsche. Über ein Variationsprinzip zur Lösung von Dirichlet-Problemen bei Verwendung von Teilräumen, die keinen Randbedingungen unterworfen sind. *Abhandlungen aus dem Mathematischen Seminar der Universität Hamburg*, 36:9–15, 1971.

[81] J.S. Chen, W.K. Liu, M. Hillman, S.W. Chi, Y. Lian, and M.A. Bessa. Reproducing kernel approximation and discretization. In *Encyclopedia of Computational Mechanics, Second Edition [E. Stein, R. de Borst, and T.J.R. Hughes Eds.]*. Wiley, 2016. In press.

[82] W.K. Liu, S. Li, and T. Belytschko. Moving least-square reproducing kernel methods (I): Methodology and convergence. *Computer Methods in Applied Mechanics and Engineering*, 143(1-2):113–154, 1997.

[83] J.-S. Chen, C.-T. Wu, S. Yoon, and Y. You. A stabilized conforming nodal integration for Galerkin mesh-free methods. *International Journal for Numerical Methods in Engineering*, 50:435–466, 2001.

[84] J.S. Chen, M. Hillman, and M. Rüter. An arbitrary order variationally consistent integration for galerkin meshfree methods. *International Journal for Numerical Methods in Engineering*, 95(5):387–418, 2013.

[85] P.C. Guan, S.-W. Chi, J.S. Chen, T.R. Slawson, and M.J. Roth. Semi-lagrangian reproducing kernel particle method for fragment-impact problems. *International Journal of Impact Engineering*, 38(12):1033–1047, 2011.

[86] M. Hillman, J.S. Chen, and S.W. Chi. Stabilized and variationally consistent nodal integration for meshfree modeling of impact problems. *Computational Particle Mechanics*, 1:245–256, 2014.

[87] M. Hillman, J.S. Chen, and Y. Bazilevs. Variationally consistent domain integration for isogeometric analysis. *Computer Methods in Applied Mechanics and Engineering*, 284:521–540, 2015.

[88] M. Hillman and J.S. Chen. An accelerated, convergent, and stable nodal integration in galerkin meshfree methods for linear and nonlinear mechanics. *International Journal for Numerical Methods in Engineering*, 107:603–630, 2016.

[89] J.S. Chen, X. Zhang, and T. Belytschko. An implicit gradient model by a reproducing kernel strain regularization in strain localization problems. *Computer Methods in Applied Mechanics and Engineering*, 193(27-29):2827–2844, 2004.

[90] E. Burman. Ghost penalty. *Comptes Rendus Mathematique*, 348:1217–1220, 2010.

[91] W.G. Dettmer, C. Kadapa, and D. Peric. A stabilised immersed boundary method on hierarchical B-spline grids. *Computer Methods in Applied Mechanics and Engineering*, 311:415–437, 2016.

[92] G.A. Sod. A survey of several finite difference methods for systems of nonlinear hyperbolic conservation laws. *Journal of Computational Physics*, 27:1–31, 1978.

[93] L.I. Sedov. *Similarity and Dimensional Methods in Mechanics. Tenth Edition.* CRC Press, 1993.

[94] J. Giordano, G. Jourdan, Y. Burtschell, M. Medale, D.E. Zeitoun, and L. Houas. Shock wave impacts on deforming panel, an application of fluid-structure interaction. *Shock Waves*, 14(1-2):103–110, 2005.

[95] R. Deiterding and S. Wood. Parallel adaptive fluid–structure interaction simulation of explosions impacting on building structures. *Computers & Fluids*, 88:719–729, 2013.

[96] Leonard E Schwer and Yvonne D Murray. A three-invariant smooth cap model with mixed hardening. *International Journal for Numerical and Analytical Methods in Geomechanics*, 18(10):657–688, 1994.

[97] Youcai Wu, John E Crawford, and Joseph M Magallanes. Performance of ls-dyna concrete constitutive models. In *12th International LS-DYNA users conference*, pages 3–5, 2012.

[98] Guohua Zhou. *A Reproducing Kernel Particle Method Framework for Modeling Failure of Structures Subjected to Blast Loadings*. University of California, San Diego, 2016.

[99] SZ Zhang et al. Detonation and its applications. *Press of National Defense Industry, Beijing*, 1976.

[100] T Rabczuk and J Eibl. Modelling dynamic failure of concrete with meshfree methods. *International Journal of Impact Engineering*, 32(11):1878–1897, 2006.

[101] M. Ambati, T. Gerasimov, and L. De Lorenzis. A review on phase-field models of brittle fracture and a new fast hybrid formulation. *Computational Mechanics*, 55(2):383–405, 2015.

[102] R. H. J. Peerlings, R. De Borst, W. A. M. Brekelmens, and J. H. P. De Vree. Gradient enhanced damage for quasi-brittle materials. *International Journal for Numerical Methods in Engineering*, 39(19):3391–3403, 1996.

[103] R. de Borst and C. V. Verhoosel. Gradient damage vs phase-field approaches for fracture: Similarities and differences. *Computer Methods in Applied Mechanics and Engineering*, 312:78–94, 2016.

[104] C. Kuhn and R. Müller. A phase field model for fracture. *PAMM*, 8(1):10223–10224, 2008.

[105] R. Courant, K. Friedrichs, and H. Lewy. On the partial difference equations of mathematical physics. *IBM Journal of Research and Development*, 11(2):215–234, 1967.

[106] V. Ziaei-Rad and Y. Shen. Massive parallelization of the phase field formulation for crack propagation with time adaptivity. *Computer Methods in Applied Mechanics and Engineering*, 312(Supplement C):224–253, 2016. Phase Field Approaches to Fracture.

[107] J. Fineberg, S. P. Gross, M. Marder, and H. L. Swinney. Instability in dynamic fracture. *Phys. Rev. Lett.*, 67:457–460, Jul 1991.

[108] F. F. Abraham and H. Gao. How fast can cracks propagate? *Phys. Rev. Lett.*, 84:3113–3116, Apr 2000.

[109] M. J. Buehler, F. F. Abraham, and H. Gao. Hyperelasticity governs dynamic fracture at a critical length scale. *Nature*, 426(6963):141–146, Nov 2003.

[110] M. J. Borden, C. V. Verhoosel, M. A. Scott, T. J. R. Hughes, and C. M. Landis. A phase-field description of dynamic brittle fracture. *Computer Methods in Applied Mechanics and Engineering*, 217–220:77–95, 2012.

[111] A. A. Griffith. The phenomena of rupture and flow in solids. *Philosophical Transactions of the Royal Society of London A: Mathematical, Physical and Engineering Sciences*, 221(582-593):163–198, 1921.

[112] G. A. Francfort and J.-J. Marigo. Revisiting brittle fracture as an energy minimization problem. *Journal of the Mechanics and Physics of Solids*, 46(8):1319–1342, 1998.

[113] I. S. Aranson, V. A. Kalatsky, and V. M. Vinokur. Continuum field description of crack propagation. *Phys. Rev. Lett.*, 85(1):118–121, Jul 2000.

[114] A. Karma, D. A. Kessler, and H. Levine. Phase-field model of mode III dynamic fracture. *Phys. Rev. Lett.*, 87:045501, Jul 2001.

[115] R. Ortega and A. M. Robles-Pérez. A maximum principle for periodic solutions of the telegraph equation. *Journal of Mathematical Analysis and Applications*, 221(2):625–651, 1998.

[116] M. E. Gurtin. Generalized Ginzburg–Landau and Cahn–Hilliard equations based on a microforce balance. *Physica D: Nonlinear Phenomena*, 92(3):178–192, 1996.

[117] M. J. Borden, T. J. R. Hughes, C. M. Landis, A. Anvari, and I. J. Lee. A phase-field formulation for fracture in ductile materials: Finite deformation balance law derivation, plastic degradation, and stress triaxiality effects. *Computer Methods in Applied Mechanics and Engineering*, 312:130–166, 2016. Phase Field Approaches to Fracture.

[118] J. P. Cusumano, A. Roy, and Q. Li. Damage dynamics, rate laws, and failure statistics via Hamilton's principle. *Meccanica*, 50(1):77–98, 2015.

[119] M. Ortiz and A. Molinari. Effect of strain hardening and rate sensitivity on the dynamic growth of a void in a plastic material. *Journal of Applied Mechanics*, 59, 1992.

[120] M. J. Borden. *Isogeometric analysis of phase-field models for dynamic brittle and ductile fracture*. PhD thesis, Univerity of Texas, Austin, Austin, Texas, 2012.

[121] G. A. Holzapfel. *Nonlinear Solid Mechanics: A Continuum Approach for Engineering*. John Wiley & Sons, Chichester, 2000.

[122] G. Del Piero, G. Lancioni, and R. March. A variational model for fracture mechanics: Numerical experiments. *Journal of the Mechanics and Physics of Solids*, 55(12):2513–2537, 2007.

[123] M.F. Wheeler, T. Wick, and W. Wollner. An augmented-Lagrangian method for the phase-field approach for pressurized fractures. *Computer Methods in Applied Mechanics and Engineering*, 271:69–85, 2014.

[124] Y. Bazilevs, K. Kamran, G. Moutsanidis, D. J. Benson, and E. Oñate. A new formulation for air-blast fluid–structure interaction using an immersed approach. Part I: basic methodology and FEM-based simulations. *Computational Mechanics*, pages 1–18, 2017.

[125] G. M. Hulbert and J. Chung. Explicit time integration algorithms for structural dynamics with optimal numerical dissipation. *Computer Methods in Applied Mechanics and Engineering*, 137(2):175–188, 1996.

[126] T. J. R. Hughes. *The Finite Element Method: Linear Static and Dynamic Finite Element Analysis*. Dover Publications, Mineola, NY, 2000.

[127] L. Ambrosio and V. M. Tortorelli. Approximation of functionals depending on jumps by elliptic functionals via Γ-convergence. *Communications on Pure and Applied Mathematics*, 43(8):999–1036, 1990.

[128] Z. P. Bažant. Size effect on structural strength: a review. *Archive of Applied Mechanics*, 69(9):703–725, Nov 1999.

[129] E. Sharon and J. Fineberg. Microbranching instability and the dynamic fracture of brittle materials. *Phys. Rev., B Condens. Matter*, 54(10):7128–7139, Sep 1996.

[130] Y. Bazilevs, G. Moutsanidis, J. Bueno, K. Kamran, D. Kamensky, M. C. Hillman, H. Gomez, and J. S. Chen. A new formulation for air-blast fluid–structure interaction using an immersed approach: part II—coupling of IGA and meshfree discretizations. *Computational Mechanics*, pages 1–16, 2017.

[131] David Kamensky, Georgios Moutsanidis, and Yuri Bazilevs. Hyperbolic phase field modeling of brittle fracture: Part i-theory and simulations. *Journal of the Mechanics and Physics of Solids*, 2018.

[132] J. F. Kalthoff and S. Winkler. Failure mode transition of high rates of shear loading. In *Proceedings of the International Conference on Impact Loading and Dynamic Behavior of Materials (Edited by C. Y. Chiem, H.-D. Kunze and L. W. Meyer)*, Bremen, Germany, 1988.

[133] Christian Miehe, Martina Hofacker, and Fabian Welschinger. A phase field model for rate-independent crack propagation: Robust algorithmic implementation based on operator splits. *Computer Methods in Applied Mechanics and Engineering*, 199(45):2765 – 2778, 2010.

[134] Yuichi Nakamura. Model experiments on effectiveness of fracture plane control methods in blasting. *Fragblast*, 3(1):59–78, 1999.

[135] SH Cho, Y Nakamura, B Mohanty, HS Yang, and K Kaneko. Numerical study of fracture plane control in laboratory-scale blasting. *Engineering Fracture Mechanics*, 75(13):3966–3984, 2008.